Analysis of Acoustic Propagation in the Region of the New England Continental Shelfbreak

by

Brian John Sperry

B.S., Electrical and Computer Engineering, University of Iowa (1990)
S.M., Ocean Eng., M.I.T. / Woods Hole Oceanographic Institution (1994)
O.E., Ocean Eng., M.I.T. / Woods Hole Oceanographic Institution (1995)

Submitted in partial fulfillment of the
requirements for the degree of

DOCTOR OF PHILOSOPHY IN OCEANOGRAPHIC ENGINEERING

at the

MASSACHUSETTS INSTITUTE OF TECHNOLOGY

and the

WOODS HOLE OCEANOGRAPHIC INSTITUTION

June 1999

Signature of Author .....
.....
Joint Program in Applied Ocean Science and Engineering
Massachusetts Institute of Technology
Woods Hole Oceanographic Institution
April 20, 1999

Certified by.
.....
Dr. James Lynch
Woods Hole Oceanographic Institution
Thesis Supervisor

Certified by.....
.....
Dr. Glen Gawarkiewicz
Woods Hole Oceanographic Institution
Thesis Supervisor

Accepted by...
.....
Professor Michael Triantafyllou
Chairman, Joint Committee for Applied Ocean Science and Engineering
Massachusetts Institute of Technology/Woods Hole Oceanographic Institution

Analysis of Acoustic Propagation in the Region of the New England Continental Shelfbreak

by Brian John Sperry

Submitted to the Massachusetts Institute of Technology/
Woods Hole Oceanographic Institution
Joint Program in Applied Ocean Science and Engineering
on April 20, 1999, in partial fulfillment of the
Requirements for the degree of Doctor of Philosophy in
Oceanographic Engineering

Abstract

During July and August of 1996, a large acoustics/physical oceanography experiment was fielded in the Mid-Atlantic Bight, south of Nantucket Island, MA. Known as the Shelfbreak Front PRIMER Experiment, the study combined acoustic data from a moored array of sources and receivers with very high resolution physical oceanographic measurements. This thesis addresses two of the primary goals of the experiment, explaining the properties of acoustic propagation in the region, and tomographic inversion of the acoustic data. In addition, this thesis develops a new method for predicting acoustic coherence in such regions.

Receptions from two 400 Hz tomography sources, transmitting from the continental slope onto the shelf, are analyzed. This data, along with forward propagation modeling utilizing SeaSoar thermohaline measurements, reveal that both the shelfbreak front and tidally-generated soliton packets produce stronger coupling between the acoustic waveguide modes than expected. Arrival time wander and signal spread show variability attributable to the presence of a shelf water meander, changes in frontal configuration, and variability in the soliton field. The highly-coupled nature of the acoustic mode propagation prevents detailed tomographic inversion. Instead, methods based on only the wander of the mode arrivals are used to estimate path-averaged temperatures and internal tide "strength".

The modal phase structure function is introduced as a useful proxy for acoustic coherence, and is related via an integral transform to the environmental sound speed correlation function. Advantages of the method are its flexibility and division of the problem into independent contributions, such as from the water column and seabed.

Thesis Supervisor: Dr. James Lynch
Woods Hole Oceanographic Institution

Thesis Supervisor: Dr. Glen Gawarkiewicz
Woods Hole Oceanographic Institution

Acknowledgments

First and foremost I would like to thank my thesis advisors, Dr. Jim Lynch and Dr. Glen Gawarkiewicz, for the opportunity to conduct my thesis work as part of the PRIMER experiment. I want to especially thank Jim for all of the guidance, ideas and support he has graciously provided throughout the course of this dissertation. Working with Jim has been a truly enjoyable experience, and I look forward to opportunities for collaboration in the future. I want to also thank Glen for his support and enlightening discussions on the physical oceanography of the shelfbreak. I am very grateful to the members of my thesis committee, Art Baggeroer and Robert Beardsley, for their contributions and efforts, and also to Timothy Duda for chairing my defense. Many thanks to Arthur Newhall at WHOI for his computer assistance and for our enjoyable discussions on propagation codes and Linux. As a student in the Joint Program I have benefited from the unsung efforts of those in the WHOI Education Office, including Marci Simon, Stella Callagee, Julia Westwater and of course Ronni Schwartz at MIT. I know that my life as a graduate student at MIT would not have been nearly as enjoyable were it not for the administrative skills of Sabina Rataj, for which I am truly grateful.

Much of a graduate student's time is spent interacting with fellow students, and I would like to acknowledge a few in particular: Peter Daly, for keeping our computing power at MIT ahead of the pack; Kathleen Wage, for many a great conversation on acoustic coherence and its relevance to graduate student life; and Pierre Elisseeff, for our discussions on tomography and for taking a job in DC. A special thanks to everyone else (Joe Bondaryk, Yurij Dudko, Dan Kilfoyle, Vincent Lupien and Caterina Stamoulis, among others), who in one way or another contributed to a very satisfying graduate student experience.

None of this would have been possible without the support and confidence of my family and of my wife. I am grateful for all of the interest in and encouragement of my work from my parents John and Mercedes, brothers Todd and Craig, grandparents Frederick and Mary Sperry, and from my wife's parents, Steve and Donna Poort. The love and support of my wife, Kelly Poort, has seen me through all stages of this thesis, from dinner-table discussions of research to editing of the manuscript. It's been an amazing past few years, with both of us pursuing PhDs at MIT, and it's just going to get better. We make a wonderful team, Kel!

Finally, I would like to thank the Office of Naval Research for providing funding for this thesis through AASERT Grant N00014-96-1-0918, and through ONR Grant N00014-98-1-0059.

Contents

List of Tables

List of Figures

Chapter 1

Background

1.1 Introduction

The past decade has seen a growing interest in the acoustics of shallow water regimes. This shift in interest from blue to brown waters echoes in part the United States Navy's growing need for operation and surveillance capabilities in the littoral regions of the world. There is additional interest in the use of acoustics in shallow water areas for other reasons as well, including making oceanographic measurements for scientific purposes, such as studying ocean dynamics, or for monitoring tasks, such as tracking marine mammal populations or monitoring waste dispersal. Much of the focus of shallow water acoustics in the past has been on the interaction between acoustic signals and the ocean bottom. While such effects are clearly a critical factor in determining attributes like transmission loss, there are other equally important factors that warrant consideration. Coastal ocean dynamics within the water column can sometimes exert the strongest influence on acoustic travel times and energy distribution throughout the column. Ongoing research in this area has been revealing, both in terms of the oceanography itself as well its effects on acoustic transmissions. Both factors are key ingredients in predicting sonar performance in coastal waters.

Beginning with the Barents Sea Polar Front (BSPF) experiment in 1992, researchers at Woods Hole Oceanographic Institution (WHOI) and other institutions have combined simultaneous oceanographic and acoustic measurements in order to

study coastal ocean dynamics and their impact on acoustic propagation. The BSPF experiment gave a first look at how complex the acoustic propagation might be in a continental shelf environment (Lynch et al., 1996). One of the lessons of the experiment was that very high resolution sampling of the coastal oceanography was needed to fully capture the complicated arrival structures – kilometer resolution in the cross-front direction, with daily sampling. The 1995 SWARM (Shallow Water Acoustics in Random Media) shallow water internal wave scattering experiment looked in detail at the interactions between the acoustics and the energetic non-linear internal wave field (Apel et al., 1997). This experiment has been highly successful in looking at internal wave scattering, due to the use of rapidly-sampling thermistors and its position shoreward of the shelfbreak front.

Because of its complexity, the region of the continental shelfbreak has received significant attention, particularly from the acoustics community. There are numerous reasons, however, for wanting to study such areas, from both oceanographic and acoustic viewpoints. Shelfbreak fronts are often sources of cold water upwelling, which is significant from a fisheries' perspective. A front can also form a barrier to water flowing off the continental shelf, with potential implications for water waste disposal for seaboard cities. Acoustically, the effects of the shelfbreak regions represent an unknown influence on sound traveling from deeper water onto the shelf (and vice versa), an issue with obvious naval implications. Furthermore, it is conceivable that our understanding of the physical oceanography of the region may be enhanced through the use of acoustic transmissions.

In 1995, the Office of Naval Research (ONR) recognized the need for improved understanding of how acoustic signals are affected by complicated ocean fronts, such as the fronts found along the eastern United States continental shelfbreak. Funding was granted for a series of experiments, known as the Shelfbreak PRIMER[1] Experiments (SBPX), to take place in the Nantucket Shoals region of the Mid-Atlantic Bight. The primary objective was to investigate how the thermohaline variability near the shelfbreak front region affected acoustic signals propagating between the continental shelf

[1]Though not an acronym, PRIMER is by convention written in all capitals.

and continental slope (Lynch et al., 1997). The remainder of this chapter contains an overview of the PRIMER experiment, a short introduction to the region in which the experiment was conducted, and lastly, an outline for the rest of this thesis.

1.2 The Shelfbreak PRIMER Experiment

Two large Shelfbreak PRIMER experiments (SBPX) have been conducted, the first from July 22–August 8, 1996, and the second from February 9–27, 1997. Additionally, a preliminary cruise in the spring of 1996 provided a limited amount of oceanographic data during springtime conditions. The experiment goals of the SBPX were to study both the physical oceanography of the shelfbreak front and the characteristics of acoustic propagation through the region. Of interest were both the range of temporal variability, from scales of minutes to seasons, and the spatial variability, from scales of meters to tens of kilometers. Several institutions were involved in the effort; researchers from WHOI, the Naval Postgraduate School and the University of Rhode Island were responsible for various aspects of the data collection and analysis. This thesis is concerned only with the results and analysis of the summer experiment. The winter data have yet to be fully analyzed.

The PRIMER study area is illustrated in Figure 1-1. The upper panel shows the site relative to the Mid-Atlantic Bight. The area is about 150 kilometers south of Cape Cod and 200 kilometers east of the New Jersey coast. In this particular region of the eastern continental shelf, many isobaths actually run east-west. Figure 1-1(b) is a magnified view of the shaded region in Figure 1-1(a), showing the deployment locations. The instrument configuration was nearly identical for the summer and winter experiments. Sampling of the larger-scale oceanography was provided by Sea-Soar (indicated by the shaded region in Figure 1-1(b)), shipboard current profilers, Advanced Very High Resolution Radiometry (AVHRR) satellite data, and two days of airborne expendable bathythermographs (AXBTs). Continuous sampling of local meteorological conditions was provided by the ship, *R/V Endeavor*. For finer-scale oceanographic sampling, several thermistor chain moorings (labelled "O", "P" and

"Q" in the figure), were deployed on the western edge of the site, along with conventional current meters, SeaCats and an upward-looking acoustic Doppler current profiler (ADCP). Numerous individual thermistors (T-pods) were placed on many of the acoustic moorings as well.

One of the most important aspects of the Shelfbreak PRIMER experiments was the simultaneous sampling of the acoustic propagation and the oceanography. Four acoustic sources were deployed along the southern edge of the region, indicated by the stars in Figure 1-1(b). Two vertical line arrays (VLAs) of hydrophones were moored in the northern two corners of the domain, indicated by diamonds.

Other measurement sites relevant to the PRIMER experiment are indicated in Figure 1-1(b). These include a series of long-term moorings maintained by researchers at WHOI, several deep CTD stations that were occupied as part of PRIMER, two mooring sites from the 1979 Nantucket Shoals Flux Experiment (NSFE) that provided supplemental information on the local tides, as well as an Atlantic Margin CORing (AMCOR) drill site that provided geoacoustic data.

The particular experiment site was chosen in part for the absence of any major topographic features, such as large canyons, which could greatly complicate the oceanography and acoustics. A location was sought in which the seafloor was as uniform as possible in the along-shelf direction. One of the few drawbacks to the final site selection was the Navy's submarine lane into and out of New London, CT, which passed through the eastern side of the experiment domain. This traffic lane prevented the placement of moorings along the eastern edge, as was done on the western edge.

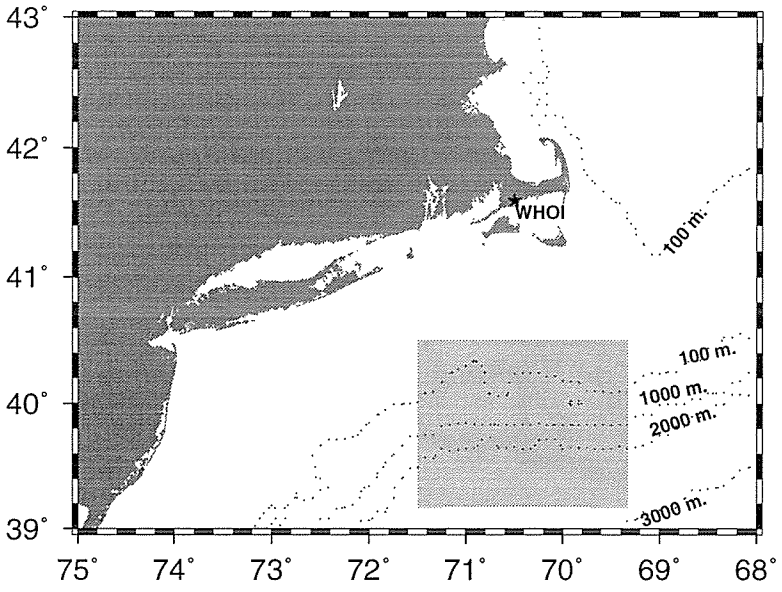

(a) Geographic overview.

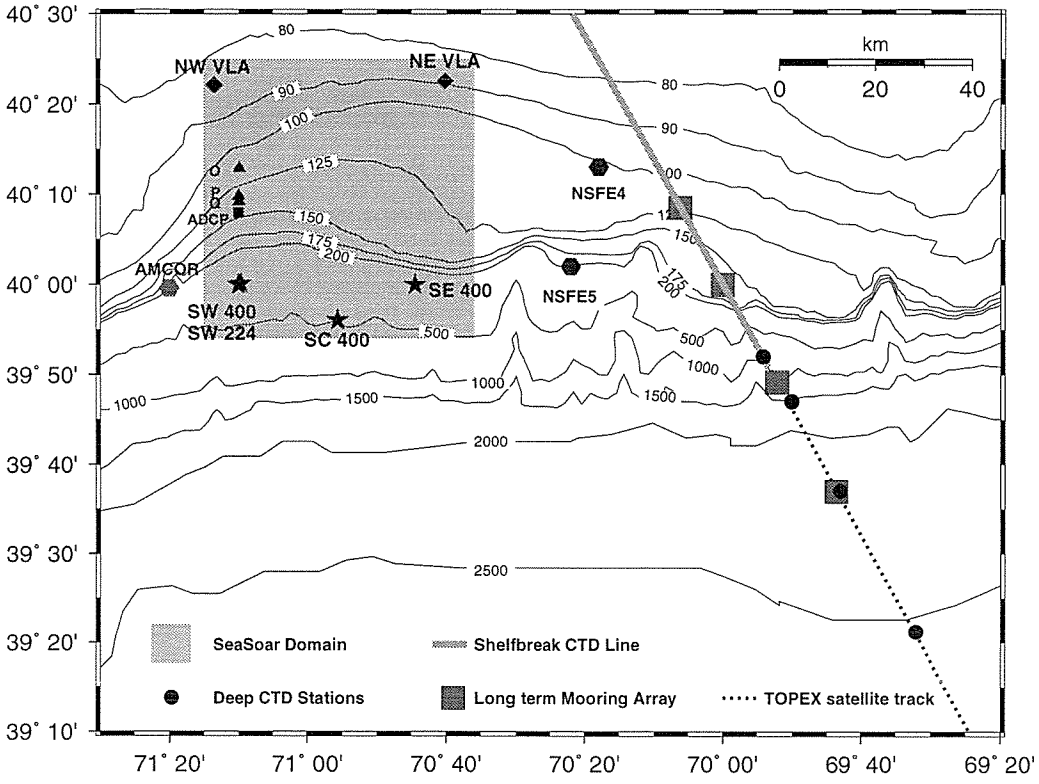

(b) Expanded view of shaded region indicated in (a).

Figure 1-1: The Shelfbreak PRIMER Field Study region, July–August, 1996.

1.3 The Mid-Atlantic Bight

The Mid-Atlantic Bight (MAB) is usually defined as the region extending from the eastern coastline of North America to the continental shelfbreak, encompassing a 2000 kilometer expanse from Cape Cod to the north down to the waters of Cape Hatteras in the south. The continental shelf tends to be quite wide, extending 50 to 150 km

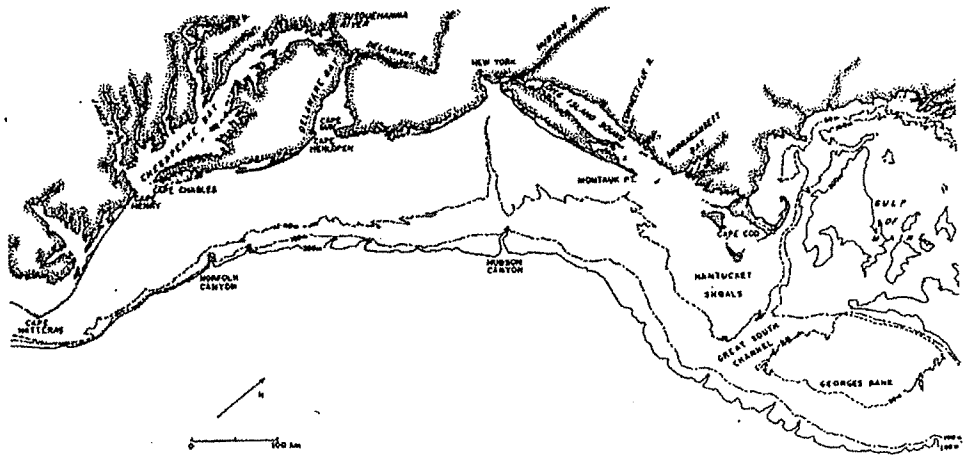

Figure 1-2: The Mid-Atlantic Bight, from Beardsley and Boicourt (1981).

away from the shoreline. The shelf floor generally slopes downward away from shore, with an average slope of around 0.07°. Along most of the MAB, there is a clearly-defined shelfbreak, dividing the shelf from the continental slope. At the break itself, depths range from 50–150 meters. Average inclinations on the slope range between 3° and 5°. The primary composition of the upper-bottom layer in the MAB is medium- to fine-grained sand, as well as silt layering in some places (Chamley, 1990).

It has been known since the early 1900's that an abrupt transition between cooler, fresher "coastal" waters and warmer, saltier "offshore" waters existed at the shelf-break (Beardsley and Boicourt, 1981). It has been shown that the shelf waters likely have their origin in the Greenland Sea area (Chapman and Beardsley, 1989), whereas the slope waters are fed by the Gulf Stream. The surface where these two water masses meet is referred to as the "shelfbreak front". On the large scale, it is a very stable feature that is present year around (Linder and Gawarkiewicz, 1998). Gawarkiewicz and Chapman (1992) describe the front formation at the edge of a continental shelf in

an initially linearly stratified fluid without horizontal density gradients. The model successfully reproduces many features seen in observations and also demonstrates the robustness of the frontogenesis process over a wide range of model parameters. On smaller scales, the front is highly variable, influenced by storms, winds and eddies. Associated with the front is a baroclinic jet driven by density differences between the shelf and slope waters. The jet is responsible for a large portion of the mass transport through the MAB. Results from the PRIMER oceanography work suggest that the region is significantly more complex than was anticipated (Gawarkiewicz, personal communication).

1.4 Thesis Outline

This thesis is an investigation of the characteristics of acoustic propagation through the New England shelfbreak front, a very complicated ocean environment. The second chapter of this thesis reviews the oceanographic observations made during the summer experiment, which are crucial to understanding acoustic propagation. Chapter 3 presents the acoustic data recorded at the northeast hydrophone array, and covers the important details involved in the data processing.[2] Chapter 4 presents the results of a detailed forward propagation study aimed at achieving a better understanding of how the detailed shelfbreak oceanography affects acoustic propagation. The acoustic simulations utilize much of the oceanography presented earlier in Chapter 2. The analysis of the recorded acoustic data in terms of modal propagation theory is detailed in Chapter 5. Also presented in that chapter are inversion results for mean water column temperature and internal tide "strength." Chapter 6 stands somewhat by itself, and is a theoretical investigation of acoustic coherence in shallow water and how it may be understood in part by means of the so-called "phase structure function". Finally, Chapter 7 summarizes the important findings and contributions of the thesis and outlines some of the important questions that remain for future studies.

[2]Readers interested in the acoustic data from the Northwest VLA are referred to the thesis by Miller (1998).

Chapter 2

Oceanographic Observations

2.1 Introduction

This chapter reviews the oceanographic conditions in the New England shelfbreak region that were encountered during the Summer 1996 Shelfbreak PRIMER Experiment (SBPX). For the most part, the oceanographic processes considered here are those having noteworthy impact on the acoustic propagation. Spatial scales range from the mesoscale eddy field and the front itself, down to the length-scale of a solitary internal wave ($\sim$100 m). The associated temporal variations are from days to minutes. Since the focus of this thesis is on the acoustics portion of the experiment, this chapter is primarily descriptive.

2.1.1 Instrumentation

The oceanographic instrumentation deployed during the summer SBPX included the SeaSoar vehicle, individual thermistors (T-pods) as well as thermistor chains, shipboard and moored ADCPs and some acoustic current meters (ACMs). This particular suite of instruments was chosen for its coverage of a wide range of space and time scales.

SeaSoar is essentially a towed CTD (conductivity-temperature-depth sensor) with wings that allow it to be "flown" up and down in the water column while being

towed at speeds of up to 8 knots. During the summer SBPX, the WHOI SeaSoar was deployed from the *R/V Endeavor* for a seven-day period, from July 26 through August 1, 1996. The maximum operating depth was 120 meters, and the vehicle was not typically flown closer than 10 meters from the bottom. A complete cycle down to 120 meters and back required roughly one kilometer to complete. The recorded data were averaged and placed onto a standard grid with a resolution of either 1 or 2 kilometers in the horizontal and 2 meters in the vertical. The SeaSoar operation plan called for four North-South transects per day, each approximately 40 km long and spaced 10 kilometers apart, as shown in Figure 2-1. During the summer experiment, operations were hindered by long-line and drift-net fishing activity. While the original experiment protocol called for continuous sampling day and night, a brief entanglement with fishing gear on Day Two (7/27/96) prompted the decision to operate well north of the 40.2° latitude during nighttime. Table 2.1 summarizes the sampling time periods for each transect over the seven-day period.

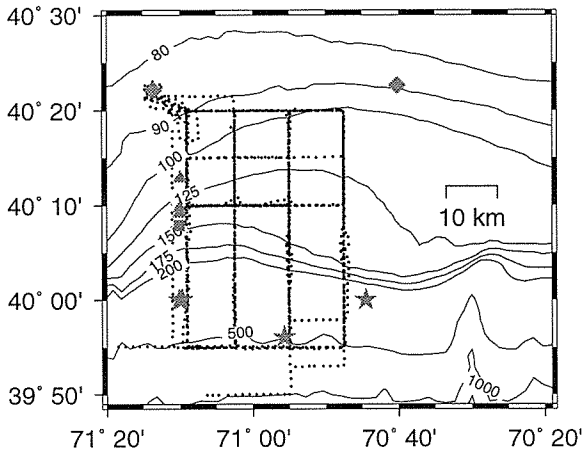

Figure 2-1: SeaSoar sampling grid for the seven-day deployment period during the summer SBPX. Symbols are used to indicate mooring locations.

In addition to the daily coverage provided by SeaSoar, vertical strings of rapid-sampling thermistors were deployed and individual thermistors (T-pods) were mounted on each acoustic mooring. Table 2.2 summarizes the locations and depths of each usable T-pod. All of the T-pods were sampled at either one or two minute intervals, which was sufficient to resolve the high-frequency soliton field (though just barely).

Day	Leg 1	Leg 2	Leg 3	Leg 4
Date, 24-hour time (UTC)				
26 July	0918–1236	1312–1630	1711–2039	2117–0029
27 July	1117–1441	1647–2017	2100–0012	0047–0206
28 July	1330–1648	1724–1918	2000–2142	2223–0118
29 July	0559–1229	1305–1636	1717–2042	2124–0030
30 July	1159–1523	1618–1812	1859–2053	2143–0041
31 July	0703–1142	1222–1544	1628–1955	2044–0008
1 Aug	—	—	0946–1304	1348–1659
Yearday (YD 1 = 1 Jan 00:00:00 UTC)				
YD 208	208.387–208.523	208.550–208.688	208.718–208.854	208.886–209.020
YD 209	209.470–209.609	209.701–209.846	209.875–210.006	210.033–210.087
YD 210	210.563–210.703	210.724–210.804	210.834–210.902	210.932–211.054
YD 211	211.252–211.521	211.547–211.692	211.723–211.861	211.894–212.021
YD 212	212.496–212.643	212.679–212.761	212.789–212.869	212.905–213.030
YD 213	213.294–213.488	213.515–213.656	213.687–213.830	213.864–214.006
YD 214	—	—	214.407–214.545	214.575–214.708

Table 2.1: Time-table of cross-shelf SeaSoar transects. Leg 1 is the western-most transect, Leg 4 is eastern-most. Legs 1 and 2 on 1 Aug. were canceled, and Leg 4 on 27 July was incomplete.

Mooring	T-pod Depths (meters)
NE VLA	1, 23, 37, 57, 77, 92
NW VLA	24, 30, 50, 70
SE 400 Hz Src	1, 10, 25, 40
SW 400 Hz Src	1, 40
SW 224 Hz Src	1, 224

Table 2.2: Depths of T-pods recovered from the various acoustic moorings. (SE 400 T-pods were actually on the nearby guard buoy.)

To provide a more rapid and spatially-larger snapshot of the hydrography than SeaSoar (at the expense of reduced resolution), there were two aircraft flights with AXBT drops on July 28 and August 8. Aside from a deep SeaSoar tow and a few deep CTD casts well off the shelf (as shown in Figure 1-1(b)), the AXBT data represent the deepest sampling of the shelfbreak region. This shortage of deep sampling will be encountered later in the acoustic modeling section, when sound speed profiles need to be constructed for the entire water column.

2.1.2 Seasonal Variations

Although the data considered in this thesis are taken solely from the summer PRIMER experiment, it is worthwhile to understand how the summertime conditions relate to the overall seasonal changes in the shelfbreak frontal structure. The primary attributes of interest are the thermohaline properties: temperature and salinity. A third component, the frontal current, or jet, is also important, but to a lesser degree from an acoustics standpoint. Seasonal variations are the dominant mode of variability within the MAB, and to first order they may be described by two primary "states": winter and summer. Figure 2-2 illustrates the variability between the two time periods for temperature, salinity and the along-shelf geostrophic current near the shelfbreak.

The position of the shelfbreak front is often defined by a particular temperature or salinity isopleth. The most common are the 10°C isotherm and the 34.5 PSU isohaline (Linder and Gawarkiewicz, 1998), which are indicated in Figure 2-2 by the thicker lines. During the winter season the combination of convective overturning and frequent storms creates a well-mixed body of cold water that extends over most of the shelf. During the summer, increased energy from insolation and the absence of major storms allows a highly stratified thermocline to develop in the upper 30 meters of the water column. In spite of the summertime warming, a mass of cold water remains near the bottom. This water is believed to be a remnant of the winter mixing, although it is conceivable that the deeper shelf water advects from the north in the summer or year-round. Unlike temperature, the salinity field does not transi-

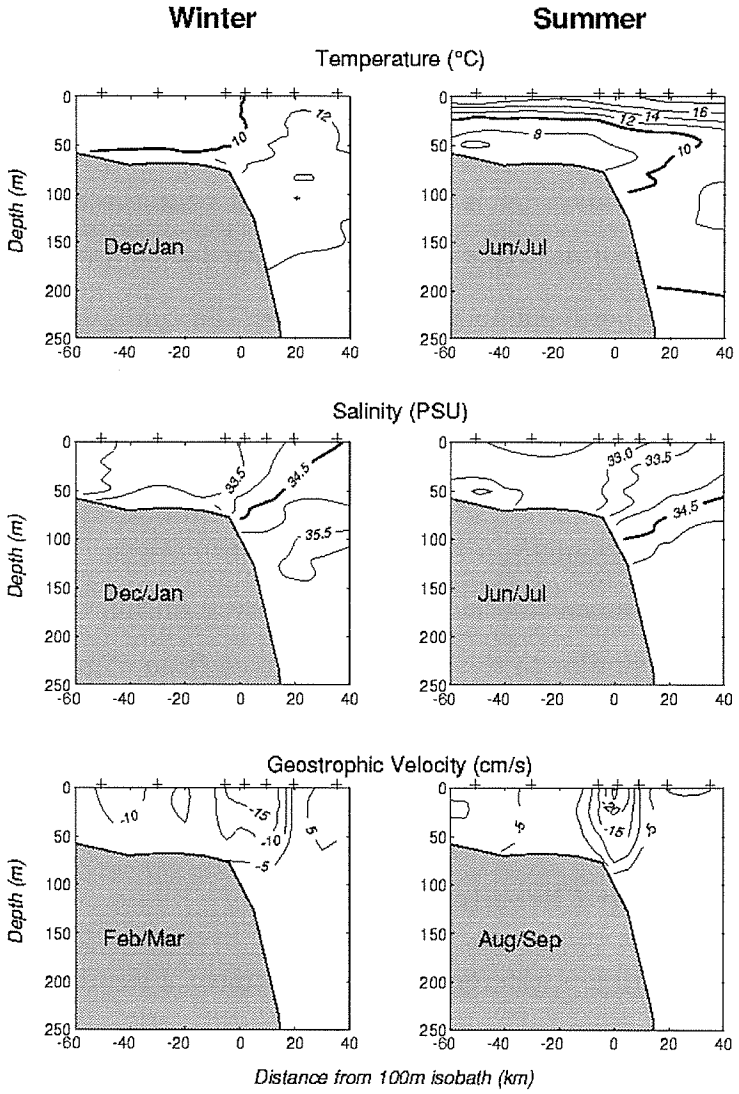

Figure 2-2: Comparison between winter and summer conditions near the shelfbreak, based on climatology. Thick lines (10°C and 34.5 PSU) indicate the location of the shelfbreak front. (Reprinted with permission from Pickart et al. (1999).)

tion from well-mixed to stratified. Instead, the primary change between summer and winter is the movement of the sloping isohalines on- and off-shore of the shelfbreak. During winter, the 34.5 PSU isohaline intersects the bottom around the 90-m isobath, whereas during the summertime it drops down to around 110 m, about 10 kilometers offshore of its winter position. Since salinity varies far less than temperature, the variations in density look very similar to those of the temperature field. The bottom two panels in Figure 2-2 illustrate the geostrophic currents set up by the cross-shelf density gradients. The main jet is usually situated near the 100-m isobath and is directed in the along-shelf direction (toward the west in the area south of Nantucket where the PRIMER experiment took place). Given the configuration of the acoustic network during the experiment, the current field associated with the jet did not significantly affect the acoustic transmissions.[1] However, secondary circulation effects due to the jet structure can locally modify the thermohaline fields, which in turn can produce noticeable changes in the acoustic transmissions. As the following sections demonstrate, the mean frontal structure observed during the summer PRIMER experiment was quite similar to the structure derived from climatology.

2.2 Mesoscale

2.2.1 Large-Scale Circulation

The large-scale circulation in the region of the continental shelfbreak is quite complicated because of the large number of factors influencing the local oceanography at any given moment. Eddies, frontal instabilities, meanders, and the Gulf Stream itself are some of the predominant influences. Since the advent of ocean-observing satellites, it has been known that over the course of a year as many as four or five warm-core rings spin off from the Gulf Stream toward the shelfbreak (Garfield and Evans, 1987). Many of these rings propagate westward and actually make contact with the shelfbreak front. Often, colder shelf water becomes entrained as spiraling filaments within

[1] An acoustic network designed for reciprocal transmissions, however, could easily measure the current field.

the eddies. Typical ring scales range from 100–300 kilometers in diameter and up to several hundred meters in depth. Lifetimes range from 6–12 months. Such eddies are important acoustically, not only because of the water properties of the eddies themselves, but also because of their interaction with the shelfbreak front. Depending on its position at the time, the Gulf Stream itself may also influence the behavior of the front. Even in the absence of the Gulf Stream and its associated warm rings, satellite AVHRR data have shown smaller eddies (10–50 km diameter), as well as waves, forming along the shelfbreak front itself as a result of instabilities (Ramp et al., 1983; Garvine et al., 1989). Figure 2-3 shows the sea surface temperature in the shelfbreak

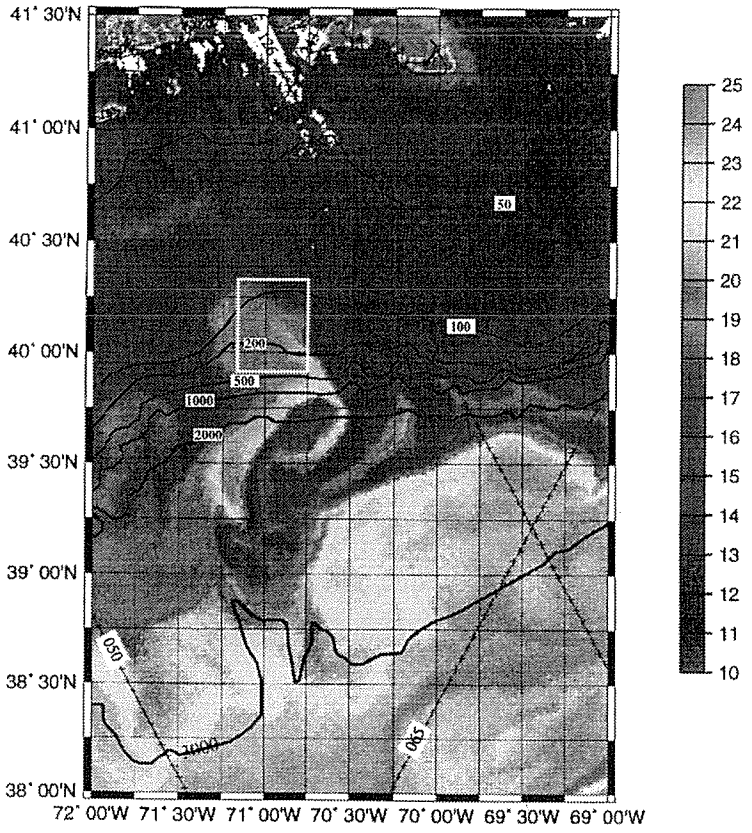

Figure 2-3: Sea surface temperature from AVHRR over shelf and slope on July 21, 1996. White box indicates the PRIMER study area. (Imagery provided by Mike Caruso of WHOI.)

region for the day of July 21, 1996, five days prior to the start of SeaSoar operations. The north wall of the Gulf Stream can be seen between the 2000- and 3000-meter

isobaths. The separation between shelf and slope water, generally near the 200-m isobath, is difficult to distinguish using only summer sea surface temperatures. Nevertheless, the satellite image is very important, as it shows two features which had significant impact on the experimental results. The first is the "T"-shaped filament of warm water seen within and just below the study region box. This filament may in fact represent a dipole-eddy pair that broke off from a nearby warm core ring. The warm, saline water associated with this filament was visible at times in the western portions of the SeaSoar data. The second feature is the southwestward meander of cool shelf water, just to the east of the slope filament. This shelf water meander was propagating to the west at 10 cm/s. This led to the apparent northward motion of the shelfbreak frontal zone at the eastern edge of the study area as the eastern edge of the meander propagated through the area. The presence of such complicated flow patterns over the continental slope leads to complex water mass distributions in the vicinity of the shelfbreak. For instance, the salinity and temperature gradients that are typically oriented in the cross-shelf direction may become gradients in the along-shelf direction instead. Given the proper configuration, an acoustic propagation path may go from having a perpendicular orientation relative to the front to being parallel to the front. Because so much of the thermohaline structure exists beneath the sea surface, it is difficult to fully appreciate the complicated nature of the shelfbreak front region, even from satellite pictures which only indicate 2-D structure. In the next section, SeaSoar data are presented to show this structure in more detail.

2.2.2 The Shelfbreak Front

SeaSoar was the primary instrument for measuring the thermohaline structure of the front during the experiment. The raw sections, with 2 m vertical resolution and 1 km horizontal resolution, and objective maps are used here to describe the thermal field. The data for each map were collected over a 24-hour time period.

Figure 2-4 shows how temperature and salinity vary with depth in the cross-shelf direction along the easternmost SeaSoar track. The data shown are from the raw SeaSoar records. The track for Day 7/27, being only a partial one, is not shown.

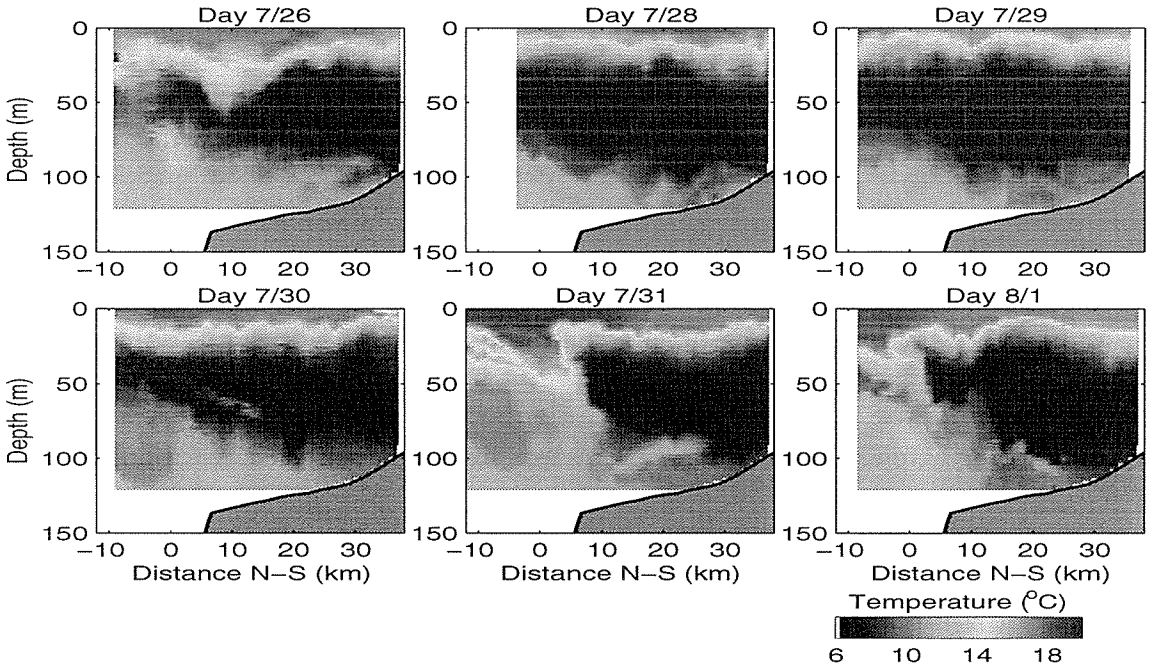

(a) Temperature

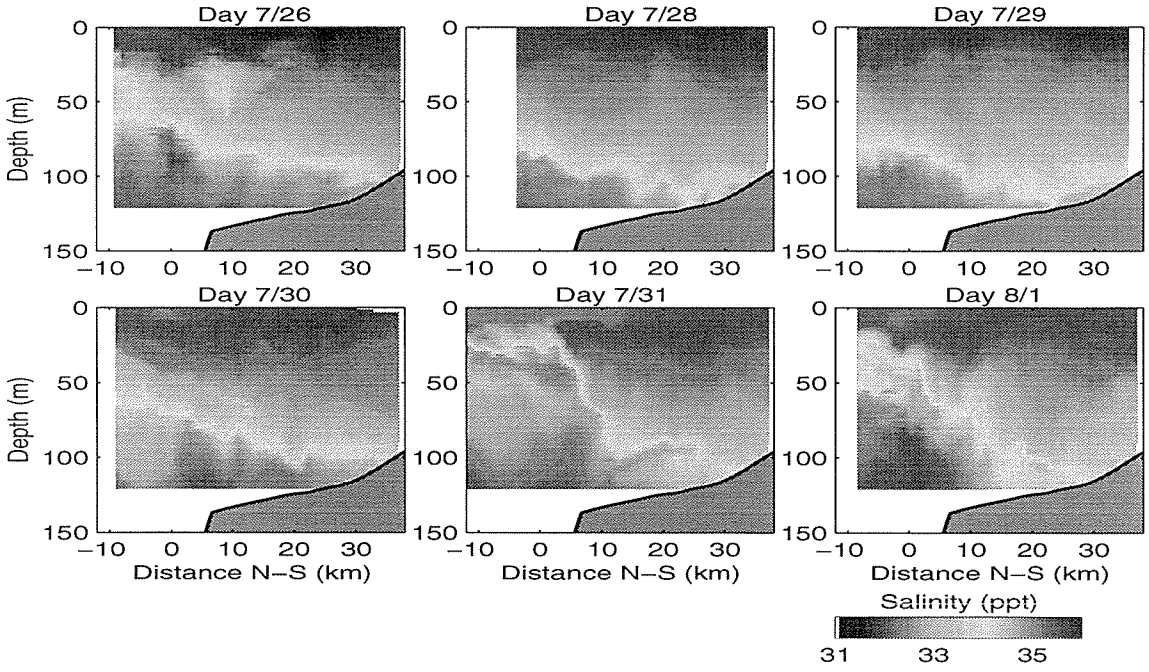

(b) Salinity

Figure 2-4: Raw SeaSoar sections along eastern-most track. Range is relative to location of SE 400 Hz source (40.000°N, 70.724°W).

This easternmost track is of particular interest as it runs parallel to the acoustic propagation path from the southeast source (located at range 0 km in the figure) to the northeast receiving array. On Day 7/31 in the temperature field a strong downwelling of the warmer surface waters is evident, possibly caused by secondary circulation effects that pull surface water down along the onshore edge of the front. Such a feature will later be shown to have a very significant acoustic impact. There is a marked decrease in the thermocline depth during Days 7/28 and 7/29, likely due to the presence of the shelf water meander, seen as a relatively homogeneous body of cold water extending from 25 to 90 meters in depth. Another feature evident in both the temperature and salinity figures is the foot of the shelfbreak front, which appears as a warmer, more saline, layer of water beneath the cold pool, extending as far onshore as the 100-m isobath. Like the downwelling mentioned earlier, the foot of the front plays an important role acoustically; the warm saline water creates an upward-refracting sound speed profile near the seafloor. The separation of shelf and slope waters is nicely demonstrated in the salinity figure, where slope waters have salinity values of 34.5 PSU or greater. The presence of the pool of cold, fresh water near the bottom is evident beneath the much warmer surface waters. From these SeaSoar records it appears that, at least along the eastern-most section, the front has been pushed well south of the study region, with the exception of Days 7/31 and 8/1, when it re-enters from the south after the eastern edge of the meander passes to the west.

Figures 2-5 through 2-7 are daily maps taken from the objectively-analyzed SeaSoar temperature data. (See LeTraoun, 1991, for details on the mapping method.) For reference, the locations of the PRIMER acoustic moorings are indicated. Note that the color scale is shifted between figures in order to maintain a reasonable dynamic range for presentation purposes. The shelfbreak front is definitely not a clean, stable feature with distinct boundaries. Instead, it varies from day to day, with significant structure on scales of 10 km or more. Evidence of the eddy filament, seen earlier in the AVHRR imagery, appears as pockets of warm water in the northwest corner of the temperature field at 4 m depth. Also evident is the colder shelf water

meander, which is most readily seen in the slice at 30 m depth. On Day 3 (July 28, 1996), the western edge of the meander has pushed the shelfbreak front well south of the southeast acoustic source mooring. The entire acoustic propagation path from SE to NE is now within the relatively homogeneous cold water of the meander. By Day 5 (July 30, 1996), the cold water is centered in the experiment domain, and by Day 7 (Aug. 1, 1996) it has mostly moved further to the west, although the eastern edge of the meander never reaches the western edge of the PRIMER region during the SeaSoar deployment period. The meander can be seen as deep as 90 m.

Maximum temperature variability within the frontal region occurs around 30 meters depth, where the temperature varies from 5–20°C. This is consistent with climatology observations (Linder and Gawarkiewicz, 1998). An important acoustic implication of the strong variability at 30 m is that the lower acoustic modes, which are the most sensitive to thermal variations in the sound speed at around 30–40 meters depth, will be most affected by variations in frontal structure. The presence of the frontal meander also appears to dominate other aspects of the local oceanography. For instance, soliton presence, as shown in a subsequent section, seems to be stronger on the western side, where there is more stratification. As the meander moves east to west, the stratified thermocline is squeezed into the upper 10-20 meters. This may have the effect of suppressing soliton/solibore generation and propagation. Acoustically, there is a much stronger tidal signature in the diagonal path from SW to NE than there is from SE to NE. One possible explanation is the greater temperature homogeneity with latitude of the water on the eastern edge, reducing the effects of tidal motion (advection of temperature structure) on the acoustic propagation. Temperature records from the SE mooring show a decrease in activity at the 40 m sensor, coinciding with the presence of the cold meander.

While the SeaSoar data reveal much variability in the upper part of the water column, they do not shed light on the structure below a depth of 120 m. For this reason it is necessary to look at the AXBT data. Figure 2-8 shows an example of AXBT profiles along a nearly north-south section going through the center of the experiment area. Below 150 meters there is a gradual decrease in temperature that

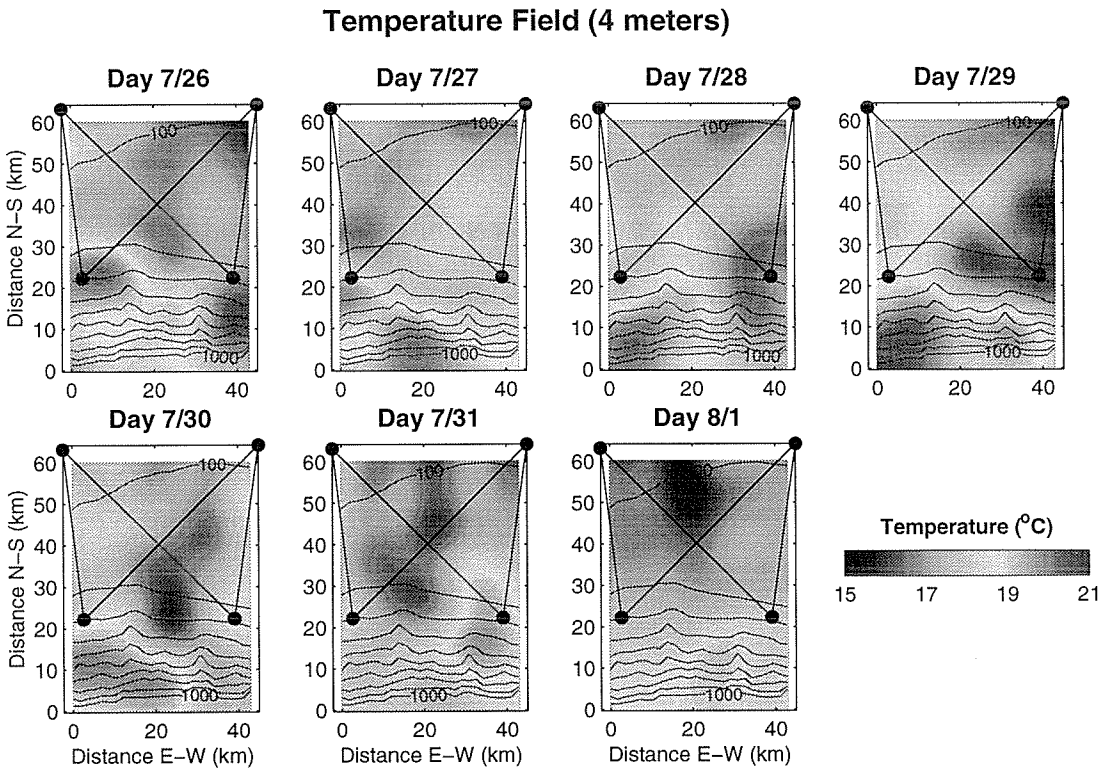

Figure 2-5: Temperature map at 4 meters depth from SeaSoar.

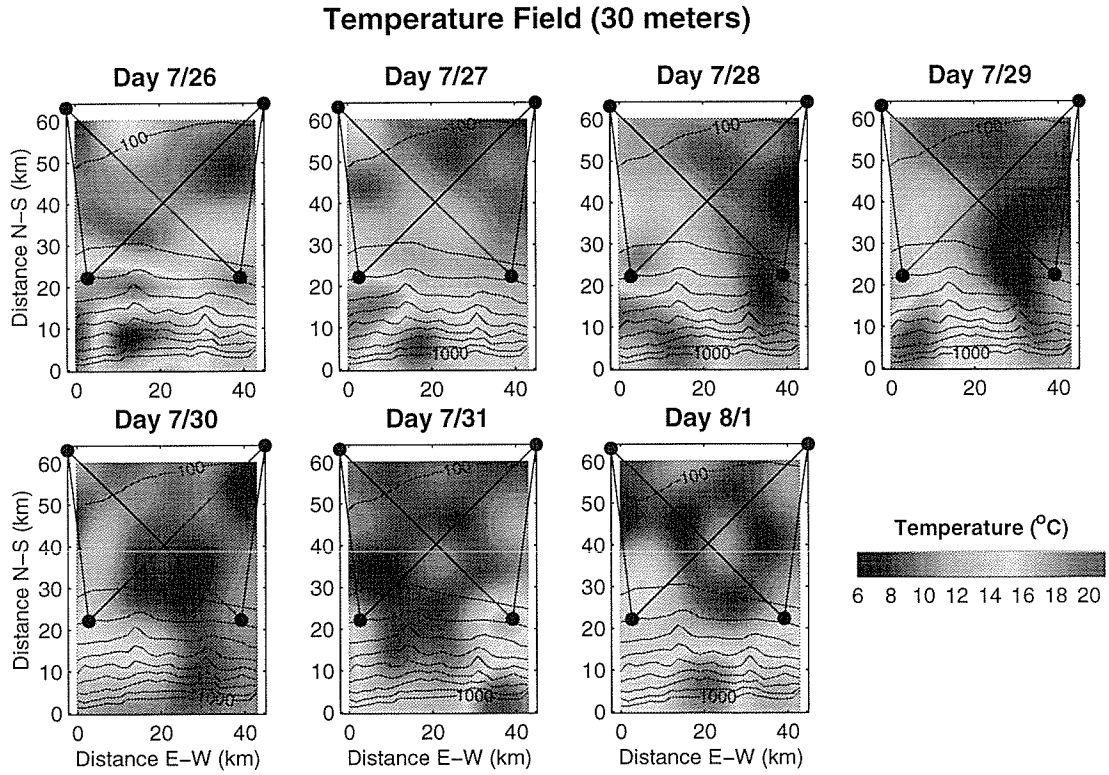

Figure 2-6: Temperature map at 30 meters depth from SeaSoar.

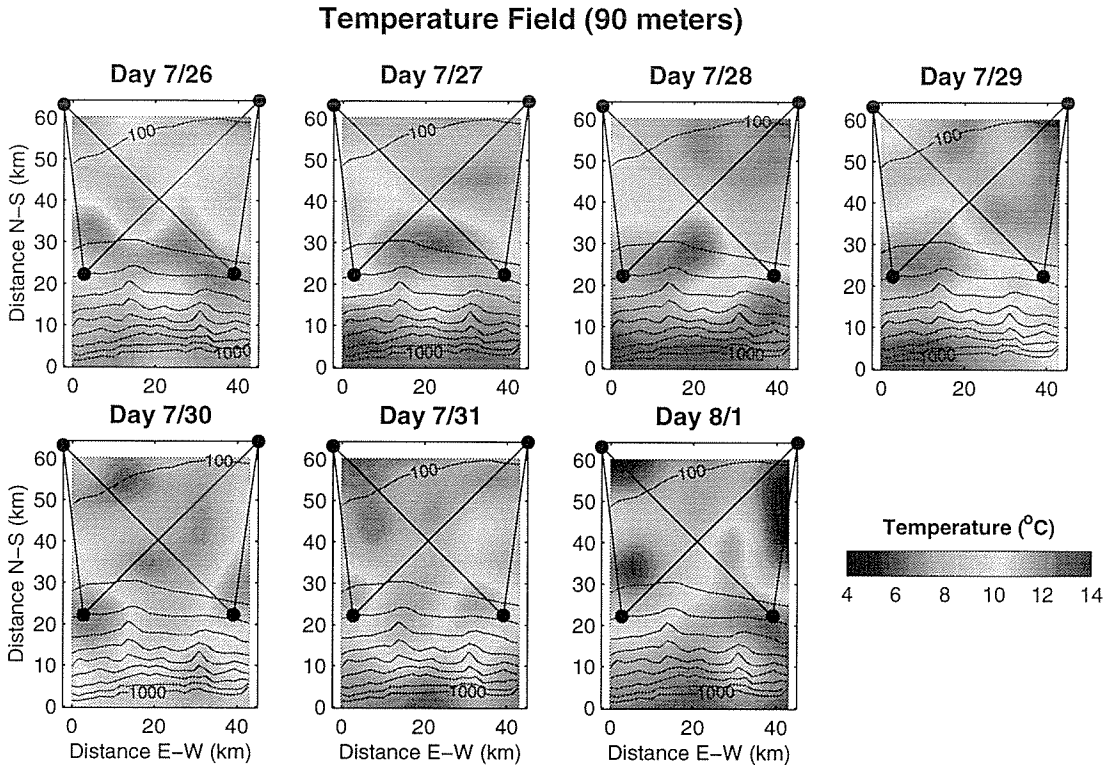

Figure 2-7: Temperature map at 90 meters depth from SeaSoar.

is similar between the two days. In agreement with SeaSoar, the upper water column shows considerable variability. The effect of the foot of the front is especially evident in the July 28 profile near 40.1° latitude, where the temperature abruptly increases with depth near the 100 meter mark.

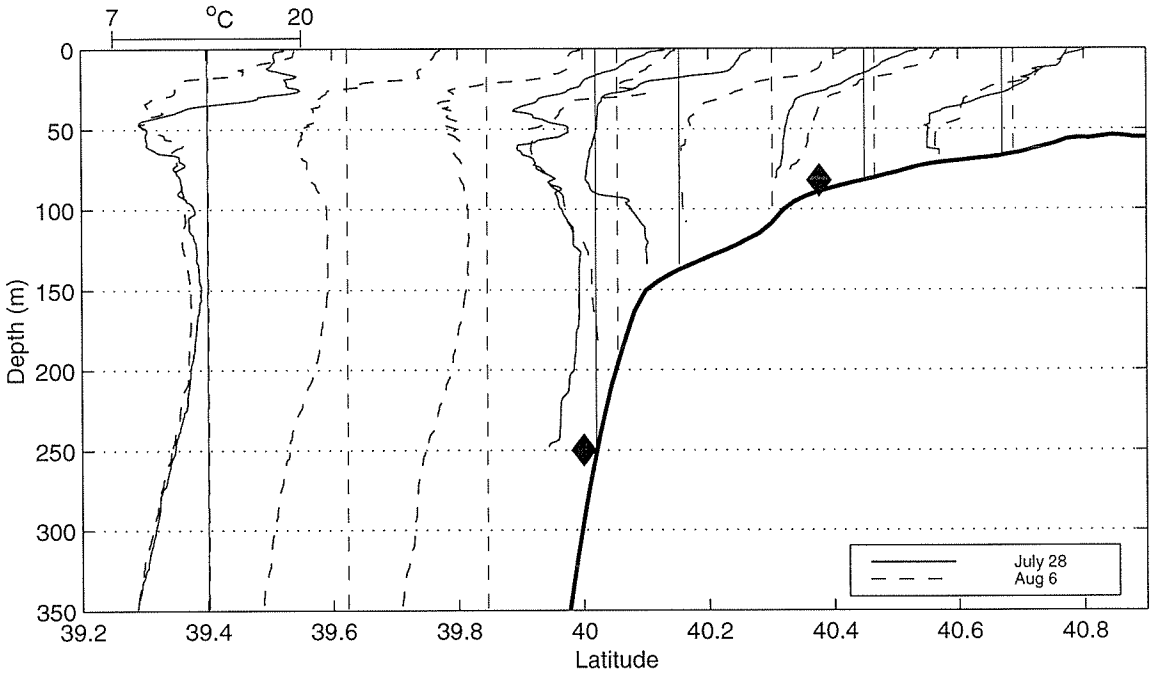

Figure 2-8: AXBT data along the $-70.9°$ longitude line. Vertical lines indicate the center for each profile, and correspond to the center of the temperature scale in upper left. Triangles indicate latitudes of the SE 400 Hz source and NE VLA.

2.3 Tidal Currents

Tidal currents on the continental shelf are of concern acoustically for both their direct and indirect effects on the acoustic propagation. Direct effects of tidal motion include changes in the effective acoustic propagation velocity via barotropic and baroclinic currents, changes in water depth due to the increasing and decreasing water volume in shallower depths, and also horizontal advection of water masses with differing acoustic properties. Perhaps more significant acoustically are the indirect effects. Tidal flow over steeply-sloping bathymetry, such as at the shelfbreak, is responsible for generating intense internal waves that propagate onshore. These waves will be given more consideration in a subsequent section.

Based on data recorded at moorings from two sites during the Nantucket Shoals Flux Experiment (NSFE) (Beardsley et al., 1985). the tide in the region is a mixed tide. Typical values for the form factor, or characteristic ratio, which measures the relative importance of diurnal and semidiurnal components, range from $F = 0.25$ to

0.5, where $F = (K_1 + O_1)/(M_2 + S_2)$, and K_1 is the lunisolar diurnal amplitude, O_1 the principal lunar diurnal, M_2 the principal lunar semidiurnal and S_2 the principal solar semidiurnal amplitude.

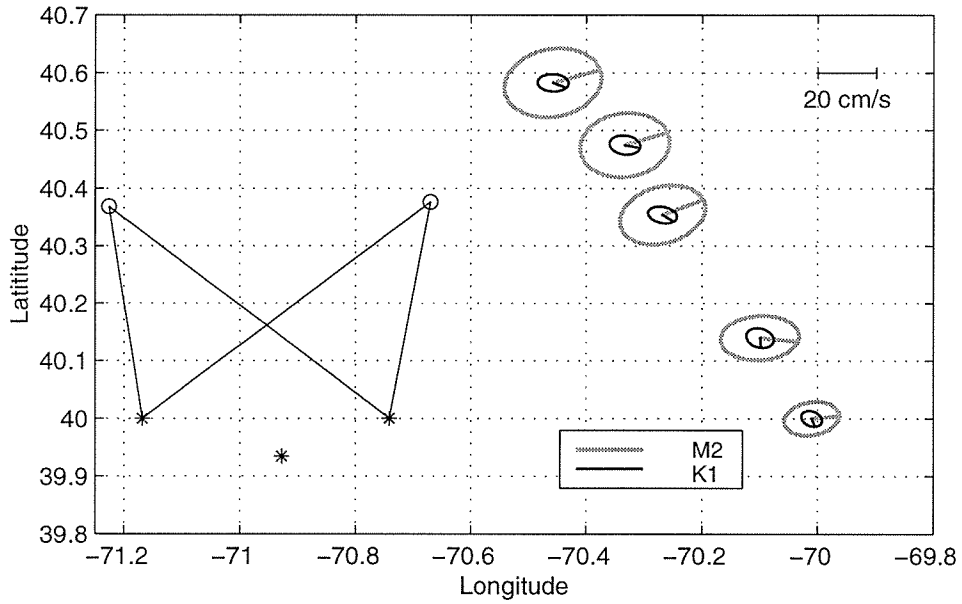

Figure 2-9: Tidal ellipses based on data from moorings along TOPEX/Poseidon subtrack. Tidal phases are indicated for June 27, 1996 00:00GMT. PRIMER acoustic moorings included for reference. (Data provided by Alberto Scotti of WHOI.)

Figure 2-9 shows the tidal ellipses for the two dominant constituents, M_2 and K_1, as computed from measurements made at several long-term moorings along the TOPEX/Poseidon subtrack adjacent to the PRIMER study region. There is a uniform increase in current amplitudes as one moves onto the shelf and into shallower water. The M_2 ellipses are nominally oriented east north-east and show little variability, while the K_1 ellipses rotate by almost 45 degrees from 40.0° to 40.6° latitude. During the Summer PRIMER experiment itself, the only current measurements available for estimating the local tides are from an ADCP on the western edge. The short time-series provided by the ADCP does not allow for accurate estimation of the tidal constituents however.

2.4 Solitons and Solibores

Internal waves (IWs) are a ubiquitous feature near the shelfbreak, just as they are over much of the continental shelf and deep ocean. While the spectrum of the deep ocean internal wave field is well described by the Garrett-Munk (GM) model (Garrett and Munk, 1972), an equivalent universal spectrum does not exist for shallow water. The GM model assumes an isotropic and homogeneous spectrum for linear internal waves, whereas in shallow water the internal wave field can be highly anisotropic, inhomogeneous, and may contain substantial energy in the form of non-linear IWs. Early analysis of the summer PRIMER data suggests that it is the non-linear internal wave field that dominates, although linear waves may certainly be present as well. From an acoustics standpoint, the non-linear solitary waves, with their larger amplitudes and shorter wavelengths, have the greatest effect on propagation, and so observations of the solitary wave field will be the focus this section. Other fine-scale oceanographic phenomena are likely present in the region; however, given the particulars of the PRIMER experiment (ranges, acoustic frequencies, etc.), they do not play nearly the role in influencing the acoustic propagation that the non-linear internal wave field does.

In its simplest form, an internal solitary wave, or soliton, travels as an isolated pulse of constant shape, representing a balance between nonlinear steepening effects and the tendency of differing frequency components in the wave to disperse. For weakly nonlinear internal waves, the expression governing the pulse shape may be written as (Apel et al., 1995)

$$\eta(x,t) = \eta_o \mathrm{sech}^2\left((x - Vt)/L\right) , \tag{2.1}$$

where $\eta(x,t)$ is the pulse shape as a function of position x and time t, V is the nonlinear velocity of the wave and L is its characteristic length. Figure 2-10 shows an example of this canonical soliton for an idealized two-layer ocean model. The bottom layer is both denser and thicker than the upper layer ($\rho_1 < \rho_2$ and $h_1 < h_2$). The exact expressions for V and L depend on a number of environmental parameters, the

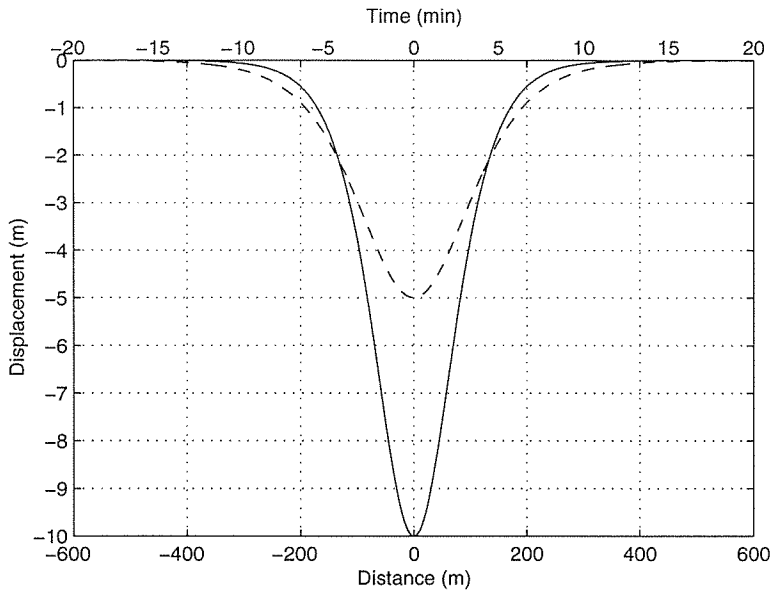

Figure 2-10: Example of a soliton wave for a simplified two-layer ocean, viewed as both functions of time and distance. Upper layer: h_1=25 m, ρ_1=1022.5 g/cm^3, lower layer: h_2=55 m, ρ_2=1026.0 g/cm^3

details of which will not be considered here. A good review of current soliton theory may be found in Apel et al. (1995). For the present discussion it suffices to point out that the propagation velocity, V, is always greater than the limiting velocity from linear internal wave theory, and that V varies with amplitude η_o. Larger solitons travel faster than smaller ones. The characteristic width, L, also depends nonlinearly upon amplitude. For situations such as in the above example, as well as throughout most of the continental shelf during summertime, $\rho_2 h_1^2 > \rho_1 h_2^2$, and solitons are waves of depression ($\eta < 0$), causing the pycnocline to decline as they pass through a region. The opposite probably happens during the wintertime, when h_1 is large and the pycnocline is only a short distance from the bottom.

There are currently two theories regarding soliton generation at the shelfbreak. In one instance, the barotropic tide incident upon the continental shelf is scattered into various baroclinic modes when a critical angle in the shelf slope is reached. The second mechanism is that of the lee-wave. (See Apel et al., 1995, for references for both mechanisms.) In this case, the ebb tidal flow off the shelf creates oscillations in the pycnocline, just offshore of the shelfbreak. As the tidal currents begin switch-

ing from ebb to flood, the series of pycnocline depressions, previously held in place against the steady offshore flow, are released and travel onshore as a train of solitons. A requirement for the generation of a lee-wave is that the offshore flow be supercritical with regard to the propagation velocity of the solitary internal waves. There is evidence, however, that during the summer PRIMER experiment such velocities were rarely supercritical, yet solitary waves were commonly observed (Colosi, personal communication).

In each mechanism, packets of solitons are generated at tidal periods, most often the semidiurnal period, as in the PRIMER area. Larger, faster solitons are typically at the front of a packet, a condition referred to as "rank ordering". In some instances a large step-like discontinuity in the pycnocline is generated at the shelfbreak and will propagate onshore, similar to a standard soliton. This combination of soliton/bore feature has been called a "solibore" (Henyey and Antje, 1997), although the naming convention is not universal. Because of variations in water depth and stratification, solibores tend to evolve into a train of solitons, beginning at the leading edge of the bore and working back toward the tail. By the time a solibore reaches the northern edge of the PRIMER region, all that typically remains is a rank-ordered packet of solitons with little hint of the initial bore. Because solibores were quite often observed during the summer PRIMER experiment, their acoustic impact will be considered in detail later in Chapter 4. Recent modeling by Colosi and Rehmann has been quite successful in reproducing the propagation characteristics of solibores (Colosi, personal communication).

Figure 2-11 shows a synthetic aperture radar (SAR) image taken a week or so prior to the summer PRIMER experiment. The image illustrates the spatial variability of a typical solitary wave pattern, which can provide clues as to the location of soliton generation sites. In this instance, in addition to the soliton trains propagating more or less perpendicular to the isobaths, there are also solitons radiating from something acting as a point source (perhaps a submarine canyon) somewhere along the western edge of the figure. A typical propagation velocity of a soliton in the region is around 0.7 cm/s. This implies a north-to-south transit time across the PRIMER area of

around 16–17 hours. For at least some of the time, then, there will be two sets of M_2-linked soliton packets generated at the shelfbreak between the acoustic sources and receivers.

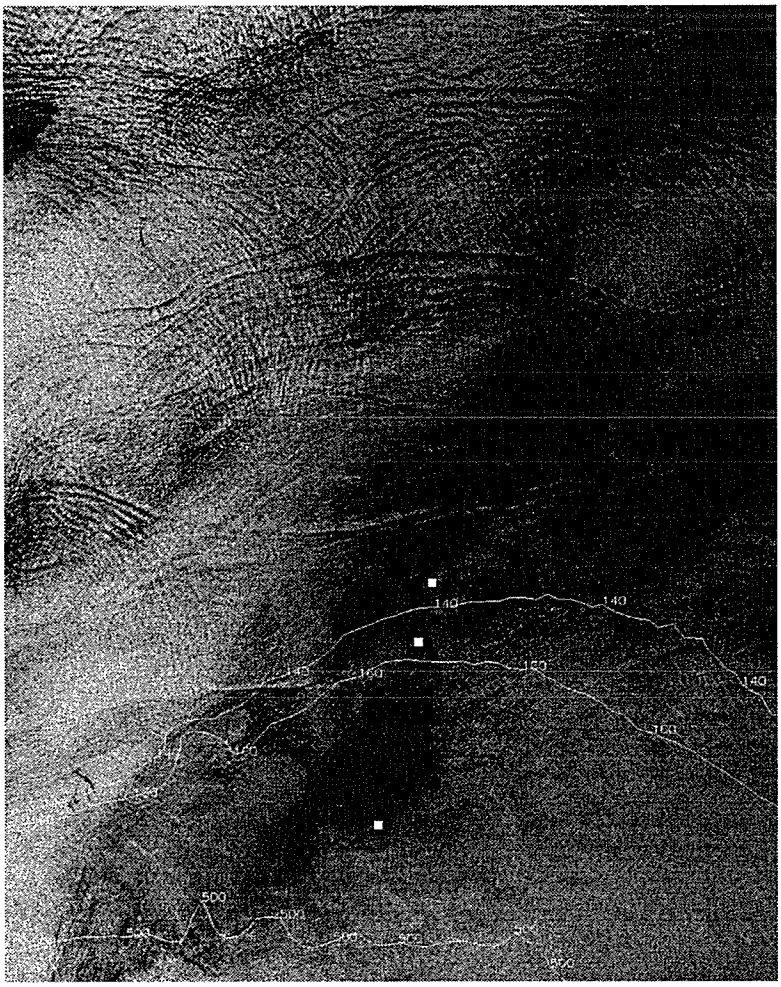

Figure 2-11: SAR image from several weeks before the July experiment, showing soliton packets propagating over the PRIMER experiment site. From top to bottom, white squares indicate locations of thermistor chain "O", ADCP and the SW 400 Hz acoustic source, respectively. (Refer to Figure 1-1(b) for detailed mooring map.) (SAR image courtesy of David Thompson of APL:JHU. Not for use or reproduction without permission.)

Observations of the soliton field were made around the study area perimeter by a variety of thermistors and an ADCP. While the western side was well-sampled, the eastern side of the region was monitored only by T-pods on the southeast and northeast acoustic moorings. The SE T-pod data showed little vertical structure that

could be consistent with traveling solitons or solibores. This could be an indication that the non-linear internal waves were not developed at that location, implying that the generation site was actually inshore of the SE mooring. Because the acoustic data considered in this thesis were all collected from the NE VLA, the T-pods from that mooring will be of primary interest here. Figure 2-12 shows the temperature as a function of depth and time, as recorded by T-pods on the NE VLA. The numerous spikes propagating along the thermocline are likely to be solitons. The vertical white lines are spaced at 24-hour intervals. With reasonable frequency, there appear to be two packets arriving within each 24-hour period, indicative of a high correlation with the M_2 tide.

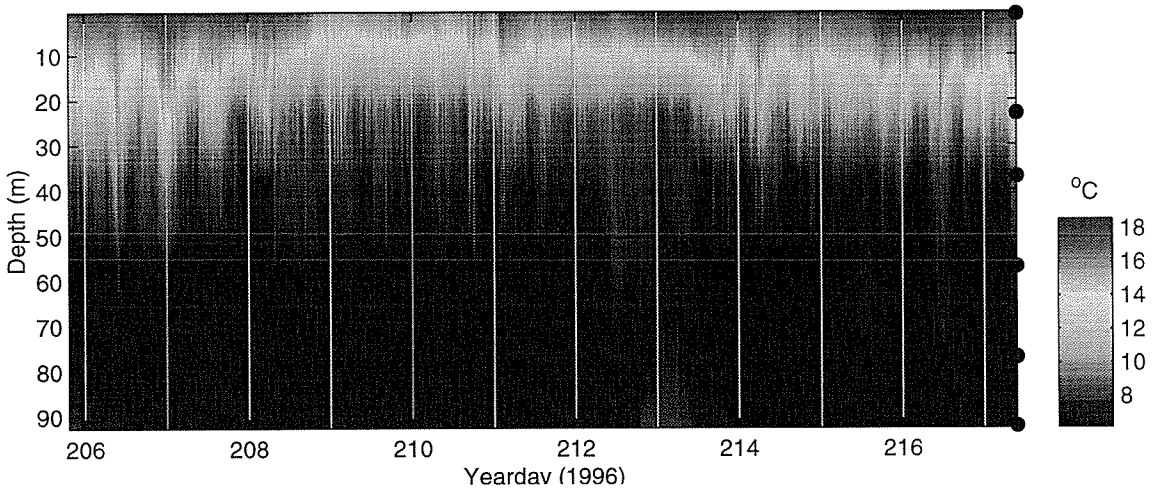

Figure 2-12: Thermistor data from the NE Vertical Line Array (VLA). Thermistor locations are indicated on the right side of figure by filled circles.

It is often desirable to know the displacement, $\eta(x,t)$, associated with the solitons which are seen in the thermistor data. Since the displacements are, in reality, displacements of isopycnal surfaces under the influence of gravity, density is the required parameter. However, the thermistors provide only temperature, and the SeaSoar provides only infrequent (and not co-located) salinity data. One possibility is to use the relationship $\eta = \Delta T/(\partial T/\partial z)$, a calculation that has been shown to be in reasonable agreement with the result using actual isopycnal surfaces (Racine, 1996). The procedure actually followed was to use interpolation and contouring methods to compute the isotherm displacements. Figure 2-13 shows the resulting power spectral density

from the isotherm displacement estimate. There is a definite peak in the displacement spectrum around the M_2 frequency. Figure 2-14 shows the 12°C-isotherm as

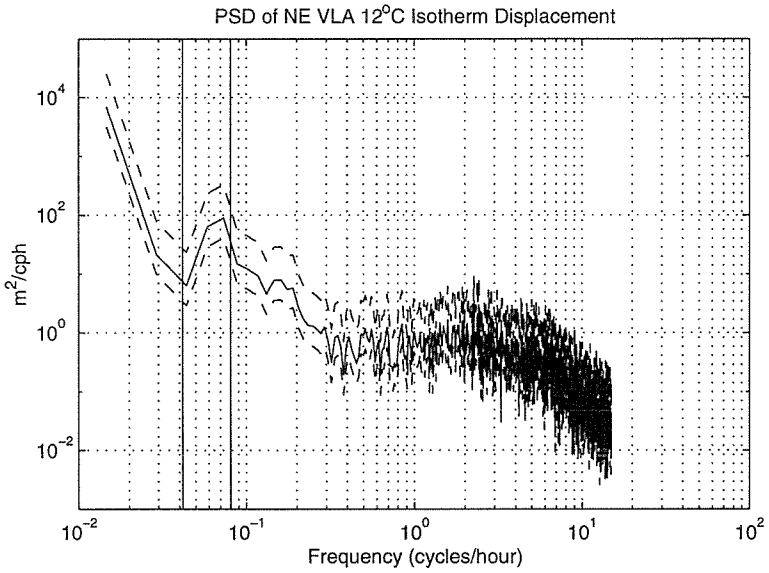

Figure 2-13: Power spectral density of 12-°C isotherm extracted from the NE VLA, shown with 95% confidence interval (dashed lines). Vertical lines indicate diurnal and semidiurnal periods.

extracted from the NE VLA thermistor data. The time series has been broken into consecutive 2×12.42-hour segments which are aligned in the plot. Vertical lines are drawn to aid in identifying soliton packet arrivals that may be linked to the semidiurnal tide. Since the tide is mixed, however, the semidiurnal dependence may not be exact. Several rank-ordered soliton packet arrivals are apparent, some of which differ substantially from the semidiurnal lines. The presence of an underlying solibore depression is apparent in a few of the cases. Given the scattering of some of the arrivals in time, it is likely that solitons are arriving from multiple generation sites, and that the sites do not consistently generate solibore/soliton packets. In fact, the periods during which the SeaSoar data show the cold water meander situated over the eastern edge of the region (YD 211-213) correspond to periods of reduced soliton activity. In a careful study of packet arrivals at moorings on the western side, it was noted that the arrivals had an RMS wander about the 12.42 hour period of around 2.4 hours (Lynch, personal communication). The packets seen at the NE VLA and

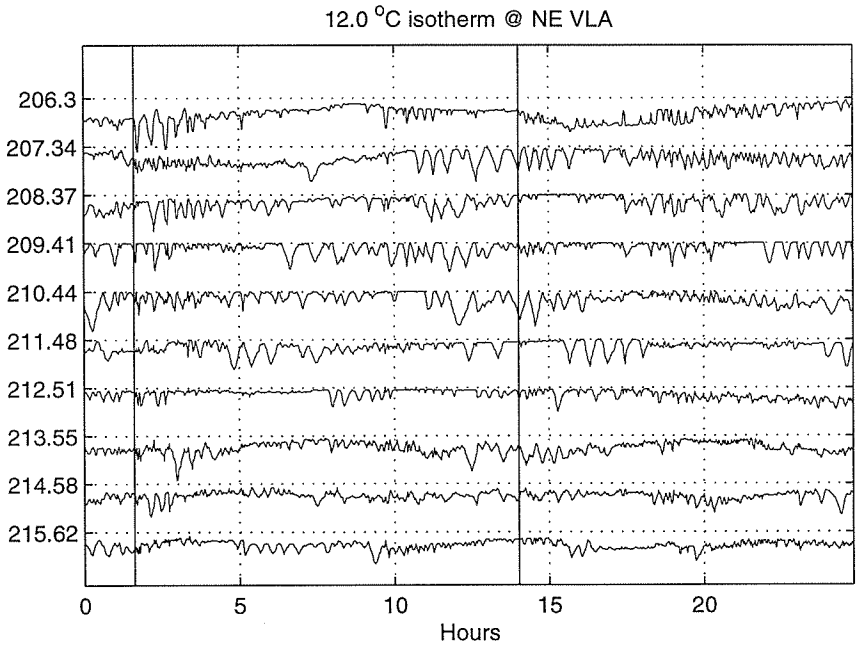

Figure 2-14: Vertical displacement of the 12 °C isotherm. Vertical lines represent alignment with a 12.42 hour semidiurnal cycle. Offset between isotherm segments is 40 meters. Numbers along the y-axis represent starting times for each isotherm in yeardays.

identified as being most-likely M_2-related show a similar wander in arrival times.

2.5 Summary

This chapter has provided an overview of some of the significant oceanographic observations made during the summer PRIMER experiment. The general structure of the shelfbreak front is similar to that shown in the climatology but there is also a large amount of structure on the 1–10 km scale that is not captured by the climatology. In particular, the shelf water meander and the presence of an eddy filament create conditions that differ from the canonical, isobath-aligned shelfbreak front. This can have considerable impact on acoustic propagation through the region, depending on the locations of source and receiver relative to the front.

While little is known about the temporal or spatial distribution of shelf water meanders, it is known that pockets of shelf water are more frequently ejected from the shelfbreak front into the adjacent slope water during late spring and early summer. The SeaSoar data collected during the PRIMER experiment represent the only data reported to date that accurately captures such motion of a meander.

The thermistor records from the NE VLA show an energetic soliton field with frequent packets that appear to be linked with the M_2 tide. Solitons are likely arriving from multiple generation sites. There appears to be a correlation between the presence of the shelf water meander and a decrease in the soliton activity as measured at the NE VLA. The acoustic impact of the oceanography presented in this chapter will be discussed in Chapter 4.

Chapter 3

Data Acquisition and Processing

The acoustic element of the Shelfbreak PRIMER Experiment (SBPX) was designed both to explore the effects of the shelfbreak front region on the propagation of acoustic signals and to provide estimates of the temperature field, via acoustic tomography, that would supplement the more traditional oceanographic measurements discussed in the previous chapter. To those ends, a network of acoustic transmitters and receivers was deployed. The configuration of this network, its signals, and the processing of the collected data are discussed in this chapter. A second component of the acoustics experiment, a one-day series of SUS (Sound, Underwater Signal) charges deployed within and around the tomography network, was used in inversions for geoacoustic properties of the bottom. The interested reader is referred to the work by Potty and Miller (1998).

3.1 The SBPX Acoustic Network

The acoustic network, as illustrated in Figure 3-1, was designed to bracket the nominal position of the shelfbreak front, with transmitters to the south of the shelfbreak and receivers to the north. Care was taken to place the network in an area where the seafloor was relatively uniform in the along-shelf direction. There were four acoustic transmitters, three 400 Hz and one 224 Hz Webb organ pipe tomography sources moored along the southern edge of the region. Acoustic source levels were 183 dB re

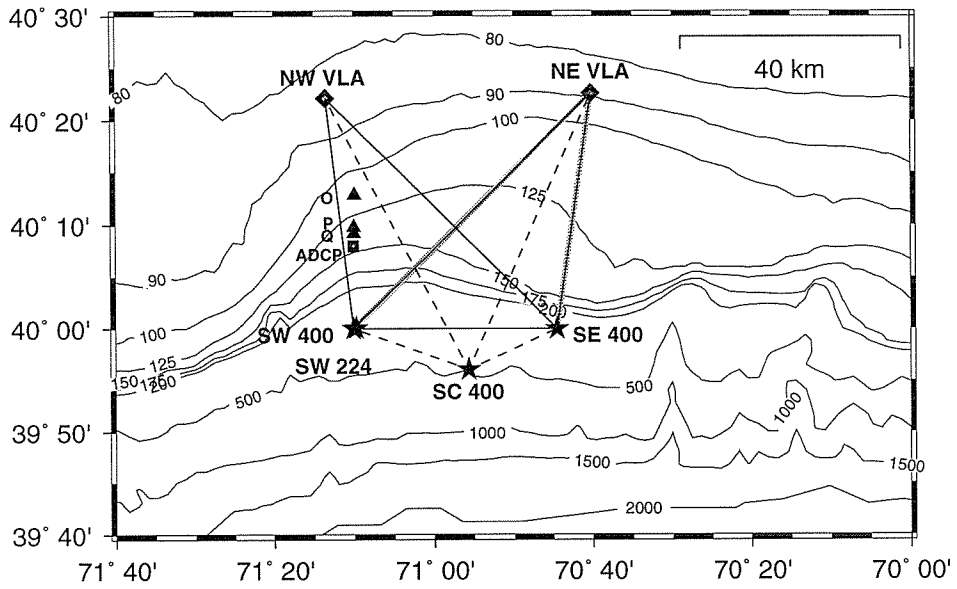

Figure 3-1: Shelfbreak PRIMER Experiment acoustic network configuration. Stars represent acoustic sources and circles indicate vertical line arrays. Figure is an expanded view of shaded region in Fig. 1-1(b).

1 μPa @ 1 m. Two vertical hydrophone arrays were deployed in the northeast and northwest corners, as shown in Figure 3-1. Table 3.1 details the deployment coordinates for each mooring. The 224 Hz and one of the 400 Hz sources were co-located in the western corner, providing an opportunity for multi-frequency propagation studies, though such comparisons are not part of this thesis. The east-west paths along the southern edge utilized very short, eight-element vertical receiving arrays attached just above each of the three 400 Hz sources. The data considered in this thesis are limited to the receptions recorded on the northeast vertical array (NE VLA).[1] During the summer experiment the central 400 Hz source failed shortly after deployment, reducing the resolution of the tomography network.

The two VLAs deployed as part of the Summer SBPX were both 16-element arrays with nominal sensor spacing of 2.5 meters. Figure 3-2 illustrates the configuration of the NE VLA. The "U"-shaped mooring design insured that the guard buoy remained

[1] As a point of clarification, this particular array was given two different "nicknames" that have appeared from time to time. It sometimes is known as the "shark", in reference to the toothy *Charcharadon* motif of its electronics sled, or, alternatively, since its surface buoy lacked the telemetry capabilities of the western VLA, it is known as the "dope-on-a-rope".

Source	Latitude	Longitude	Src Depth	Range to NE VLA
SW-224	39° 59.995′	−71° 9.699′	291.0 m	59.084 km
SW-400	39° 59.995′	−71° 10.100′	285.0 m	59.579 km
SC-400	39° 56.050′	−70° 55.669′	460.0 m	53.804 km
SE-400	40° 00.008′	−70° 44.495′	273.0 m	42.232 km
NE VLA	41° 00.000′	−70° 44.495′		
NW VLA	40° 22.103′	−71° 13.499′		

Table 3.1: Acoustic source and receiver geometry information. The 400 Hz sources are all 12 m above the bottom and the 224 Hz source is 5 m above the bottom. Positions are from survey data, rather than drop coordinates.

close to, yet dynamically-isolated from, the motion-sensitive hydrophone array. With a vertical aperture, it is possible to resolve the depth structure of the sound field, from which many physical properties of sound propagation may be inferred. The temporal resolution of the transmitted signal is increased by using specially-coded signals, as will be discussed in the next section. Following that, the necessary processing associated with a vertical array of sensors is presented.

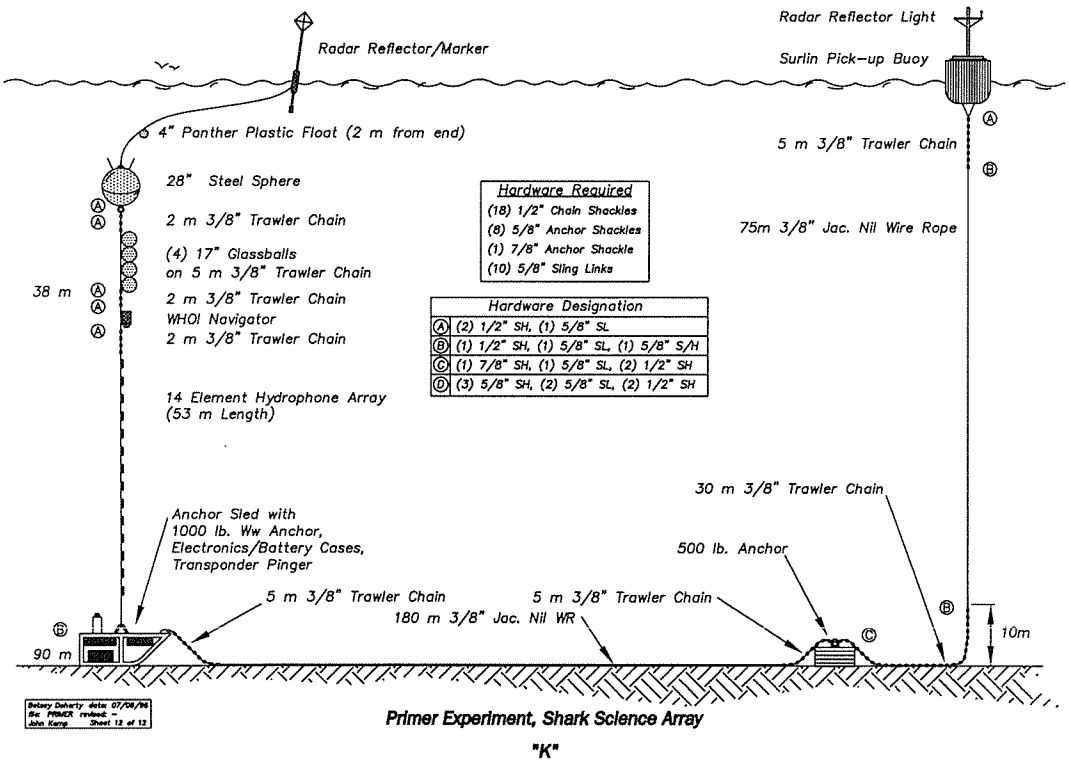

Figure 3-2: Deployment geometry of the northeast vertical line array.

3.2 M-Sequence Processing

3.2.1 Signal Design

The source transmission schedule was designed to provide good temporal resolution of effects from the rapidly-moving solitary waves present near the shelfbreak (PRIMER was *not*, however, designed to be an internal wave experiment), while at the same time conserving battery power. The signals transmitted were standard tomographic m-sequences (a.k.a. pseudorandom noise sequences, because of their close resemblance to random noise signals), which provide, after pulse compression, the best travel time resolution for a source with limited peak-power and a given bandwidth (Munk et al., 1995). Each 400 Hz source was programmed to transmit every 15 minutes, with individual sources timed so as to prevent simultaneous receptions from multiple sources. The 224 Hz source transmitted every five minutes on the hour. As an illustration of the transmission scheduling, Figure 3-3 shows a spectrogram of the receptions over a two-hour period, averaged over three adjacent hydrophones on the NE VLA.

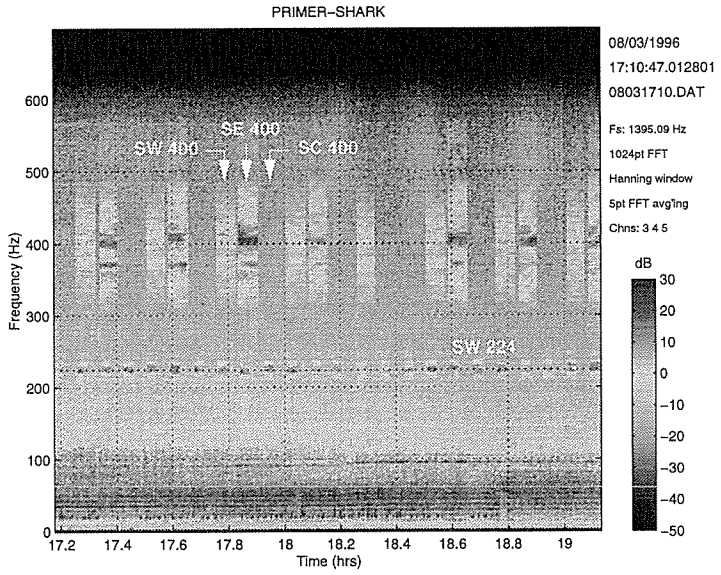

Figure 3-3: Spectrogram showing signal transmissions over a two-hour period, as received at the NE VLA. Labels indicate the source responsible for each arrival, including the time period where the central source would have transmitted.

Table 3.2 summarizes the sequence coding for each source. The 400 Hz sources (100 Hz bandwidth, $Q \simeq 4$) all had a 27% duty cycle, while the 224 Hz source (16 Hz bandwidth, $Q \simeq 14$) had a 39% duty cycle.

Source	Law	Digits	cpd	Seq. Period	Total Time	Xmits (min)
SW-224	103	63	14	3.9375 s	118.1 s	0,5,...,50,55
SW-400	1473	511	4	5.1100 s	245.3 s	0,15,30,45
SC-400	1175	511	4	5.1100 s	245.3 s	10,25,40,55
SE-400	1533	511	4	5.1100 s	245.3 s	5,20,35,50

Table 3.2: Source signal parameters. Indicated for each source are the octal law, digit length, cycles per digit (cpd) used to generate the m-sequence, duration of a single sequence, total transmission time, and transmission schedule.

3.2.2 Signal Recording

Traditional m-sequence tomography utilizes on-board pulse compression of the incoming data because of limitations in data storage capacity (Munk et al., 1995). For the SBPX, however, it was possible to store over twelve days of continuously-sampled data without any in situ processing. The NE VLA stored all data internally on a series of hard drives housed on the anchor sled. The drives contained sufficient storage capacity for over 50 gigabytes of data at modest sampling rates. A Delta-Sigma converter controlled the sampling rate, which was fixed at 1395.089286 Hz for the duration of the experiment. With a 5 megahertz reference clock, the sampling rate is given by $f_s = 5 \times 10^6/(256 \cdot n_1 \cdot 2^{n_2})$, where $n_1 = 7$ and $n_2 = 1$. All 16 channels were sampled simultaneously, with each hydrophone having a sensitivity of -170 dB re 1 V/μPa. The converters applied a lowpass FIR filter of constant 28 sample period group delay, and a flat bandwidth of 523 Hz (-3 dB at 572 Hz) (von der Heydt, 1996). Happily, not a single hydrophone channel on the northeast VLA failed.

3.2.3 Signal Processing

The signal processing required for the data was straightforward and consisted of the following steps: (1) extraction of the desired transmission event from the stored data

records, (2) bandpass filtering, (3) demodulation to obtain the complex envelope, (4) correction for timing errors, (5) pulse compression to remove the m-sequence coding, and (6) downsampling and truncating the data to reduce storage requirements. Additionally, in most cases, the 48 sequences were reduced to only 16 by averaging three consecutive sequences at a time. The duration of three consecutive sequences was determined to be well within the decorrelation time scale of the acoustic propagation path, thus allowing coherent averaging. Also, mooring motion was negligible on these time scales, so no correction for motion-induced Doppler shifting was required.

The time-corrected, pulse-compressed signal from the j^{th} hydrophone may be expressed in the form of a discrete Fourier transform:

$$s_j(n) = \frac{1}{N} \sum_{k=1}^{N} \left(P_j(k) W^*(k) e^{-i2\pi k (f_c/f_s)\theta_t} \right) e^{i2\pi kn/N}, \tag{3.1}$$

where P_j and W are, respectively, the demodulated Fourier transforms of the raw digitized signal at hydrophone j and a replica of the transmitted pseudorandom signal. The m-sequence carrier frequency is f_c (224 or 400 Hz), and f_s is the system sampling rate. The parameter θ_t is a phase correction accounting for timing errors introduced by non-integer sampling rates, clock drifts and any delays in writing the data to disk. For the 400 Hz transmissions, each sequence lasted 5.11 seconds. As sampled, this transmission duration was equivalent to a sequence length of 7128.91 samples, which was rounded up to 7129. Similarly, the 224 Hz sequences were rounded down to be of length 5493 sample points. After the pulse compression and demodulation, the 400 Hz receptions were downsampled by a factor of 4, and the 224 Hz receptions by a factor of 5. Because the final pulse-compressed arrival was much shorter than the 5.11 second sequence originally transmitted, only a one-second segment of data was saved for each reception.

Virtually all of the scheduled receptions were successfully processed. There were instances when the SE 400 Hz source completely failed to transmit, but those times were quite rare. Any receptions that fell across data file boundaries were discarded, and timestamps of successive data files were monitored to ensure that delays in writing

the data to disk did not affect the pulse compression. Typical write delays were on the order of 2–3 microseconds. The next section looks in detail at the characteristics of the processed data.

3.3 Reception Characteristics

Frequency Content

The spectrogram in Figure 3-4 shows a close-up of un-processed individual m-sequence arrivals at the NE VLA from the three operating sources. The 224 Hz source arrives every 5 minutes, and the SE 400 Hz (upper) and SW 400 Hz (lower) receptions arrive every 15 minutes, with five minute offsets between sources. The peak-to-floor spectrum level is 25 dB, where the plotting threshold has been set to just suppress the out-of-band noise. As would be expected, the SW 400 Hz arrival, which has to travel over a longer path, shows more attenuation than the SE 400 Hz signal. This is particularly evident by the lower signal levels toward the outer edges of the frequency band. The 400 Hz receptions shown in Figure 3-4 contain numerous nulls, or notches, in the spectra that appear stable over various periods of time. Similar instances of frequency-selective fading are seen in virtually all of the transmissions from both sources. Since the sources were not calibrated immediately prior to the experiment, this phenomenon could possibly be due to problems with the source waveforms. A more likely explanation, however, is that the nulls are the result of multipath interference effects that are stable over the time scales of 2–3 minutes.

Signal-to-Noise Ratio (SNR)

The primary purpose of using m-sequences is to improve the time resolution of signals received from a power-limited source. Time resolution can be shown to be a function of SNR. For this particular region of the continental shelf, the noise spectrum below 200 Hz is fairly high in amplitude, due to a combination of shallow water noise and shipping. Sea states during the summer experiment were reasonably calm, never

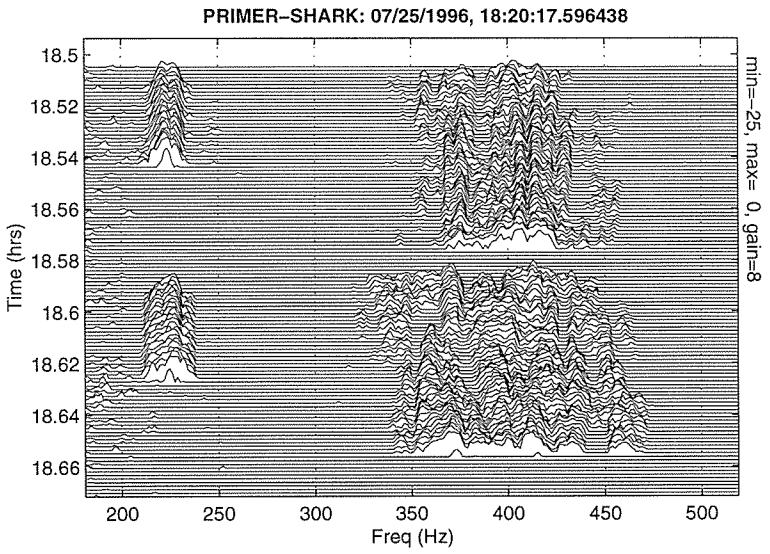

Figure 3-4: Spectrogram close-up of individual arrivals. Spectral slices are 5 seconds apart. Upper 400 Hz arrival is from SW, lower from SE. Plotting threshold has been set to just suppress out-of-band noise.

exceeding Sea State 3 (SS3).[2]

A standard exercise in acoustic propagation experiments is to construct a signal level table such as Table 3.3. Although this table oversimplifies the issues, it is often a useful tool. The two largest unknowns are the bottom attenuation, which depends on sub-bottom geoacoustic properties, and the reduction in signal levels because of scattering within the water column, such as from internal waves. A possible range of bottom loss values is given, while the scattering loss is left as an unknown. Transmission loss calculations based on propagation models suggest that, over the seven-day time span of SeaSoar data, the depth-averaged signal loss can range from 70 to 95 dB.

Typical single-channel SNR values, with no sequence averaging, were 24 dB and 20 dB for the SE400 and SW400 sources, respectively, and defined as the ratio between the mean signal levels over short time windows with and without a signal present. Recognizing that scattering losses have not been accounted for in the predictions, the measured and predicted SNR values are in reasonable agreement. With values for the SNR, a theoretical travel time resolution can be calculated and expressed as a root-

[2]Sea State 3 is defined as 7–10 knot wind speed with 3–5 foot seas.

Source Level	185 dB re 1μPa @ 1m
Spreading Loss (at 42 km)	-60 dB
Absorption Loss	(< 1 dB)
Bottom Loss	-30 to -10 dB
Scattering Loss	?
Received signal	95 – 115 dB
Noise spectrum level[a]	65 dB re 1 μPa (SS3)
Bandwidth 100 Hz (Q=14)	20 dB
Single-phone SNR	11 – 34 dB

[a]Urick (1983)

Table 3.3: Predicted source signal levels for the eastern edge 400 Hz signal path.

mean-square (RMS) error in measured travel time. For a given SNR and bandwidth, the RMS travel time error (σ_τ), say of the peak signal arrival, may be modeled as (van Trees, 1968)

$$\sigma_\tau = \frac{d}{\sqrt{SNR}}, \tag{3.2}$$

where d is the digit length used in the pseudorandom sequence and SNR is the signal-to-noise ratio. For an SNR of 25 dB and digit length of 10 milliseconds, the RMS travel time error is 2 milliseconds. For the 224 Hz source, the same SNR would result in $\sigma_\tau = 14.3$ msec.

Interference from Shipping

The main source of complication during the processing was signal contamination by nearby shipping. The spectrograms in Figure 3-5 show two examples of noise contamination at the NE VLA. In Figure 3-5(a), hyperbolic-like spectral lines, characteristic of a moving sound source in shallow water (Collins et al., 1994), are clearly visible. Although the lines appear to be a series of tones undergoing extremely large Doppler shifts, they are actually the result of Lloyd's mirror interference effects, which can be readily simulated with basic propagation models. In many instances the strong shipping noise exceeded the signal gain provided by the pulse compression, preventing extraction of any useful data. In Figure 3-5 the constant presence in both spectro-

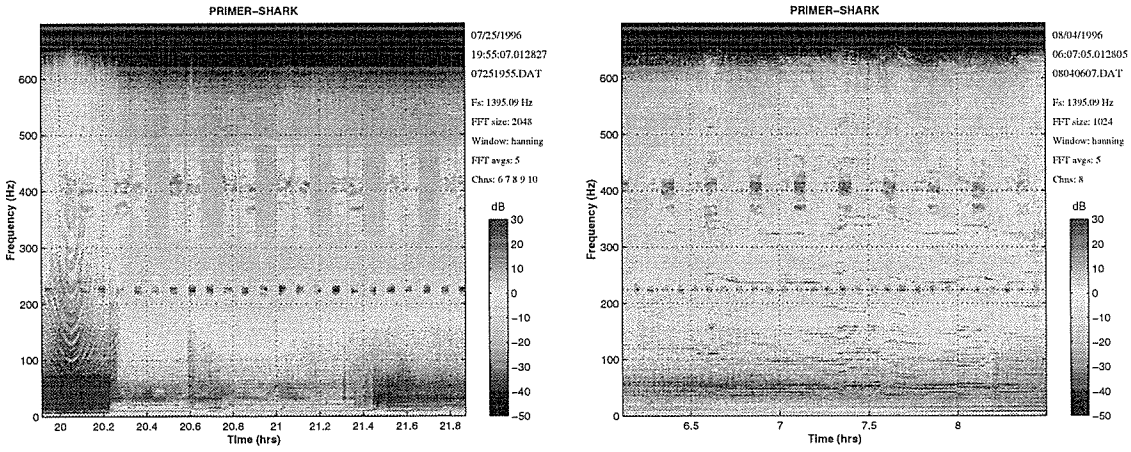

(a) Closest point of approach shipping noise phenomenon.

(b) Shipping noise.

Figure 3-5: Shipping noise as recorded on the northeast VLA.

grams of strong tones below 100 Hz is indicative of the ever-present level of shipping noise on the eastern continental shelf region. The spectrogram in Figure 3-5(b) is included to illustrate some of the variety seen in the shallow water noise field. The table in Appendix B details all of the transmissions that were affected by shipping noise.

Time Series

In Figure 3-6, an example of the depth structure of the pulse-compressed, demodulated receptions at the northeast VLA is shown for arrivals from the two 400 Hz sources. The SE 400 arrival has more energy than that from the SW 400 Hz source and tends to have a "cleaner" onset, both features likely due to the differences in path lengths. Characteristic of shallow water propagation, the initial arrival tends to be the strongest and is more abrupt, while the tail of the signal fades away in a more random fashion. It is difficult to see much vertical structure in the arrivals, and individual raypaths and/or modes are not discernible. It is situations such as this one that motivate the use of vertical receiving arrays. As discussed in the next section, having an array of sensors allows one to separate the signal into its component normal

modes by spatial filtering, even when the mode arrivals are overlapping in time.

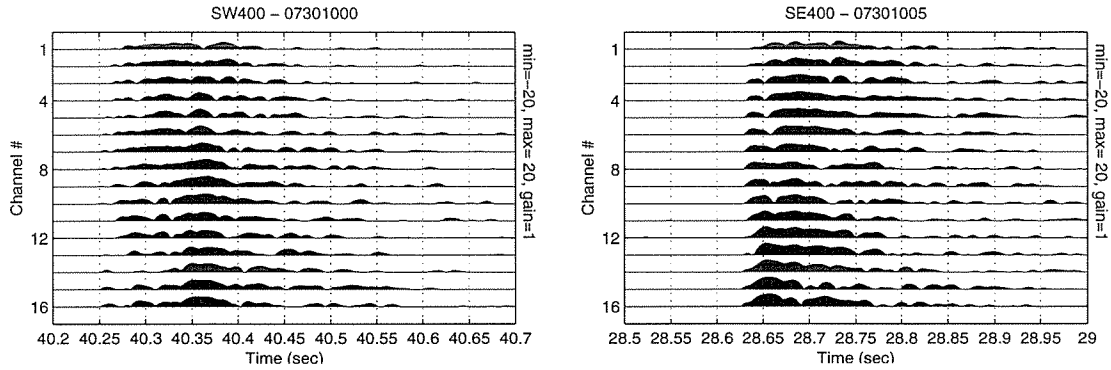

(a) SW400 Source Arrival

(b) SE400 Source Arrival

Figure 3-6: Arrival time series versus hydrophone number at the NE VLA.

3.4 Mode Filtering

A useful and physically-meaningful approach to analyzing acoustic propagation in shallow water is to model the acoustic pressure field as a weighted sum of normal modes, where an individual mode may be thought of as the coherent interference of up- and down-going plane waves having identical (though not arbitrary) grazing angles. For a single-frequency, or continuous-wave (CW), pressure field, the normal modes give the depth structure of the waveguide solutions to the homogeneous Helmholtz equation, which, for constant medium density $\rho(z) = \rho_o$, may be written as

$$\nabla^2 p(r,z) + k^2(r,z)p(r,z) = 0\,, \tag{3.3}$$

where p is the pressure field at range r and depth z, and k is the acoustic wavenumber. Assuming a locally-separable solution, $p(r,z) = \sum_m \psi_m(z)a_m(r)$, and cylindrical symmetry, the eigenvalue equation governing the local modeshapes is given by

$$\frac{d^2\psi_m(z)}{dz^2} + (k^2(z) - k_m^2(z))\psi_m(z) = 0\,, \tag{3.4}$$

where k_m is the horizontal wavenumber and ψ_m the modal eigenfunction associated with the mth mode. The modeshapes $\psi_m(z)$ form an orthogonal basis set, and by convention, are normalized so that $\int ||\psi_m(z)||^2 \rho^{-1} dz = 1$. The reason for using a vertical hydrophone array is to be able to spatially filter the pressure field in order to estimate the a_m, or local mode coefficients.

The acoustic pressure field from a CW source, as measured on an array with hydrophones at depths z_j, $j = 1, \ldots, N$, is commonly modeled as

$$p(z_j) = \sum_{m=1}^{M} a_m \psi_m(z_j) + n(z_j)$$

where M is the number of propagating modes at the receiver and n represents the noise contribution to the field measurement, p. In matrix form, the above equation becomes $\mathbf{p} = \mathbf{\Psi a} + \mathbf{n}$, where $\mathbf{p}$ and $\mathbf{n}$ are $N \times 1$, $\mathbf{a}$ is $M \times 1$ and $\mathbf{\Psi}$ is the $N \times M$ matrix of vertically-sampled modeshapes ($\{\mathbf{\Psi}\}_{jm} = \psi_m(z_j)$). An estimate of the mode coefficients, $\hat{\mathbf{a}}$, is typically formed using a linear combination of the array elements, written in general form as

$$\hat{\mathbf{a}} = \mathbf{H}^H \mathbf{p} = \mathbf{H}^H \mathbf{\Psi a} + \mathbf{H}^H \mathbf{n}\,, \tag{3.5}$$

where the matrix $\mathbf{H}$ represents a suitably-chosen linear operator, and $(\cdot)^H$ represents the Hermitian, or complex-conjugate transpose, operator.[3] The primary constraint to consider when mode filtering the PRIMER data is the array. The 16-element VLA spanned only the lower half of the 90 meter water column. Although the 16 sensors theoretically allow up to 16 modes to be estimated, the short aperture reduces this number. The properties of the noise vector, $\mathbf{n}$, also impact mode beamformer performance. The most common assumption made about the noise field is that it is Gaussian, spatially white (i.e., spatially uncorrelated) noise. It is known, however, that this assumption is not always a good model in shallow water, where surface

[3] Although the modeshapes $\psi_m(z)$ are real, in many array processing applications they are scaled by a complex exponential of the form $\exp(ik_m\delta)$ in order to correct for any tilt in the array.

noise can couple into the waveguide modes, becoming spatially correlated and more difficult to discriminate against spatially.

The mode filtering procedure used in this thesis is the sampled modeshape, or direct projection method, where the vector of estimated mode coefficients, $\hat{\mathbf{a}}$, is given by

$$\hat{\mathbf{a}} = \mathbf{H}^H \mathbf{p} = \mathrm{diag}(||\boldsymbol{\psi}_m||^{-2}) \boldsymbol{\Psi}^H \mathbf{p}\,, \tag{3.6}$$

where $\mathrm{diag}(q_i)$ indicates a diagonal matrix with elements q_i along the main diagonal. The method is straightforward and robust, particularly when the modeshapes are not well sampled, and it provides good rejection to spatially-uncorrelated noise (Buck et al., 1998). The scaling of the sampled modeshape matrix by $\mathrm{diag}(||\boldsymbol{\psi}_m||^{-2})$ eliminates any bias due to the lack of orthonormality of the sampled modes. Even so, there will still be some bias due to cross-talk, or leakage, between the modes. Figure 3-7 illustrates the levels of cross-talk for each mode estimate at 400 Hz. Each panel shows the mode filter output assuming a single-mode input. For modes 3 and below, leakage levels are all below 0.5. Above that, however, a single-mode input results in essentially a three-mode output response. Because of degraded estimates beyond mode 10, the modal analysis in this thesis will be limited to only the first ten modes, and even then, one must bear in mind the fact that there will be non-negligible leakage in the mode estimates for modes 3 and above.

Before moving on to a discussion of other issues related to the mode filtering problem, it is worth mentioning two other modal beamformers considered, but not utilized, in this work. The first is the pseudo-inverse (PI), or least-squares filter. The advantage of this filter is that it eliminates much of the cross-talk between the modes. The tradeoff is greatly-increased sensitivity to arrays that are poorly-conditioned (i.e., a short array aperture), such as the NE VLA (Sperry, 1994). Even with diagonal weighting to reduce sensitivity, the final performance of the PI using the NE VLA modeshapes was no better than with the sampled modeshape method. The second approach represents a departure from the direct projection and PI methods in that

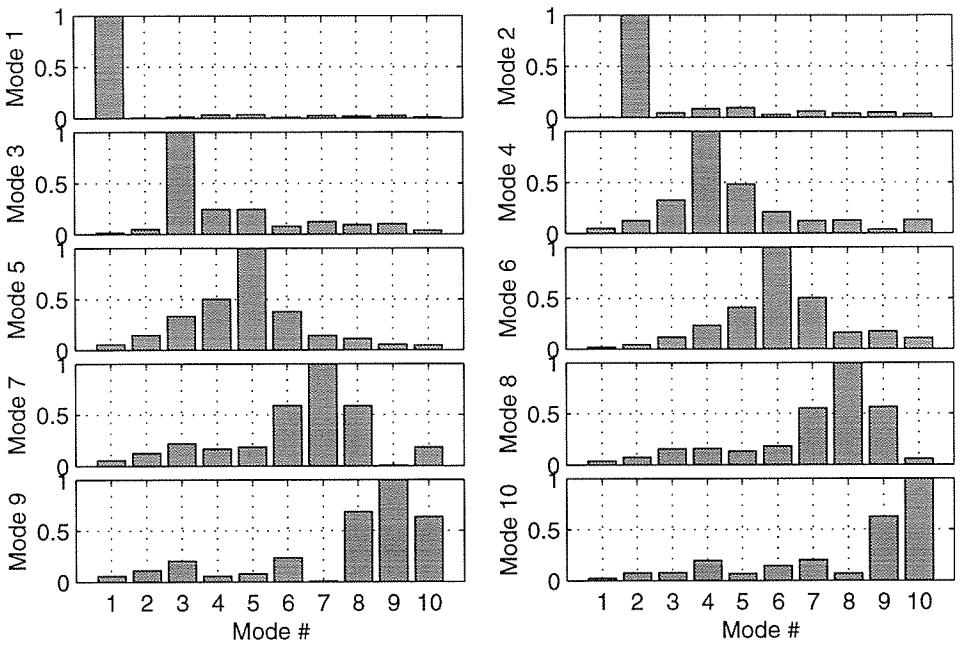

Figure 3-7: Modal cross-talk for the direct projection mode filter at 400 Hz.

it treats the mode coefficients as complex random variables with certain known, a priori statistics. The maximum a priori filter suggested by Buck et al. (1998), and the optimal mode filtering algorithm suggested by Chiu et al. (1997), are examples of such filters. The essence of the latter algorithm is that it provides additional constraints for estimating the mode coefficients based on the expected cross-correlation of the arriving modes. This is particularly useful in situations like PRIMER, where the receiving array undersamples the environment. The drawback, however, is that the cross-correlation matrix must first be estimated via a propagation model. Given the complicated oceanography in the PRIMER region, it is possible that the a priori correlation matrix would be mismatched to the actual environment, resulting in incorrect coefficient estimates.

The discussion so far has only considered mode filtering for a CW source. In PRIMER, the 224 and 400 Hz sources had bandwidths of 16 and 100 Hz, respectively. Both $\mathbf{\Psi}$ and $\mathbf{a}$ are functions of frequency, as shown in the broadband expression for

the received pressure field, p,

$$\mathbf{p}(t) = \int \mathbf{\Psi}(f)\mathbf{a}(f)e^{-i2\pi ft}df + \mathbf{n}(t)\,. \tag{3.7}$$

In the case of the NE VLA, the modeshapes, as sampled by the 16 array elements, do not vary substantially over the 350–450 Hz band, so it is possible to assume $\psi_m(z,f) \approx \psi_m(z,f_o)$, where $f_o = 400$ Hz. Equation (3.7) then becomes

$$\mathbf{p}(t) = \mathbf{\Psi}(f_o)\int \mathbf{a}(f)e^{-i2\pi ft}df + \mathbf{n}(t) = \mathbf{\Psi}_o\mathbf{a}(t) + \mathbf{n}(t)\,. \tag{3.8}$$

As verification of the approximation, several receptions were filtered with both the single-frequency filter and the more computationally-intensive broadband version, and the results were in good agreement with one another.

3.4.1 Time Dependence

The time dependence of the modeshapes can occur if there are large changes in sound speed at the array over short time periods. Passing solitons are the primary cause of such rapid changes, although any process that changes the sound speed field must be tracked regardless of how rapid. Rapidly-sampling thermistors attached to the VLA provided a means of tracking the sound speed profile. Even so, the two-minute thermistor sampling period was barely sufficient to keep up with the fluctuations. Figure 3-8 shows an example of how quickly the sound speed profile changes with the passing of a soliton. The three profiles pictured are separated by two-minute intervals. The change in sound speed at 40 meters depth is nearly 20 meters/second in just four minutes. The modeshapes used for the modal beamforming were updated every thirty seconds by interpolating between thermistor samples.

3.4.2 Array Motion

One final issue to consider when processing the VLA data for the mode coefficients is the effect of array motion due to local currents. The VLA was designed to be a

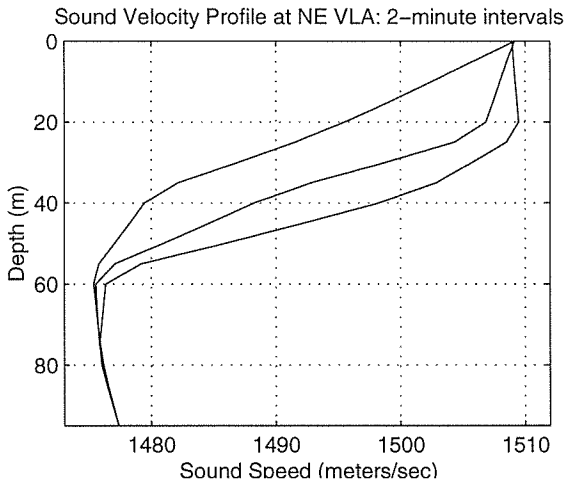

Figure 3-8: Sound speed profiles measured at NE VLA, separated by 2-minute intervals. Initial profile is at left/upper; final profile is at right/lower.

very stiff mooring, not susceptible to current motion. Additionally, the upper buoy on the VLA was kept far enough below the surface to avoid surface wave-induced motion. When a vertical array does move, the modal beamforming process is affected in two ways. First, the hydrophones are now at slightly different depths and thus sample the acoustic modeshapes differently than they would with a straight VLA. This is typically a very small effect. The second, more important effect, is that a leaning array presents a slight horizontal aperture, therefore a given mode will have a phase difference from one hydrophone to the next. The amount of this difference depends on how large the horizontal projection of the array is relative to the mode wavenumber, k_n. Using a set of transponders deployed to monitor the motion of the VLA, it was determined that the VLA motion was sufficiently small, and therefore negligible for the purposes of modal beamforming. Appendix A looks in more detail at the issue of tracking the motion of the array.

3.4.3 Mode Arrivals

Figure 3-9 shows the output of the mode beamforming for the SW 400 Hz source over a seven-day period. Each panel represents the modal energies averaged over a one-hour period each day during which there was SeaSoar sampling along the eastern leg.

There are many interesting features to note. For instance, there is a daily wander in the mode arrivals of over 100 milliseconds, and the relative arrival times of the individual modes varies daily as well. The changes in energy distribution amongst the modes is also variable. There appears to be roughly a 200 millisecond spread to the arrivals, although on some days, 7/27 in particular, it is less than 100 msec for the lower modes. In the next chapter, we will use propagation modeling tools based on the environmental data discussed in the previous chapter to develop an understanding of why the arrivals shown in Figure 3-9 look the way they do.

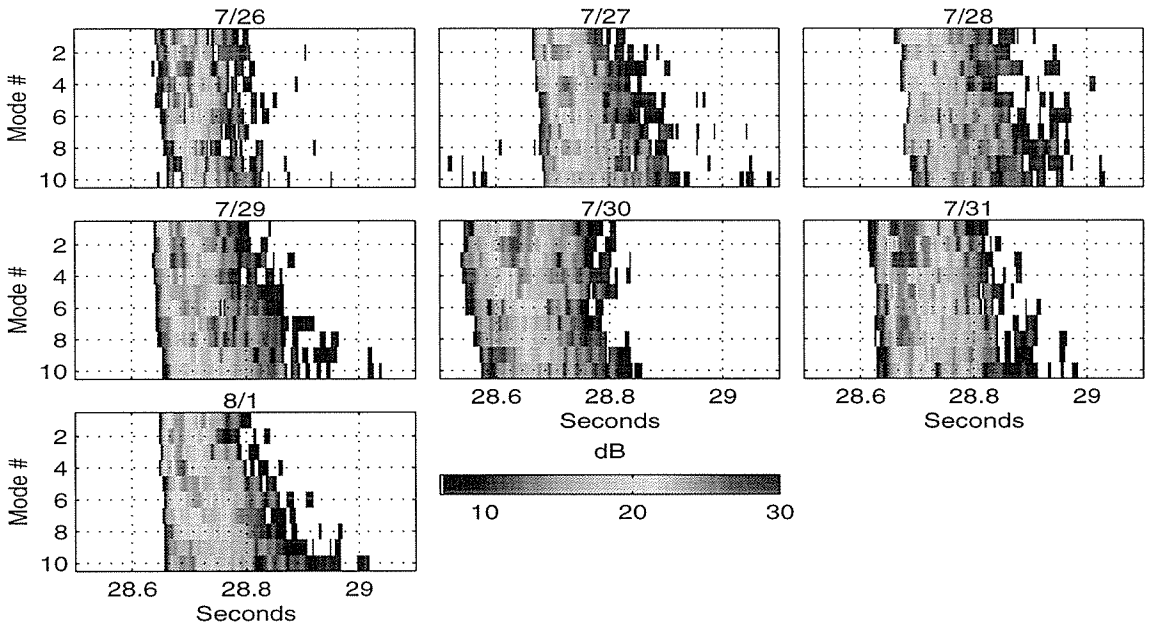

(a) Mode energy levels averaged over one hour.

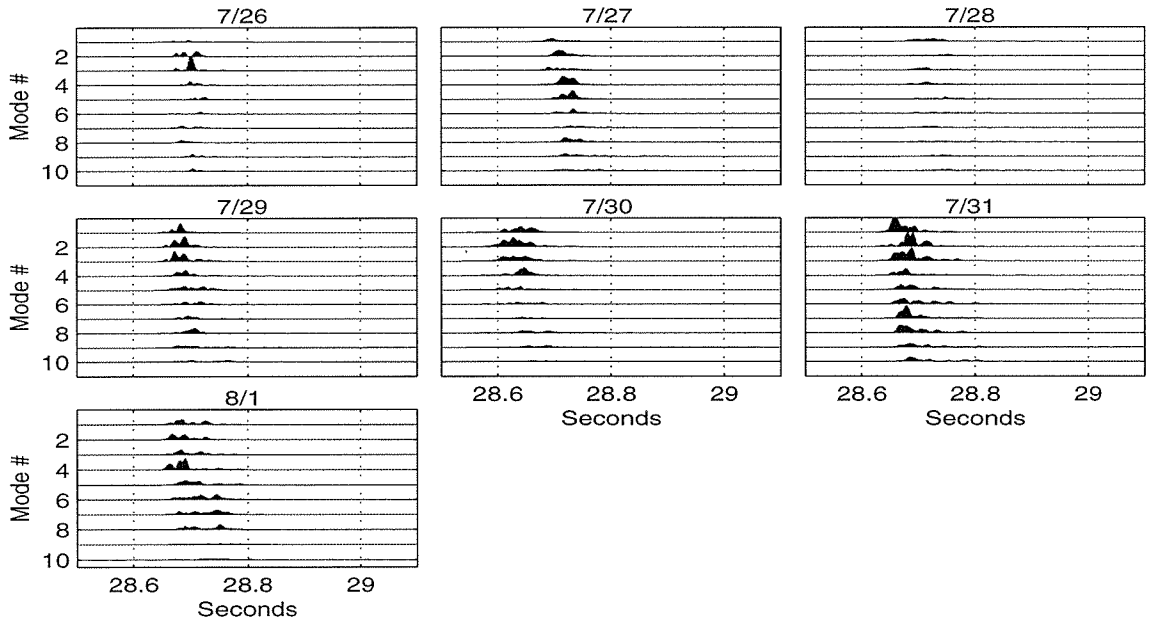

(b) Variance in mode energies over the one hour period.

Figure 3-9: Mode arrival energy for the first 10 modes from the SE 400 Hz source, averaged over a one-hour period during the middle of each SeaSoar transect along the eastern edge.

Chapter 4

Forward Propagation Study

4.1 Introduction

A major objective of the Shelfbreak PRIMER Experiment was to develop an understanding of acoustic propagation in a very complex region of the ocean. Because of the range- and time-varying nature of the environment, it is very difficult to infer the state of the ocean strictly from the recorded acoustic data, that is, to know exactly what the channel "response" is of the shallow water waveguide. It therefore becomes necessary to have a model of the underlying propagation physics. With such a model, one can relate particular features in the recorded data to one or more aspects of the propagation, such as acoustic mode coupling at the interface between two water masses. It should not be a surprise that the quality of the acoustic propagation model output is only as good as the environmental data which is input. Thus, one of the PRIMER objectives was to collect very high quality oceanographic measurements. This chapter on propagation modeling presents a series of simulations that describe the variability of acoustic propagation near the shelfbreak front. Some of the comparisons between model results and results from the experiment are found in the subsequent chapter, which looks closely at the recorded data.

4.2 Range-Dependent Normal Mode Theory

In many acoustic propagation situations it may be reasonable to assume that the environment (e.g., water depth, sound speed field, geoacoustic properties of the sea bottom) do not vary significantly along the propagation path. Such an assumption leads to greatly-simplified propagation physics. Brekhovskikh and Lysanov (1990), however, cite three instances in which range variability must be carefully considered: (1) sound propagation in a coastal wedge; (2) propagation across frontal zones; and (3) very long range propagation. The Shelfbreak PRIMER experiment firmly encompasses the first two cases, and though it does not qualify as long range propagation, it actually adds a fourth instance: propagation in shallow water where fluctuations from the internal wave field are strong. The purpose of this present section is to review the theoretical framework of range dependent mode propagation as applicable to propagation near the shelfbreak front. In particular, the governing equations are discussed, along with approximations and numerical implementations.

The starting point for the discussion on normal mode propagation theory is the Helmholtz equation for the acoustic pressure p, assuming cylindrical symmetry and a point source located at coordinates $r = 0, z = z_s$:

$$\frac{1}{r}\frac{\partial}{\partial r}\left(r\frac{\partial p}{\partial r}\right) + \rho\frac{\partial}{\partial z}\left(\frac{1}{\rho}\frac{\partial p}{\partial z}\right) + k^2(r,z)p = -\frac{\delta(r)\delta(z-z_s)}{2\pi r}\,. \tag{4.1}$$

Density, ρ, is assumed to be only a function of depth, while the wavenumber, $k(r,z) = \omega/c(r,z)$, varies in both range and depth. When the sound speed c is a function of depth only, Eqn. (4.1) is readily solved via separation of variables; the separation between z-dependent terms and r-dependent terms can be made completely. With c a function of both range and depth, however, the solution for the acoustic pressure field takes the form

$$p(r,z) = \sum_m \Phi_m(r)\psi_m(r,z)\,,$$

where the vertical modeshapes ψ_m vary with range, and $\Phi_m(r)$ is the mode coefficient

for mode m.

Substituting the above expansion for p into Eqn. (4.1), and applying the cross-product operator $\int \rho^{-1}(\cdot)\psi_m dz$, leads to, after some reorganization, two equations, one for the mode coefficients Φ_m, and another for mode functions, ψ_m (Jensen et al., 1994). The equation for equation for ψ_m is

$$\rho(z)\frac{\partial}{\partial z}\left[\frac{1}{\rho}\frac{\partial\psi_m(r,z)}{\partial z}\right] + [k^2(r,z) - k_m^2(r)]\psi_m(r,z) = 0\,, \tag{4.2}$$

where k_m is the mode m horizontal wavenumber, and each ψ_m is subject to certain boundary conditions that depend on how the seafloor and sea surface are modeled.

The range function for mode m, Φ_m, is determined by solving

$$\frac{1}{r}\frac{d}{dr}\left(r\frac{d\Phi_n}{dr}\right) + \sum_m 2B_{mn}\frac{d\Phi_m}{dr} + \sum_m A_{mn}\Phi_m + k_n^2(r)\Phi_n = -\frac{\delta(r)\psi_n(0,z_s)}{2\pi r}\,, \tag{4.3}$$

where A_{mn} and B_{mn}, the coupling coefficients between modes m and n, are given by

$$A_{mn} = \frac{1}{\rho}\int \frac{1}{r}\frac{\partial}{\partial r}\left(r\frac{\partial\psi_m}{\partial r}\right)\psi_m dz\,, \qquad B_{mn} = \frac{1}{\rho}\int \frac{\partial\psi_m}{\partial r}\psi_m dz\,. \tag{4.4}$$

Because of the coupling between the individual modes, one must solve the equation for all modes with non-zero A_{mn} or B_{mn} simultaneously. It is possible to solve Eqn. (4.2) and Eqn. (4.3) via finite difference methods, but such computationally-demanding calculations are limited mainly to determining reference solutions. There exist several possibilities for simplification, two of which will be discussed here, the adiabatic and one-way coupling approximations.

In the adiabatic approximation, first suggested by Pierce (1965), the coupling coefficients A_{mn} and B_{mn} are assumed to be negligible, thereby uncoupling the Φ_m while still allowing the modeshapes ψ_m to vary with range. Under the adiabatic approximation, the solution for p is given by

$$p(r,z) = \frac{e^{i\pi/4}}{\rho\sqrt{8\pi r}}\sum_{m=1}^{M}\frac{\psi_m(0,z_s)}{\sqrt{k_m(r)}}\psi_m(r,z)e^{i\int_0^{r'}k_m(r')dr'}\,. \tag{4.5}$$

This approximation is strictly valid only when the coupling coefficients are negligible, or in other words when the horizontal sound speed gradients are small relative to the mode interference lengths. Written as a constraint on the acoustic frequency, f, one has (Milder, 1969)

$$f \ll f_{adiab} = c^2 / R_{mn}^2 \left\langle \frac{\partial c}{\partial r} \right\rangle^{-1} , \tag{4.6}$$

where $R_{mn} = 2\pi/(k_m - k_n)$ is the mode interference length. Desaubies et al. (1986) have actually shown that the adiabatic approximation breaks down even sooner than predicted by the above condition because of improperly accounting for modal phases. In spite of the above limitations, adiabatic propagation is often assumed in strongly range-dependent situations because of the valuable insight it provides. Indeed, the adiabatic solution will be used later in this chapter as a point of reference for the modeled acoustic receptions that do include mode coupling.

The one-way coupled mode formulation is a simplification of the step-wise coupled mode solution suggested by Evans (1983). The former has been used as the basis for many coupled-mode numerical propagation models. One begins by assuming that the environment may be broken into a series of range-independent segments over which the local modeshapes can be considered invariant. The exact number of segments required will vary depending on the degree of range dependence. The solution for the acoustic field within segment j may be expressed as (Jensen et al., 1994)

$$p^j(r,z) = \sum_{m=1}^{M} \left[a_m^j H1_m^j(r) + b_m^j H2_m^2(r) \right] \psi_m^j(z) , \tag{4.7}$$

where $H1$ and $H2$ are ratios of Hankel functions representing forward- and backward-propagating modes, and a_m and b_m are the respective mode coupling coefficients. The one-way coupling approximation ignores the energy in the backscattered direction (i.e., the b_m terms), an approximation that is generally quite good. A further simplifying assumption is the single-scatter approximation, which ignores all but first-order scattering terms. The resulting equations can be implemented in an efficient march-

ing scheme (Jensen et al., 1994). If $\mathbf{a}^j$ is the vector of forward propagating mode coefficients in the jth segment, the coefficients for the next segment are given by

$$\mathbf{a}^{j+1} = \mathbf{R}^j \mathbf{a}^j \,, \tag{4.8}$$

where,

$$\left\{\mathbf{R}^j\right\}_{mn} = \frac{1}{2}\left(\int \frac{\psi_m^{j+1}(z)\psi_n^j(z)}{\rho_{j+1}(z)}dz + \frac{k_n^j}{k_m^{j+1}}\int \frac{\psi_m^{j+1}(z)\psi_n^j(z)}{\rho_j(z)}dz\right)\sqrt{\frac{r_{j-1}}{r}}e^{ik_m^j(r-r_{j-1})} \tag{4.9}$$

The two terms within the parentheses represents pressure and velocity matching conditions, respectively, from mode m to mode n across the segment interface, and the tailing exponential represents the phase accumulation across the jth segment. Propagating the field from source to receiver is then simply a matter of multiplying a series of matrices together:

$$p(r_J, z) = \Psi^J \mathbf{R}^J \ldots \mathbf{R}^2 \mathbf{R}^1 \mathbf{a}^1 = \Psi^J \mathbf{R}_{eff} \mathbf{a}^1 \,. \tag{4.10}$$

$\mathbf{R}_{eff}$ represents the effective coupling matrix of the entire waveguide between source and receiver. Eqn. (4.10) forms a useful conceptual picture of coupled mode propagation. It also highlights the difficulties associated with inverting the received field, p, for environmental perturbations when mode coupling is present. Sufficiently-detailed environmental data must be known a priori in order to construct the $\mathbf{R}^j$ necessary to develop a reference solution about which a linear inverse may be applied. If the coupling coefficients were instead considered unknowns to be inverted for, then the number of observation points required is dramatically increased.

While the physical interpretation of propagation provided by normal mode theory is very useful, a fully-coupled normal mode solution becomes computationally impractical as the complexity of the modeled environment grows. At every range step the matrix $\mathbf{R}^j$ must be computed. An alternate approach to computing acoustic fields in highly range-dependent environments is to use parabolic equation (PE)

methods. This will actually be the approach followed for the propagation modeling presented in this thesis. PE methods achieve their increased efficiency by transforming the traditional elliptic wave equation, which the normal mode method solves, into a parabolic equation by means of (in a simplified view) the paraxial approximation, which eliminates the second-order range derivative under the assumption that

$$\left|\frac{d^2p}{dr^2}\right| << \left|2k\frac{dp}{dr}\right| .$$

PE codes, however, solve for the complex pressure field, p, and do not directly provide any information about the normal modes. Therefore it is necessary to project the PE field onto the local modeshapes in order to obtain the actual mode coefficients, as given by

$$a_m(r) = \int_0^H p^{(PE)}(r,z)\rho(z)^{-1}\Psi_m(z;r)dz . \tag{4.11}$$

In spite of this additional step, the combined PE/mode decomposition approach is more efficient than a coupled-mode program, and has been the method of choice for several investigators (Colosi and Flatté, 1996; Preisig and Duda, 1997). The particular PE code used in this thesis, RAM, was developed by Mike Collins (Collins, 1994, 1993), and uses a wide-angle Padé approximation, making it ideally-suited for shallow water applications in which there may be energy propagating at high grazing angles. For simulations involving only mesoscale variability, a range stepsize, Δr, equal to one wavelength was used. This fairly conservative increment assured convergence of the acoustic field. When the higher-frequency soliton field was included, step sizes were reduced. In all cases the depth increment, Δz, was set to 0.5 meters.

All normal mode calculations were done using the Kraken code, developed by Michael Porter (Porter, 1991). Whenever modal decompositions were performed, care was taken to ensure that both PE and normal mode calculations were done using exactly the same environment, including any interpolation done internal to the codes themselves.

4.3 Propagation Analysis

4.3.1 Reference Propagation Environment

As a first step in analyzing the characteristics of acoustic propagation in the shelf-break region, it is useful to establish a reference propagation environment that can be used for comparison with more realistic, but complicated, scenarios. The following three sections describe the details of the reference environment, while the subsequent sections look at the resulting propagation characteristics. Since the time scales for variability in the bottom properties are sufficiently longer than time scales of interest here, the bathymetry and geoacoustic properties defined here will be treated as constant throughout the propagation studies of this thesis.

Bathymetry

Figure 4-1 shows bathymetric sections along the eastern and diagonal propagation paths to the northeast VLA. The data were taken from the National Ocean Survey (NOS) Digital Bathymetric Soundings, as distributed by the National Geophysical Data Center (NGDC). Comparisons of the data with shipboard echosounder data indicated that the two datasets are in good agreement, with variations on the order of 2–3 meters. The initial upslope portion of both propagation paths is relatively steep, reaching a maximum slope of 2.5° on the eastern path. It is less steep on the continental shelf.

Water Column Sound Speed Profile

Acoustic propagation models require sound speed values from the sea surface to beneath the ocean floor, and along the entire path from source to receiver. The SeaSoar transects, however, did not extend as far north and east as the northeast VLA. Though the thermistor data at the VLA could have been used to extend the SeaSoar data the remaining few kilometers, it was easier, and not significantly in error, to simply extend the nearest SeaSoar grid point to include the VLA location. More problematic was the limited SeaSoar flight depth of 120 meters. This limitation meant that for the

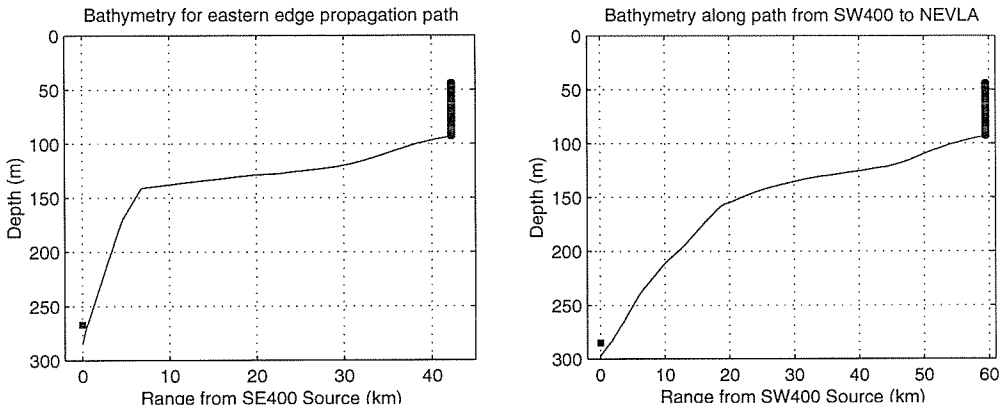

(a) SE source to NE VLA.

(b) SW source to NE VLA.

Figure 4-1: Bathymetric sections along acoustic propagation paths.

first 20 kilometers of the propagation path, the thermohaline field required extrapolation down to the seafloor, sometimes as deep as 300 meters. The extrapolations were done by merging the SeaSoar data in a smooth fashion with an average temperature profile from the AXBT data. Extrapolations of the salinity field were made using a salinity profile from one of the deep-water CTD casts further off the shelf. For depths below 150 meters, the AXBT data showed good agreement with climatology for the region (Linder, 1996). This agreement suggests that the assumption of static oceanography for the lower depths is not unreasonable.

After extrapolating, the next step was to define an "average" water column. Figure 4-2 shows the cross-shelf sound speed section computed by averaging the SeaSoar data in the along-shelf direction and also over the seven-day deployment period. The strong duct around 30–80 meters depth is a result of the colder, less saline shelf water. The thermocline is quite strong during this time period, owing to the relatively calm July weather during the experiment. The sharp contrast of the shelfbreak front has been removed from the propagation path by the averaging, although the foot of the front remains clearly visible beneath the pool of cold shelf water. It is interesting to note the very close resemblance of the reference profile discussed here, to the climatological temperature field for the summer, shown earlier in Figure 2-2. The general shape of the cold pool and its location relative to the shelfbreak are quite similar. The

decrease in sound speed below 150 meters in depth, a feature captured in both the AXBT and climatology data, actually represents the start of the deep-water sound channel, or SOFAR (SOund, Fixing And Ranging) duct.

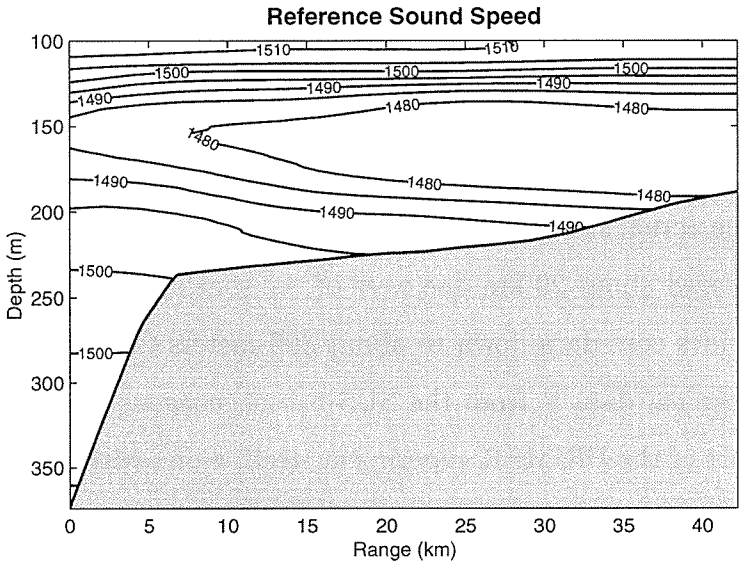

Figure 4-2: Cross-shelf section of sound speed from SeaSoar data, averaged over 50 kilometers in the along-shelf direction and over a seven-day period. SE 400 Hz source is at 0 km, NE VLA at 42.2 km.

Geoacoustic Effects

With a representative sound speed model for the water column established, the impact of the sea floor geoacoustic properties on the acoustic field in the water may now be estimated. A typical sediment profile taken in the region of the PRIMER experiment would likely consist of an upper layer of Holocene sands, 5–20 meters deep, followed by up to 200 meters of horizontally-stratified layers which contain various mixes of silt, sand and clay material from the Pleistocene era (Potty and Miller, 1999). The sandy surface layer may be composed of medium to coarse grained sands, or even gravel, in some locations. A range of typical geoacoustic parameters for such bottoms is listed in the table below (Hamilton, 1980).

While the continental shelf areas surrounding the PRIMER site have been well-studied, there is virtually no published geoacoustic data available for the upper 100

Composition	ρ [gm/cm^3]	c_p [m/s]	α_p [dB/λ]
Clay	1.5	1500	0.2
Silt	1.7	1575	1.0
Sand	1.9	1650	0.8
Gravel	2.0	1800	0.6

Table 4.1: Typical geoacoustic parameter ranges for a range of bottom layer compositions common to the continental shelf. Shear parameters are essentially negligible for present considerations.

meters within the actual study region. An Atlantic Margin Coring (AMCOR) Project drill site was located about 20 km due west of the southwestern corner of the experiment, and provides core data down to about 300 meters (Richards, 1977). Another source of geotechnical data is from the SUS-based geoacoustic inversions that were performed as part of the PRIMER experiment itself, along with several shallow cores that were done post-experiment (Potty and Miller, 1999). Profiles of compressional velocity and density are shown in Figure 4-3, for both the AMCOR and recent geoacoustic inversion results from the University of Rhode Island (URI).

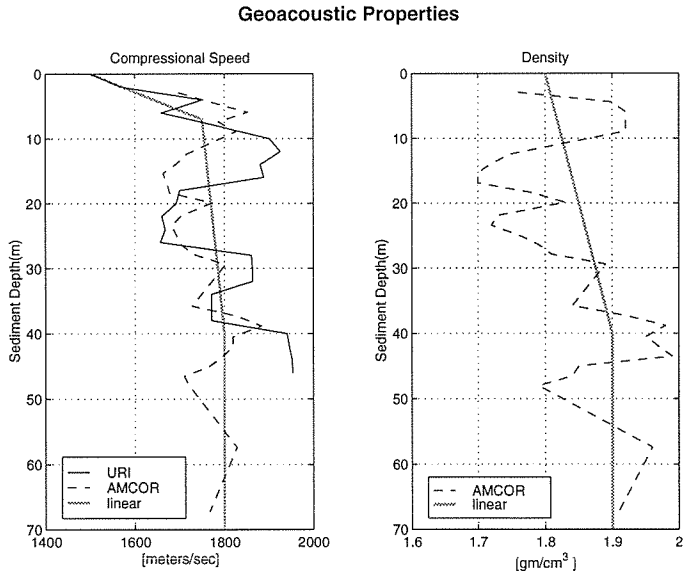

Figure 4-3: Geoacoustic models for compressional sound speed and density.

Figure 4-4 shows the results of a simple parameter study performed to determine propagation sensitivity to geoacoustic parameters. Four models were considered, the URI and AMCOR datasets, a uniform bottom with a sound speed of 1900 m/s and

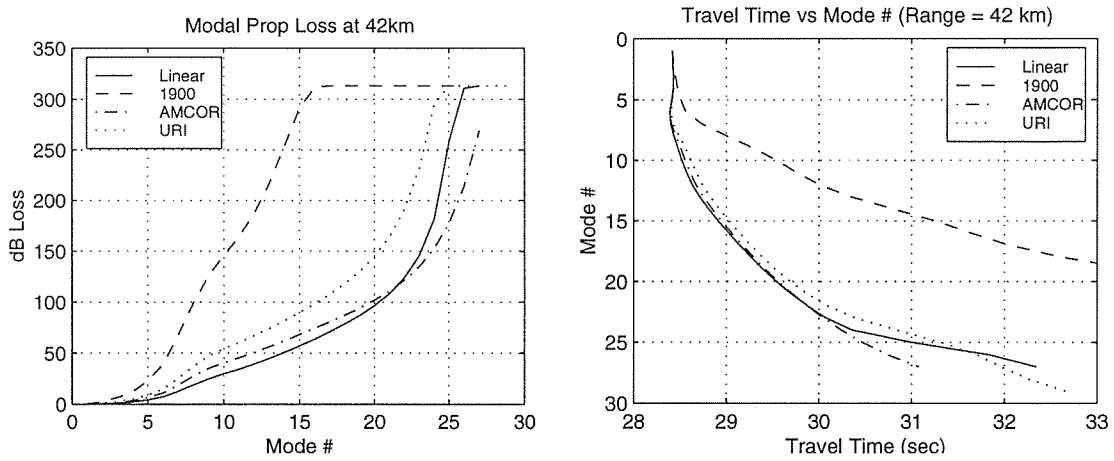

(a) Propagation loss

(b) Total travel time

Figure 4-4: Geoacoustic parameter study results.

density of 1.9 gm/cm^3, and a segmented linear fit to the AMCOR/URI models. The linear fit model, while retaining the important near-surface sound speed gradient, has the advantage of not permitting any modes to be trapped within bottom layers. Their presence creates numerical difficulties when projecting the PE pressure field onto the local modes. While such trapping phenomena may occur in reality, such trapped modes would quickly attenuate.

Looking first at the total propagation loss per mode in Figure 4-4(a), there is good agreement between the models (1900 m/s case aside) for the fully-trapped modes (1–5). The models suggest that for modes 10 and above, the bottom loss will be significant ($\geq$ 50 dB). Similar to what was seen in Figure 4-4(a), the travel time sensitivity shown in Figure 4-4(b) reveals that, except for the 1900 m/s bottom model, all models are in relatively good agreement. Given the above, it is reasonable to use the linear-fit model, and adjust the bottom attenuation parameter until the general energy levels from the synthetic data are in general agreement with the real data. Based on comparisons between synthetic and measured data, it appears that an attenuation level of around 0.7 dB per wavelength is sufficient. As well as accounting for actual energy loss into the bottom, the above attenuation level also serves as a compensating factor for propagation and scattering mechanisms that may affect the

overall field intensity, but are not modeled. Recent coring work suggests that the attenuation levels may be somewhat lower than those used here (Potty, 1999), although work still remains to be done before the values are finalized.

Modal Propagation

Before considering the full scale of environmental variability, it is important to understand the characteristics of the normal mode field within the reference waveguide. Particular items of interest include the efficacy of the source in exciting the mode field, how energy is coupled between the modes, and the propagation velocities and dispersion characteristics of the individual modes.

During the summer PRIMER experiment, each of the 400 Hz sources was moored just 12 meters above the bottom. In looking at Figure 4-2, it is clear that a deep source is not the most efficient way of getting sound into the shelf waters; a source located mid-water, within the cold water duct, would be optimal. With the PRIMER experiments, engineering practicalities dictated that the source be placed very near the bottom. In particular, such placement substantially reduces mooring motion. To understand how the sound field is affected by the upslope propagation, PE simulations were made using the environment described earlier, and the computed pressure field projected onto the local modeshapes at each range step. Figure 4-5 shows how the mode amplitudes vary as a function of range and mode number, and Figure 4-6 compares just the initial and final mode amplitudes for the SE 400 source. Because both the diagonal and eastern paths show very similar behavior, the rest of this chapter will focus only on the eastern propagation path.

Looking first at the initial mode amplitudes at the source, the pattern is consistent with that of a near-bottom source exciting only the higher modes which have non-zero amplitudes near the bottom. The source depth passes through zero-crossings of the modeshapes as mode number increases, giving rise to the null at around mode 21. The anomalously-large amplitudes in modes 5, 7 and 9 are because those particular mode numbers correspond to modes that are trapped in the narrow duct just above the ocean bottom. The deep source directly excites these modes, which couple well

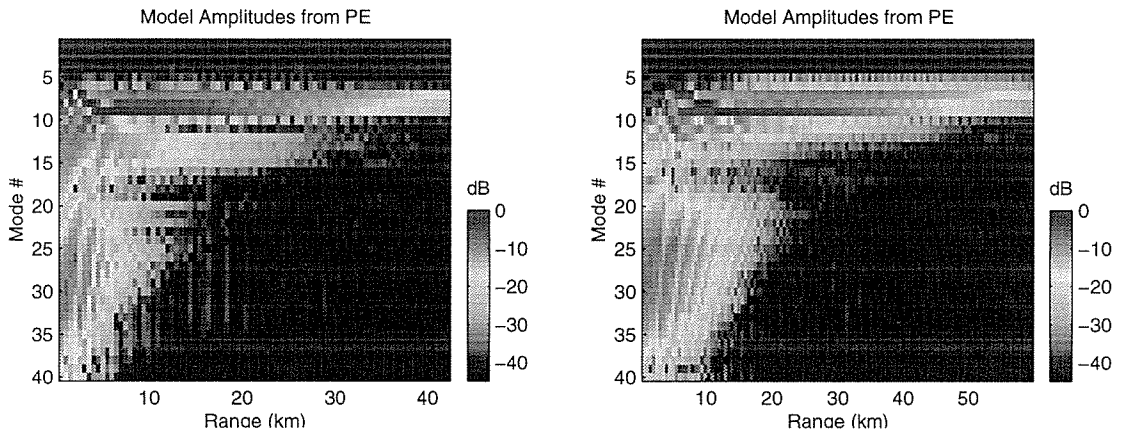

(a) Eastern Path

(b) Diagonal Path

Figure 4-5: Evolution of mode amplitudes at from single-frequency (400 Hz) PE simulations using a range-independent profile.

into higher modes (10–15) that are not trapped in the lower duct but do extend all the way to the bottom. One expects the number of trapped modes to vary from day to day, and also with frequency.

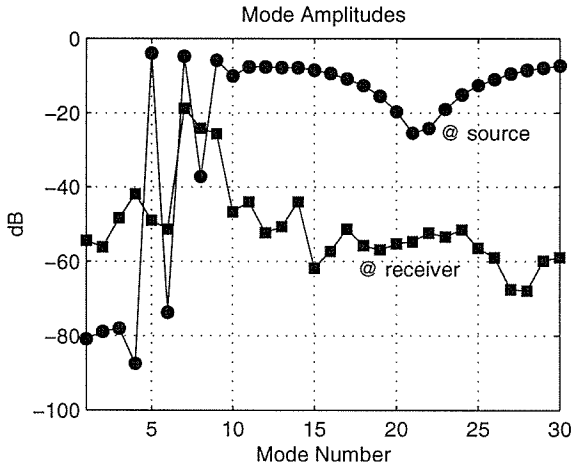

Figure 4-6: Comparison of initial and final mode amplitudes at 400 Hz, for the SE400 source to NE VLA.

The primary effect of the slope is to strip away energy in the higher modes. The energy in modes 10–20 is able to propagate onshore reasonably well without excessive energy loss. For most of the shelf propagation path, modes 5 and lower are non-bottom interacting. Though much energy is lost into the bottom, some energy does

couple into the lower modes and so is not entirely lost. At the receiving VLA there are roughly 20 modes with angles below critical in this simulation. Cylindrical spreading loss is *not* included in these simulations since it is uniform with mode number, and it hinders the presentation of mode amplitudes with range. An important conclusion that may be drawn at this point in the analysis is that given the PRIMER source location near the bottom, it is highly unlikely that bathymetric-induced coupling transferred energy into modes five and below, as was seen in the data shown at the end of Chapter 3.

Aside from the distribution of energy across mode space, the other aspect of the background propagation to consider is the temporal behavior of the signals. Two questions in particular one might ask are: Which modes are fastest, and how much dispersion is there? One factor greatly complicating the propagation is the fact that the sound channel near the source is more representative of a deep water sound channel, where the higher modes travel faster than the lower modes. Near the receiver, the channel is more typical of shallow water environments, where mode 1 is the fastest. Figure 4-7 shows the group velocities as a function of range for the first 20 modes. The key item to note here is that the fastest path through "mode space", from source to receiver, is to propagate in mode 6 until the 30 kilometer mark, and then couple into mode 1 for the remainder. An example of exactly this phenomenon appears in a later section on coupling due to solitary waves.

Figure 4-8 shows the mode arrivals for the reference environment under adiabatic propagation conditions and uniform excitation levels for each mode. In contrast to standard shallow water propagation, modes 6 and 7 are actually the fastest modes. Referring back to Figure 4-7, it can be seen that some of the higher modes have faster propagation velocities over more of the propagation path, up until ranges where the sound speed profile is more typical of a shallow water profile.

Horizontal Refraction

It is well known that acoustic propagation at oblique angles to a sloping bottom can result in a deflection, or refraction, of the direction of propagation (See, e.g.,

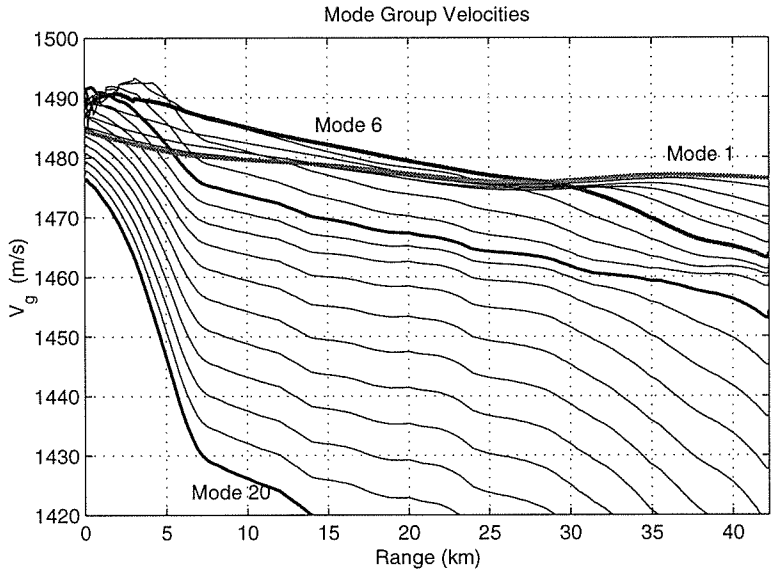

Figure 4-7: Modal group velocities at 400 Hz for eastern propagation path. Note the y-axis is truncated at 1420 m/s. Modes 1–20 are always propagating.

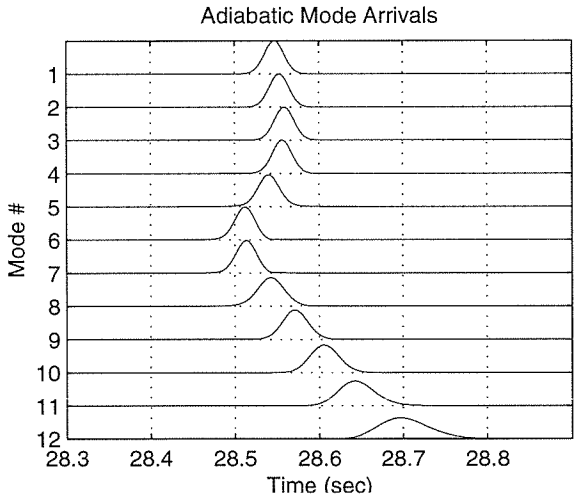

Figure 4-8: Adiabatic mode arrivals for the reference propagation environment.

Brekhovskikh and Lysanov, 1990). In terms of normal mode theory, this may be seen by noting that modal phase speeds decrease with a shoaling bottom (provided the sound speed does not drastically change), and that acoustic energy will always refract toward regions of slower sound speed (a.k.a. Snell's Law). To estimate the effects of horizontal refraction for the PRIMER experiment, the "horizontal ray/vertical mode" theory developed by Weinberg and Burridge (1974) was applied using the USGS bathymetry for the region and a 3-D sound speed field constructed from SeaSoar data. In the worst case scenario, the differences in mode travel times between straight line propagation and the horizontally-refracted path were less than a millisecond. Straight-line propagation from source to receiver will therefore be assumed. Appendix C gives a more detailed discussion of the horizontal refraction calculations and results.

4.3.2 Mesoscale Oceanography Effects

Mesoscale fluctuations in the region of the continental shelfbreak can be considerable and their effects on acoustic propagation often dominate other influences. This section looks specifically at the shelfbreak front and how its presence affects the acoustic modal energy distribution and the modal time series. Using the large-scale oceanography provided by SeaSoar, sound speed sections along the eastern edge of the experiment region were extracted. For each of these seven daily snapshots, parabolic equation acoustic propagation runs are made, and the results compared. Figure 4-9 presents the sound speed fields for the seven sections. Local sound speed gradients reach a maximum during Day 6, where changes are of the order 3 m/s over one kilometer and 30 m/s over 15 kilometers. The fact that the front has relatively high gradients in both temperature and salinity contributes to the large difference in sound speed going from slope to shelf waters.

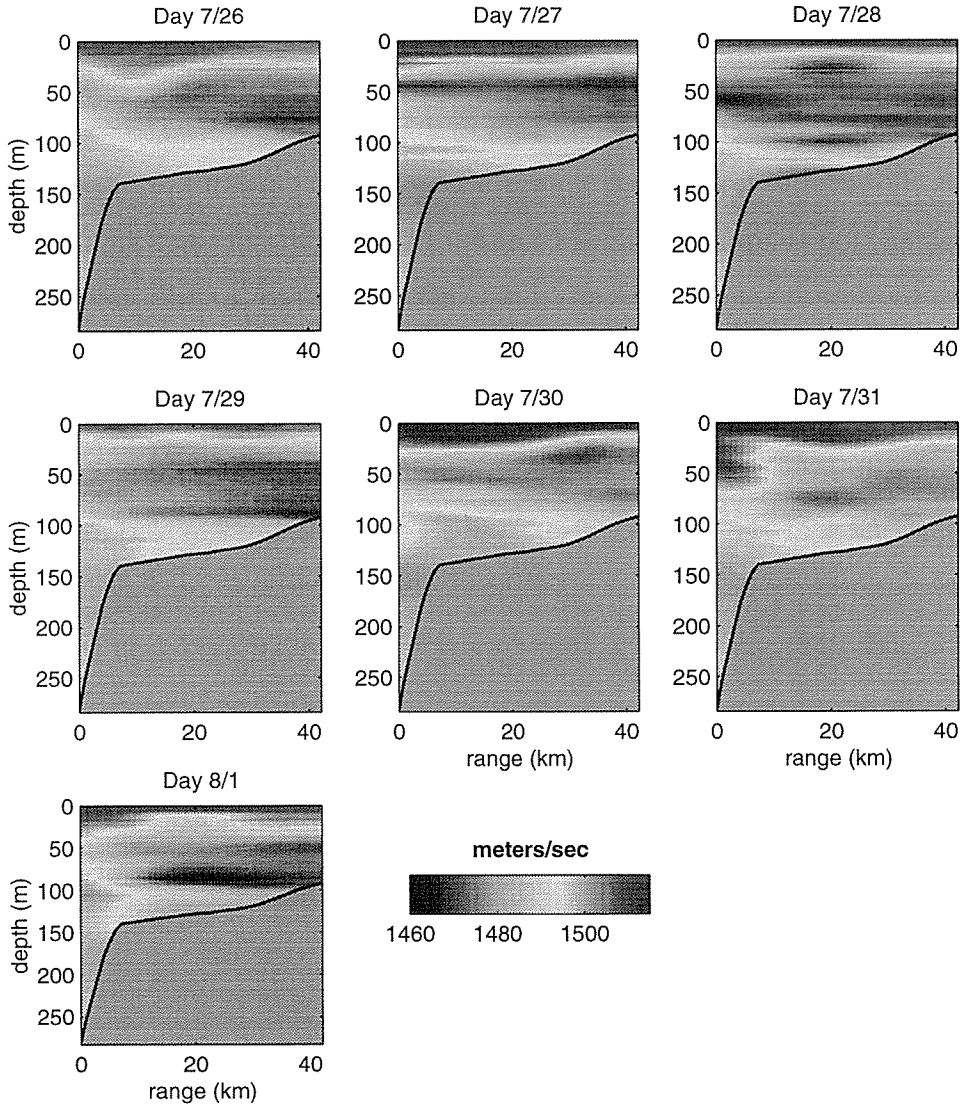

Figure 4-9: Sound speed sections from SeaSoar along eastern propagation path.

Mode Coupling

Figure 4-10 shows the mode energies versus range for the seven sound speed sections shown earlier. For Days 7/27 – 7/29, when the range-dependence is at its weakest, the maximum mode energies are clustered around modes 5–8. For the other days, the energy is spread more evenly over the modes. On Day 7/31, the strong low-mode energy seen at 6 km from the source is a result of the higher modes encountering the large downwelling feature that can be seen in the SeaSoar data on the seaward edge of the front. The rate of occurrence of such acoustically-significant events is difficult to predict given that the formation mechanisms are not well understood. In only one of the three days of SeaSoar data that actually captured the front was such downwelling seen. Figure 4-11 summarizes the initial and final energy distributions. There is a large degree of variability in the initial distribution of mode energies at the source as a result of the modeshapes changing with variations in the local soundspeed profile. Mode amplitudes at the receiver also show a certain amount of variability over the seven-day period, in particular, the enhanced low-mode energy on Day 7/31 is readily discernible. The distribution of mode energies is really a combination of two factors: initial excitation at the source, and the mode coupling at the front. The rest of the mesoscale variability captured in the SeaSoar data does not contribute much in the way of coupling. It does, however, play a role in determining travel times, which is the next issue considered.

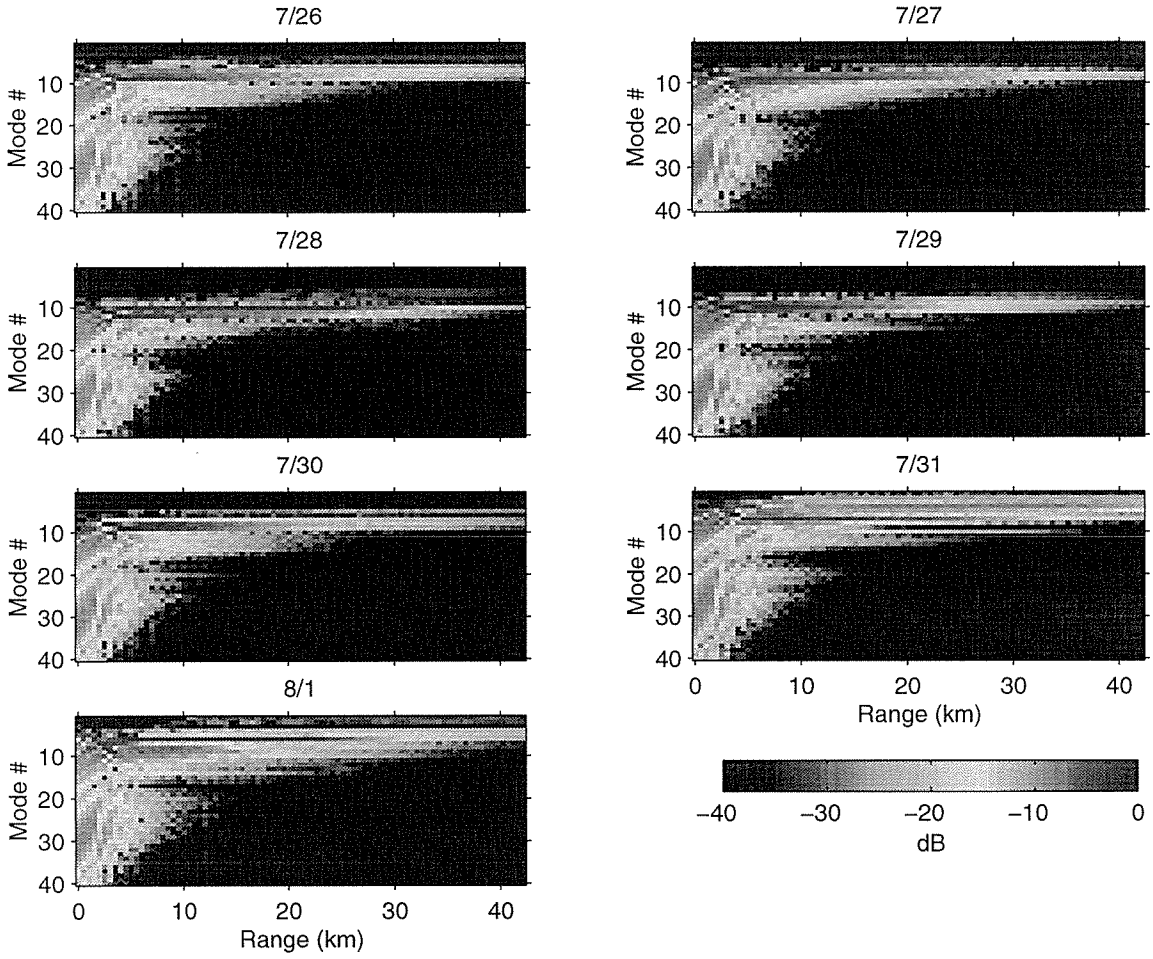

Figure 4-10: Modal energy distributions versus range along eastern propagation path. Source depth 273 m, frequency 400 Hz.

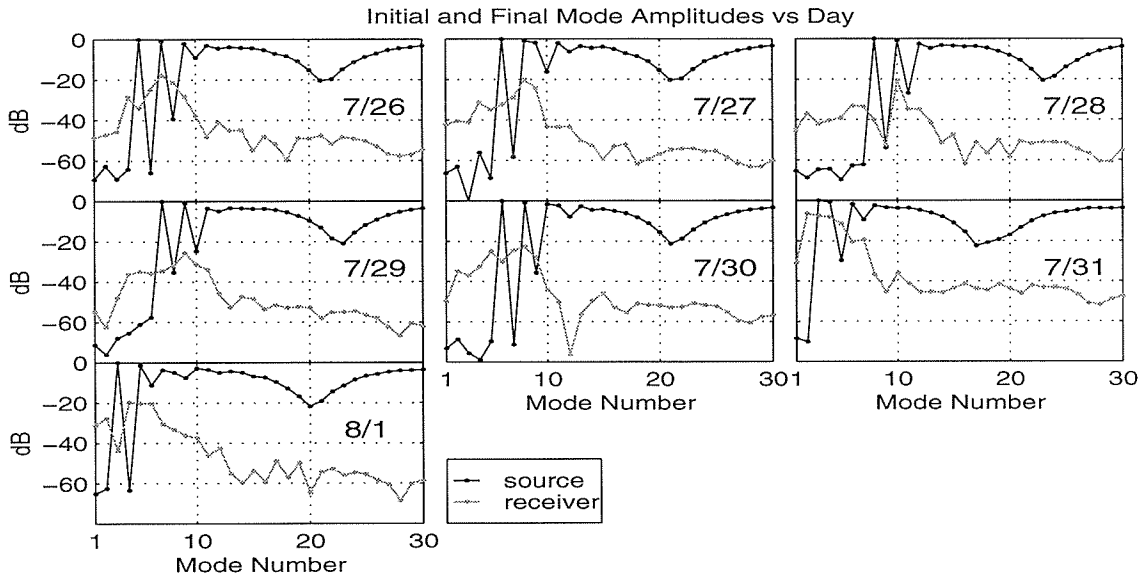

Figure 4-11: Comparison of initial and final mode energies for each of the seven days of SeaSoar coverage.

Travel Time Effects

Measured travel time fluctuations for a given mode can result from two different effects. One, changes in modal group speed, results from changes in the sound speed field (i.e., temperature) along the propagation path. This is considered an adiabatic travel time change. Changes in mode coupling can also create perceived changes in travel time, and unless these effects can be identified as coming from mode coupling, they may be incorrectly perceived as adiabatic fluctuations.

Considering first the potential magnitude of adiabatic travel time fluctuations, Figure 4-12 shows the results of propagating through the seven daily SeaSoar sections, assuming both adiabatic propagation and uniform mode excitation. There is a surprising amount of variability in mode arrival patterns over the daily sections. The fastest arriving mode ranges between numbers 4–8, and varies by more than 200 milliseconds over the 7 days. The spread in mode arrivals also varies substantially, from 50–200 milliseconds. It is apparent that information on the mesoscale structure is being conveyed in the differing mode arrival patterns. This structure, however, will be modified by the effects of mode coupling, and by the fact that the lower mode numbers are not directly excited at the source. All of these effect are considered next,

by making broadband calculations with the PE code, followed by the usual modal decomposition.

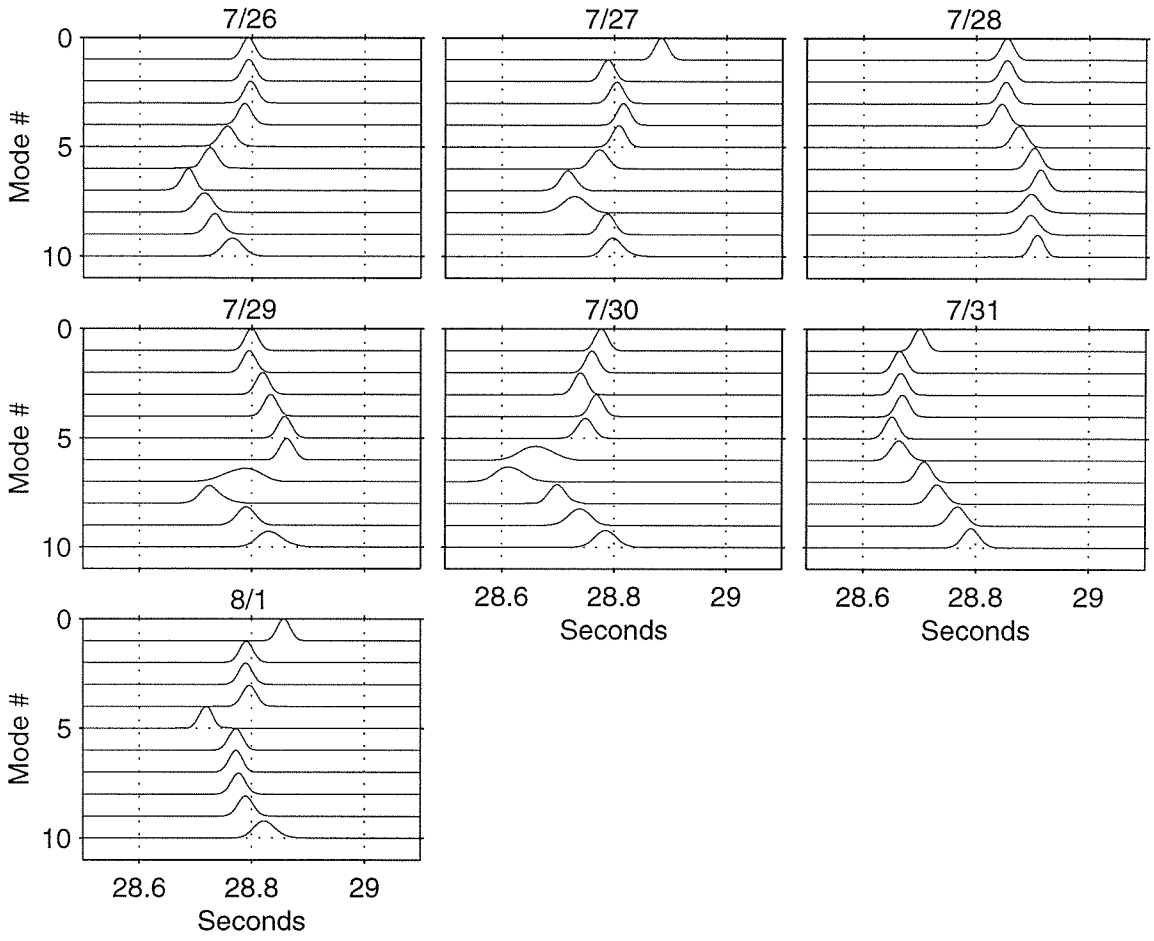

Figure 4-12: Mode arrivals from adiabatic propagation through mesoscale variability along the eastern path. All modes uniformly excited.

Figure 4-13 shows the resulting mode arrivals for the same SeaSoar sections as earlier. There is significant variability over the seven days. Similar to the adiabatic case, the arrivals wander by up to 200 milliseconds. With mode coupling present, however, the relative arrival structure of the modes is additionally changed. Days 7/30–8/1 show more energy in the lower modes than earlier days. This can be traced to coupling at the front, which is pushed forward of the SE400 source during this time period.

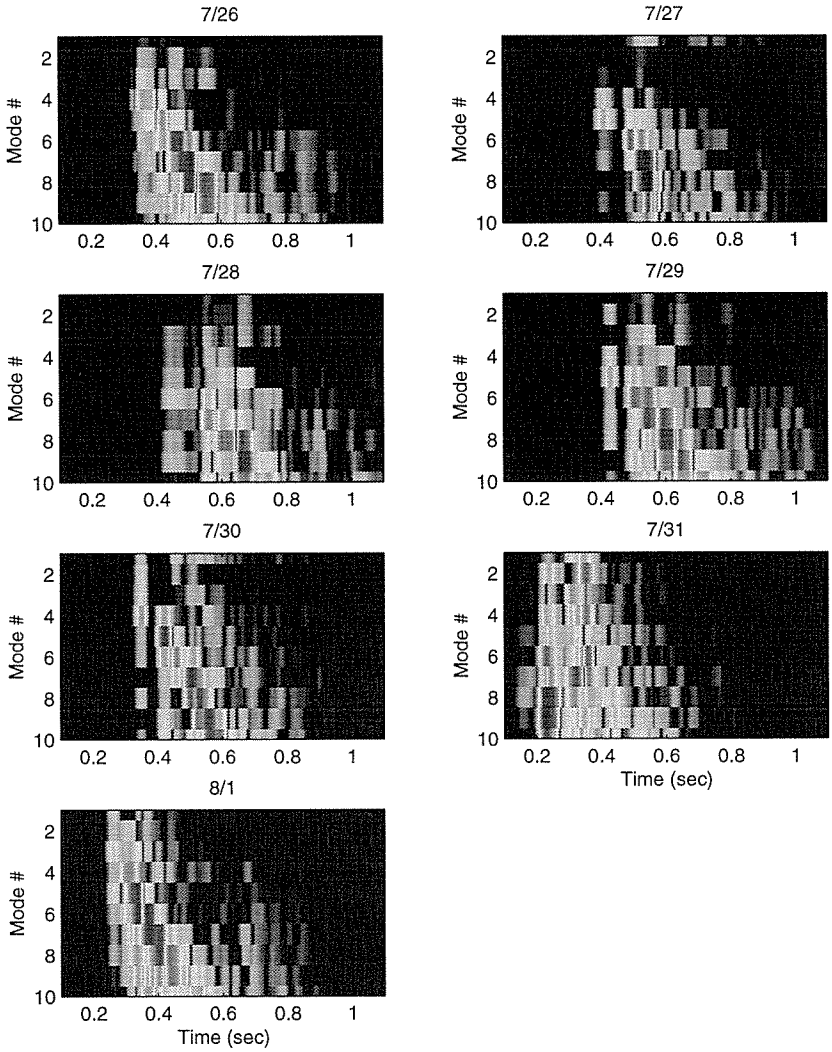

Figure 4-13: Synthetic mode arrivals based on SeaSoar sections along the eastern edge.

4.3.3 Internal Wave Effects

While the effects of the deep water internal wave field on acoustic propagation have been studied for well over two decades, the interactions between shallow water internal waves and acoustics have drawn interest only within the last ten years or so. Zhou et al. (1991) first reported anomalous transmission losses they had observed in the Yellow Sea. Their explanation of the increased losses involved the transfer via solitons of energy from low, trapped acoustic modes to higher, more bottom interacting (and thus more attenuated) modes. Using a very simplified three-layer model of a soliton packet, they demonstrated how this coupling between the acoustic modes could exhibit a resonant behavior that depended upon acoustic frequency, soliton wavelength and soliton packet length. A number of experiments showing soliton/acoustic interactions have since been reported (e.g., Headrick et al., 1997a; Rubenstein, 1998). In addition to increased experimental studies, there is a growing amount of theoretical work being done on the interaction of acoustics and solitons.

Preisig and Duda (1997) showed that the primary factor determining the net mode coupling in a symmetric solitary wave is the relative phasing of the modes after propagating through the wave trough. In a later paper, the same authors consider the effects of a moving packet of irregularly-spaced solitons on the field intensity. Rubenstein (1998) has looked at propagation through internal cnoidal waves, a very regular type of soliton packet. Resonant coupling occurs when the modal interference length along the acoustic path is an integer multiple of the projected wavelength between crests of the cnoidal wave series. Because of 2-D "Bragg crystal" resonances, strong anisotropy is seen in the acoustic propagation whenever mode interference wavelengths match the path-projected soliton wavelengths.

The situation presented in the Shelfbreak PRIMER Experiment is more complex than any of the above, however. Because the study site encompassed the internal tide generation region (at least some of the time) and included large bathymetric changes, the internal wave field underwent a distinct evolution over the 50-kilometer cross-shelf extent of the PRIMER area. In order to obtain a feeling for the effect of

oceanographic variability on acoustic propagation, this section looks at the results of a series of acoustic propagation runs made through a synthetic internal tide model based on the Korteweg-de Vries (KdV) equation (Colosi, 1998; Apel et al., 1995), and initialized using actual data.

Simulated Propagation Through the Internal Tide

The model used here for the evolution of the internal tide solibore was based on a modified version of the KdV equation. The model was initialized with a realistic solibore depression taken from thermistor data, and then allowed to propagate for a 24-hour period. Range-independent bathymetry and buoyancy profile were assumed. While not entirely representative of the actual environment, it does provide a sufficiently-realistic soliton/solibore environment for the purposes of this study. It should be pointed out that this particular KdV model does not include current shear and rotation effects, which can play important roles in determining the internal tide (Colosi, personal communications). Figure 4-14 shows the resulting evolution of a single tidal bore over a 24-hour period. Tracking the leading edge of the internal tide disturbance yields a propagation velocity of around 0.7 m/s up the slope. In actuality, the cycle repeats itself every 12 hours, resulting in there being, at times, two internal tidal bores within the region between acoustic source and receiver. That situation will be considered, but only after understanding the effects of a single solibore on acoustic propagation. Since the exact generation region of internal tide is difficult to place, the initial bore depression used in this study has been shifted so that its leading edge is initially in line with the source location.

The model output shown in Figure 4-14 is actually the amplitude of the first internal wave mode, which field data show is the dominant internal wave mode in the shelfbreak region. Using a representative depth profile for this first mode, the model output may be converted into sound speed perturbations over depth, range and time. Figure 4-15 shows two examples of the resulting sound speed field at times $T = 2$ and $T = 12$ hours. The perturbations have been superimposed upon the reference sound speed environment presented earlier in this chapter.

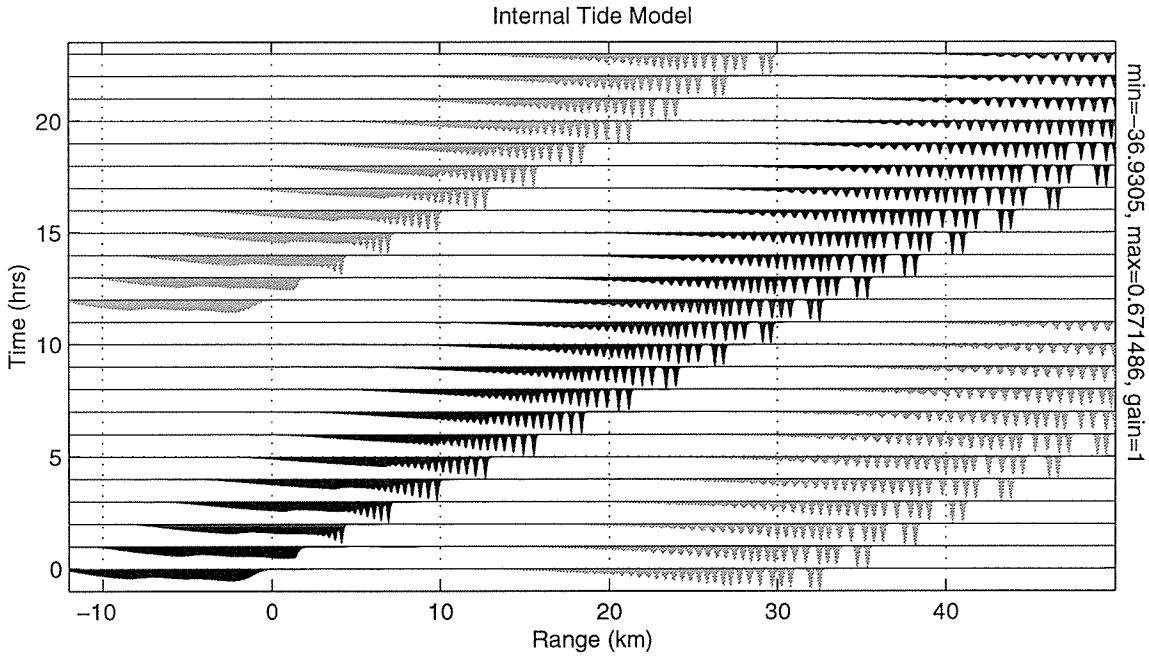

Figure 4-14: Model of internal tide evolution based on KdV equations. Spacing between horizontal lines is 40 meters. Source and VLA are located at 0 and 42 kilometers, respectively. Lighter curves indicate the second solibore needed to model the semidiurnal internal tide.

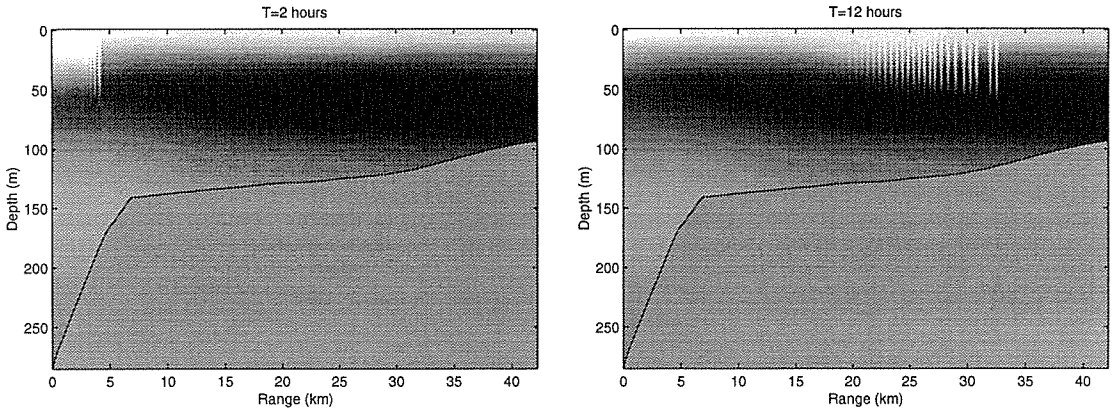

(a) T=2 (b) T=12 hours

Figure 4-15: Examples of sound speed profiles under perturbation by the solibore field.

Parabolic equation calculations were made through the modeled environment at half-hour intervals. To capture the rapid spatial variability of the solitons, very fine step sizes ($\Delta r = 1\text{m}$) were used with the PE code. The generated pressure field was then projected onto the local modeshapes at a variety of ranges, as well as over the entire 100 Hz frequency band for selected ranges.

Mode Coupling

Figure 4-16 presents a series of images showing how the mode amplitudes, as functions of mode number and range, are modified by the presence of an evolving solibore. It takes roughly 15 hours for the leading edge of the solibore to reach the receiver, and a portion of the solibore tail still remains within the acoustic propagation path even after 20 hours. The obvious feature to note is that upon exiting the solibore disturbance, the acoustic field has been scattered into a much broader range of mode numbers than was contained initially. Looking at the case after 6 hours, for example, modes 7 and 9 are initially the strongest. Beginning at the 10 km mark, energy is coupled into successively-adjacent modes as the acoustic field transits the solibore. Modes 1 and 2 do not receive energy until the final coupling at the shock-like leading edge of the bore. It is interesting to note that the coupling serves as a mechanism for energy loss as well as gain. Energy coupled upward in mode number suffers accelerated attenuation because of the greater bottom interaction of the higher modes. The opposite occurs for energy coupled into the lower modes, which are shielded from the bottom. This effect is especially evident in the panel for T =2 hours, where the lower modes become populated only a short distance from the source and are able to proceed to the receiver without attenuation. For the received field to have maximum energy, it is therefore important that the coupling take place early in the propagation (i.e., over the slope, rather than the shelf). Although the KdV model used to generate the solibore time series over-estimates the number of solitons, and does not fully account for dissipation effects, the net result should qualitatively remain then same even with fewer solitons. It is also important to note that the spacing of the solitons is not uniform within the bore, which indicates that Bragg resonance is probably not an

important scattering mechanism.

The previous simulations illustrate the combined effects of many modes simultaneously incident upon an energetic solibore. To consider just the coupling from an individual mode, the PE model was initialized with a single mode rather than a point source, and the resulting mode coefficients extracted from the PE field. Figure 4-17 shows the magnitude of the pressure field for modes 1 and 10. Only an isolated section of the propagation path is considered here. Figure 4-18 shows the effective mode coupling matrix for the first fifteen modes, that results from the configuration illustrated in Figure 4-17, both with and without the solibore present. Without the solibore, the matrix is strongly diagonal; the off-diagonal elements owing to slightly-varying bathymetry. With the solibore present, however, there is no diagonal element to the coupling matrix, indicating that incident energy is being partitioned into all of the modes. The absence of strong off-diagonal peaks indicates there is no resonant coupling taking place. For resonant coupling to occur, there needs to be a confluence of several factors: acoustic frequency, acoustic modal wavenumbers, soliton wavelength and soliton packet length. The latter three all vary with range and time in the PRIMER experiment, making it difficult for any strong resonant effects to occur.

There are two points to be made with these simulations. One is that the energy received in mode n at the VLA may have taken a variety of paths through mode-space, depending on the configuration of the soliton field at that particular moment. This has important ramifications for the inverse problem, which typically relies on the uniqueness of mode travel paths. The second point, which will become more important in the following chapter, is that there is now a clear mechanism for getting energy from a bottom-mounted source into the lower modes that are trapped in the cold water duct.

Mapping the flow of energy through range and mode space only tells part of the story as far as the entire impact of the internal wave field is concerned, however. Coupling can also significantly alter mode arrival times and spreads. In the next section, the propagation of a pulse through the internal tide is considered.

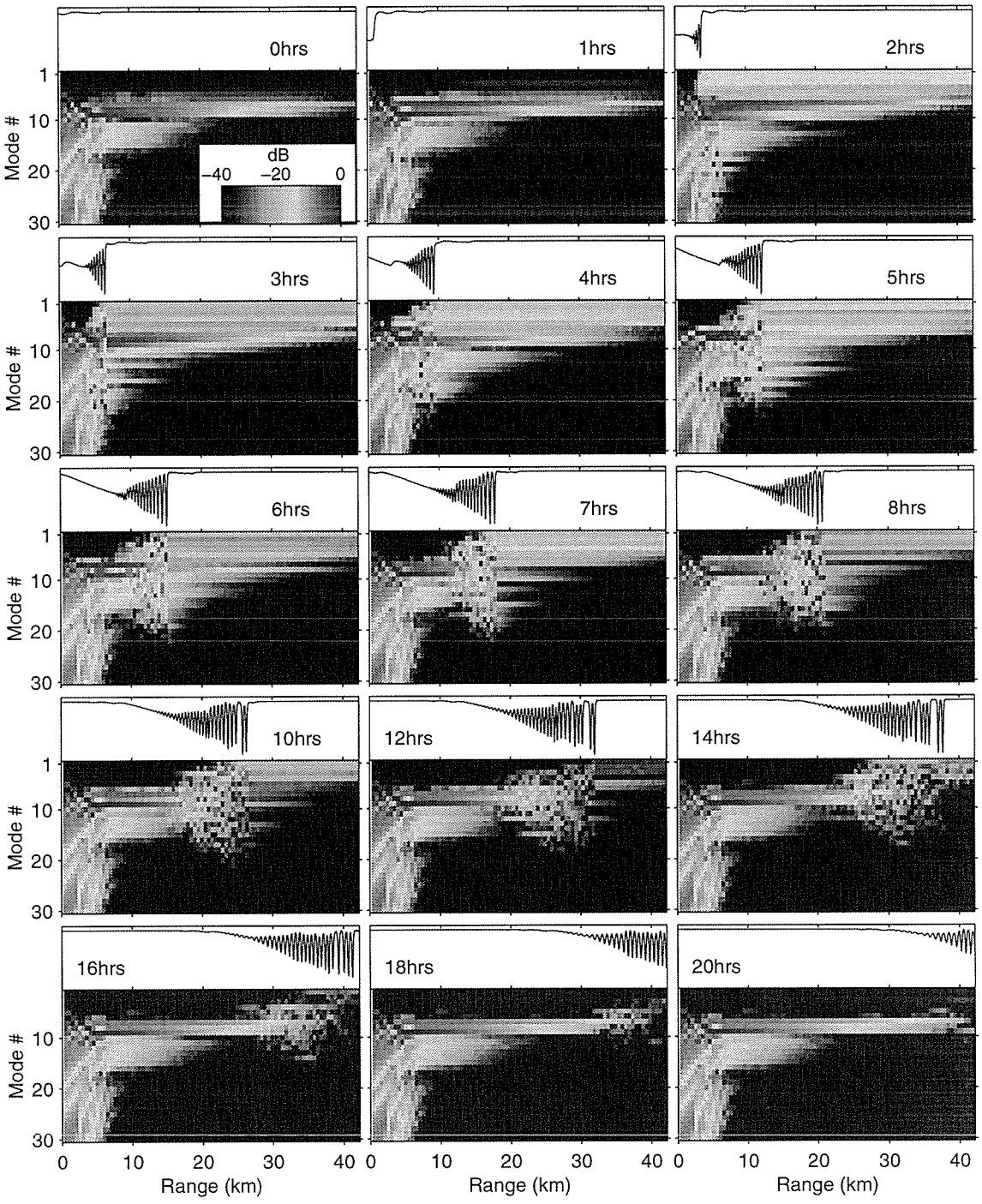

Figure 4-16: Mode coupling due to a single internal tide solibore over a 20-hour period. Upper panels track the position of the solibore, while lower panels display mode amplitudes as a function of mode number and range.

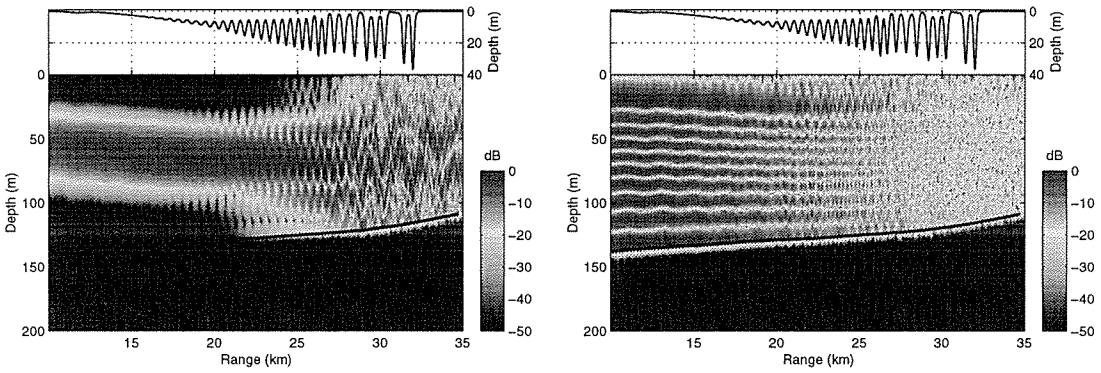

(a) Mode 1

(b) Mode 10

Figure 4-17: A closer look at propagation of individual modes through a well-developed soliton cluster.

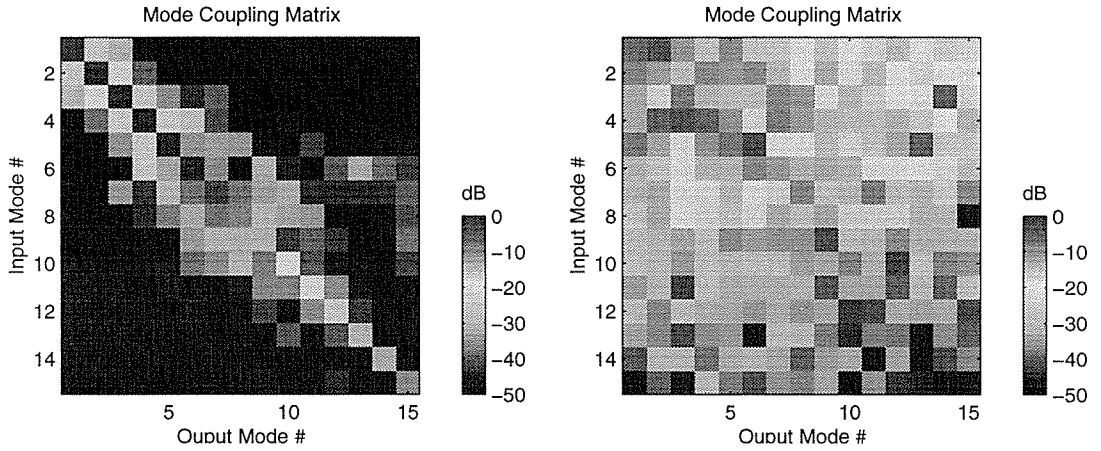

(a) Solibore absent.

(b) Solibore present.

Figure 4-18: Effective mode coupling matrices for the environment indicated in Figure 4-17.

For each time step of the solibore internal tide model shown in Figure 4-14, a series of broadband PE runs were made to synthesize an arrival time series for each arrival. The leading edge, centroid, peak and spread were then measured for each mode. Figure 4-19 illustrates how the arrival leading edges for the first ten modes varied over the 24-hour simulation period (the centroids showed similar patterns). Each arrival is color-coded according to its peak amplitude, and the arrival times are plotted relative to the adiabatic mode 1 time-of-arrival. It is apparent that there are three groups of modes: the first five modes, which all have a broad minimum in travel time around the 12-hour mark; modes 6 and 7, which remain relatively constant; and modes 8–10, which, on average, show decreasing travel times. The illustrated behavior is readily explained by combining the variation with range of the modal group velocities with the fact that only the higher modes are excited by the source. These modes are bottom

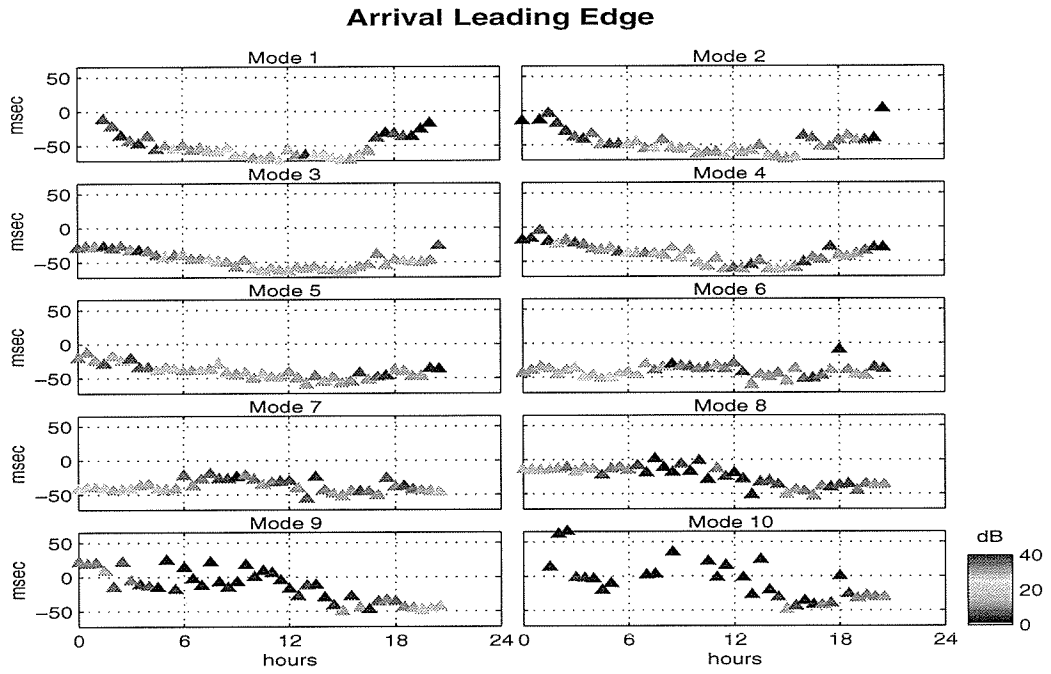

Figure 4-19: Arrival leading edges for each mode. Arrivals are color-coded according to received amplitude. Y-axis is relative to mode 1 adiabatic arrival.

interacting, and are therefore substantially attenuated by the time they reach the receiver. With mode coupling, however, it is possible for energy to propagate faster,

and with less attenuation, in lower modes, then couple into a high mode nearer to the receiver. Mode 6 represents the lowest mode that is energized in the absence of the soliton field. Regardless of mode coupling, there will always be some energy propagating in mode 6, and so, on average, travel time fluctuations for mode 6 will be small. Modes 1–5 do not receive any energy under quiescent conditions. This suggests that the travel times of these modes will be a strong function of where on the propagation path they are excited.

To understand the parabola-like travel time perturbation curves of the low modes, it is helpful to recall how the modal group velocities vary as a function of range. (See Figure 4-7 on page 76.) In Figure 4-20, a simple propagation model is devised whereby energy starts in mode M and couples into mode 1 at varying ranges. The y-axis in Figure 4-20(a) gives measured travel time of mode 1 at the receiver. The x-axis indicates the coupling range. The path which yields the shortest travel time for mode 1 initially starts in mode 6, the fastest mode over the first 30 km, and doesn't transfer to mode 1 until the 30 kilometer mark.

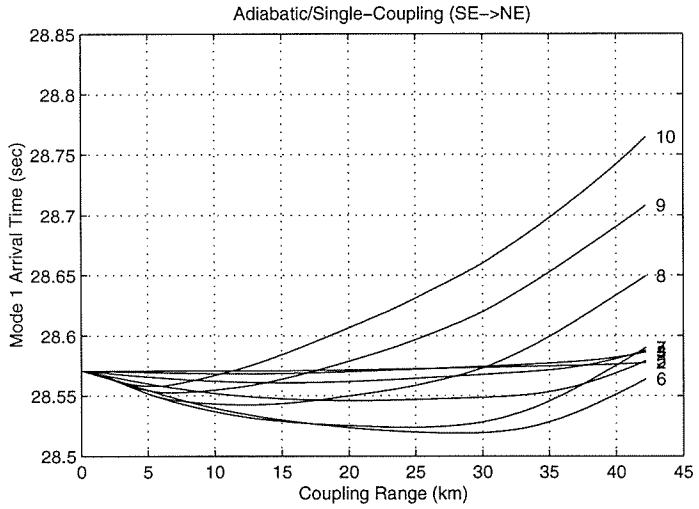

(a) Mode 1 travel time variations.

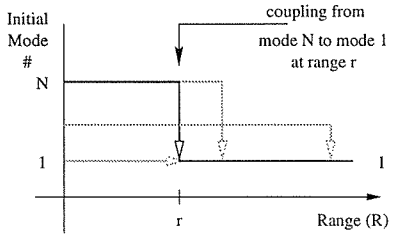

(b) Coupling schematic.

Figure 4-20: Effect on mode 1 travel time due to coupling from various modes at various distances along the source to receiver path.

Another parameter of interest is the arrival spread, in this case measured by

the inter-quartile range, or IQR, defined as the difference between the 75^{th} and 25^{th} percentiles of the signal falling above a given noise threshold. Figure 4-21 shows the arrival spreads corresponding to the same arrivals shown in Figure 4-19. One of the more noticeable features is the peak in signal spread near the 12-hour point for modes 1 and 2. This corresponds to multiple modes all coupling into mode 1 at around the 30 kilometer point. The differences in mode travel times with range leading up to the 30 kilometer mark, give rise to the large spread values seen for modes 1 and 2.

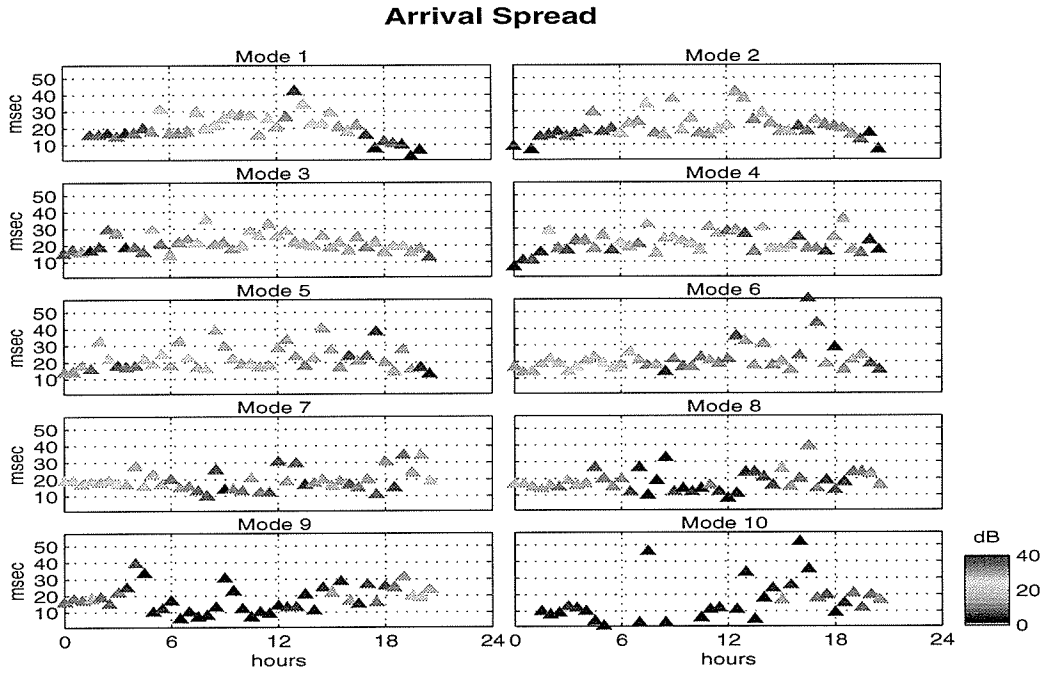

Figure 4-21: Inter-quartile spread of mode arrivals.

Semidiurnal Effects

The previous simulations have only considered the presence of a single solibore. In theory, a solibore should be generated with every change of the semidiurnal tide (i.e., every 12.4 hours). Because the source-to-receiver range exceeds that which can be covered by a soliton or solibore in 12.42 hours, there will always be more than one series of internal tide disturbances along the propagation path. This effectively adds a second "degree of freedom" to the mode coupling problem. Figures 4-22 and 4-23 show how the arrival time and spread are modified with the addition of a second

solibore at the M_2 period.

Looking first at Figure 4-22, there is clear evidence of an M_2-periodicity. For the low modes, the variability is much smaller than that shown previously, whereas the higher modes show much larger fluctuations. The latter may be explained by noting that energy may now be coupled into the lowest modes early on, and then coupled back into the higher modes near the receiver. This also explains the increased levels in energy seen in the higher modes as compared with the simulations with the single solibore.

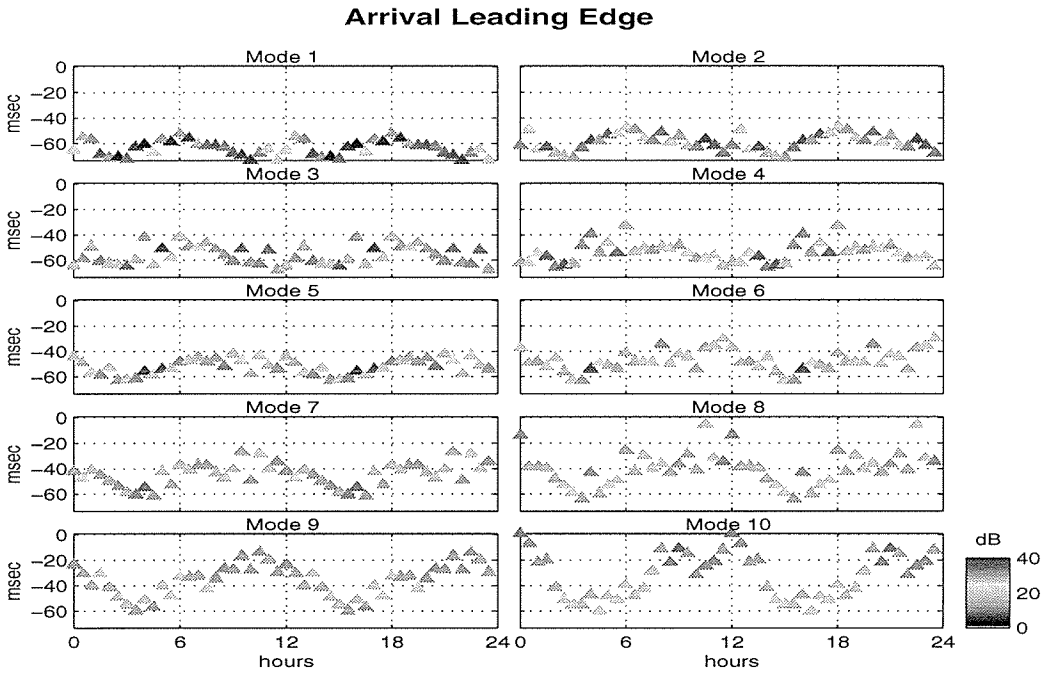

Figure 4-22: Leading edge arrival times for modes 1–10 after propagating through synthetic M_2 internal tide solibore.

It is interesting to note that, because of the coupling, the mode 1 arrival time is now biased roughly 60 milliseconds faster than its adiabatic arrival. In fact, all of the mode leading-edges are biased faster than their adiabatic counterparts as a result of traveling in faster modes for part of the distance, and then still being able to couple into the proper mode at the receiver.

An M_2 signal is also apparent in the measured IQR for some of the modes, shown in Figure 4-23. Adding in the second soliton train increases the spread by around

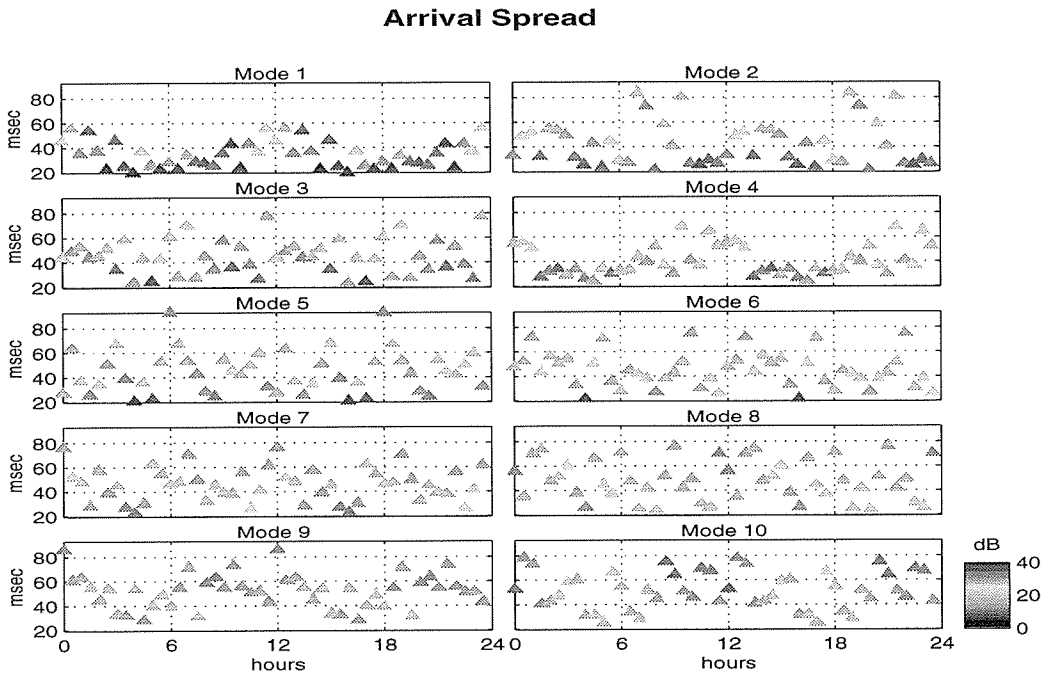

Figure 4-23: Arrival spread for modes 1–10 for simulated propagation through an M_2 internal tide.

20–40 milliseconds depending on the mode number. It is interesting to note that there are large fluctuations in the spread between successive 1/2-hour time increments that appear to be superimposed upon lower-frequency (M_2 or lower) variations.

4.4 Summary

In this chapter we have looked at how the oceanography and sea floor influence the propagation of acoustic energy through the shelfbreak region. Two findings are particularly important. The first is the relative contributions to the overall mode coupling by the bathymetry, the shelfbreak front and the soliton field. Of these three, it is the soliton field that is likely responsible for the majority of the mode coupling. The location of the SBPX makes it possible for highly-energetic solibores to travel through the study area, creating large mode coupling disturbances. Depending on the location of the front, however, it may at times be the dominant coupling mechanism. The bathymetry is also responsible for a certain amount of energy transfer between modes, but only the front and solitons were shown to be able to transfer energy into

the lowest modes.

The second important finding of the chapter is the impact of having range-dependent group velocities in the presence of mode coupling. One outcome of this is that the fastest arrival along the eastern acoustic propagation path would be one that traveled in mode 6 for the first 30 kilometers, then coupled into mode 1 and traveled the rest of the way to the receiver. The fastest path along the diagonal actually involves four different mode numbers.

Chapter 5

Data Analysis and Inversion

5.1 Overview

At the end of Chapter 3, an overview of the acoustic data and its complicated nature was given. Chapter 4 explored, with the aid of propagation modeling based on the measured environmental data, the interaction of sound with the ocean environment as it travels through the region of the continental shelfbreak. This chapter returns to the related tasks of acoustic data analysis and inversion, with the benefit now of having an understanding of some of the relevant propagation issues. The first three sections of this chapter are concerned with analyzing the data from the two 400 Hz sources located at the southeast and southwest corners of the experiment. The final section deals with how one might go about inverting the acoustic data for sound speed fluctuations and thus water temperature and oceanography.

5.2 Extraction of Modal Statistics

The waterfall plots in Figure 5-1 show the arrival of mode 1 from the SE 400 Hz (abbreviated as SE400) source using two different time scales. In the Figure 5-1(a), the 11-minute gap between the end of one transmission and the beginning of the next has been eliminated. Each transmission lasts roughly 4 minutes (1 transmission = 48 sequences, averaged 3 at a time). Within an individual transmission series, the

receptions are reasonably correlated, but between series, the correlation is weak. The maximum decorrelation time, therefore, is at most 11 minutes, but is most likely much less than that. In a few instances there are features that are consistent from one 15-minute period to the next. In canonical shallow water, range-independent, propagation, the earliest arrival has an abrupt onset and maximum amplitude, while the signal tail trails off in an uneven fashion. Both the sharp onset and diminishing tail are seen in the receptions, but the earliest arrivals are not always the most energetic. These features are all consistent with propagation in shallow water when mode coupling is significant.

In Figure 5-1(b), mode 1 arrivals are shown for a seven-day period at one-hour intervals. From this perspective, there is absolutely no coherence between arrivals. The only measures with moderate consistency from one hour to the next are features such as the leading edge and general spread of the signal. In less complicated environments it is sometimes possible to associate the larger "bumps" within each arrival with particular features of the propagation, but not in this case. Instead, the next sections will focus on a few statistical characterizations of the acoustic receptions that have proven effective in previous work, in particular, measures of the travel time variability and of the signal spread.

Several different parameters were considered as measures of the signal wander, including the leading edge of the arrival, the arrival centroid and the peak arrival time. The leading edge of the arrival was defined to be the first time the arrival transitioned through a threshold set to 15 dB above the noise floor. The noise floor was determined for each transmission by calculating the background noise level based on a short section of data prior to any arrival. Arrivals contaminated by shipping noise were eliminated from consideration (see Appendix B for a list of shipping interferences). The peak arrival time was defined simply as the time of arrival of the point of maximum amplitude in the time series. The centroid was calculated by finding the center of mass for that portion of the sequence that was above threshold, as illustrated in Figure 5-2.

There are a number of ways one can define the spread of an arrival, such as

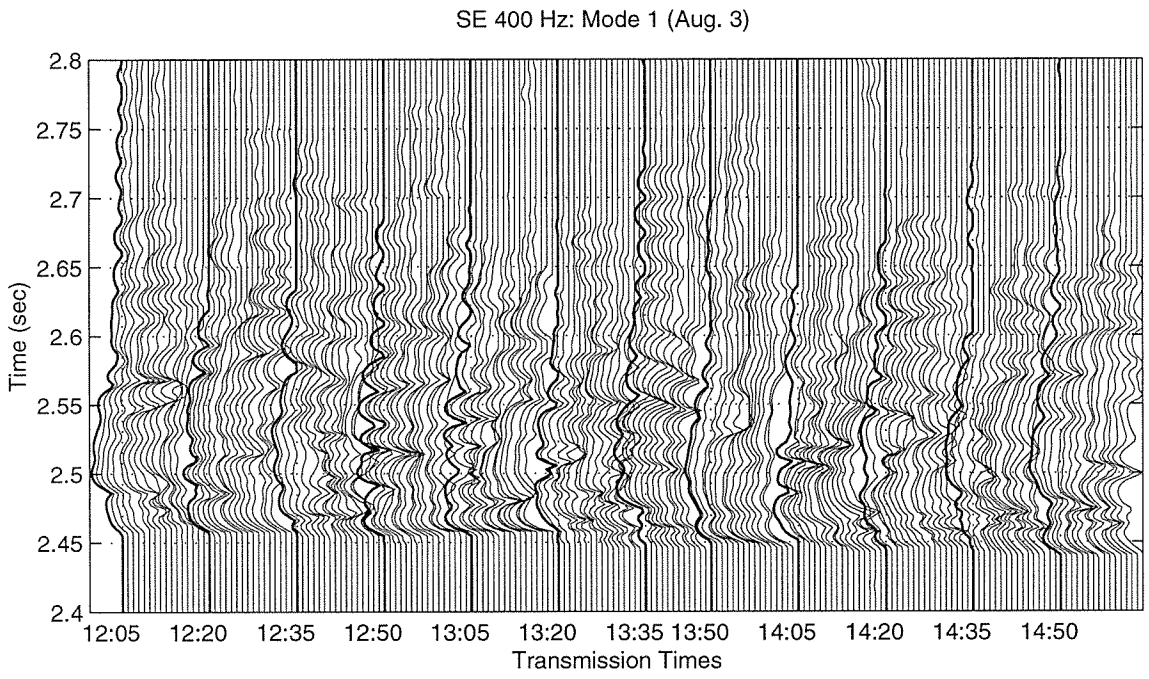

(a) Mode 1 receptions from SE 400 Hz source on August 3. Transmissions are every 15 minutes, last for 4.1 minutes, and the 11-minute gap between transmissions has been omitted. The start of each transmission is indicated by thicker lines.

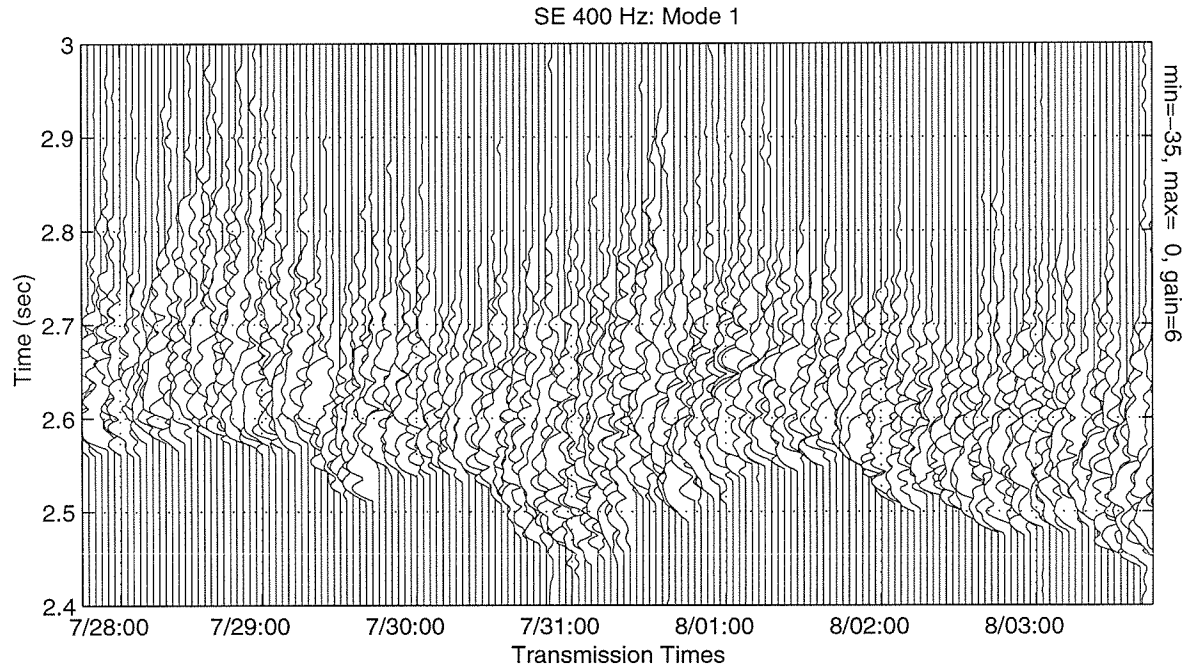

(b) Mode 1 arrivals over a seven day period. Each line is an average over the first three sequences at the beginning of each hour.

Figure 5-1: Mode 1 receptions from the SE 400 Hz source.

variance, time above threshold, inter-quartile range, mean absolute deviation, etc. Because of its success in similar situations (Headrick, 1997), and because a survey of other measures failed to uncover a better statistic, the inter-quartile range, or IQR, is used as a measure of signal spread. The IQR is defined as the difference between the 75^{th} and 25^{th} percentiles, and is a robust estimator of the spread. To calculate the IQR, the portion of the signal above threshold is extracted and rescaled to have amplitudes between 0 and 100. A vector of bin numbers is constructed, with each bin number being weighted according to its amplitude scaling. The IQR of the vector of bin numbers is calculated. Figure 5-2 illustrates the calculation.

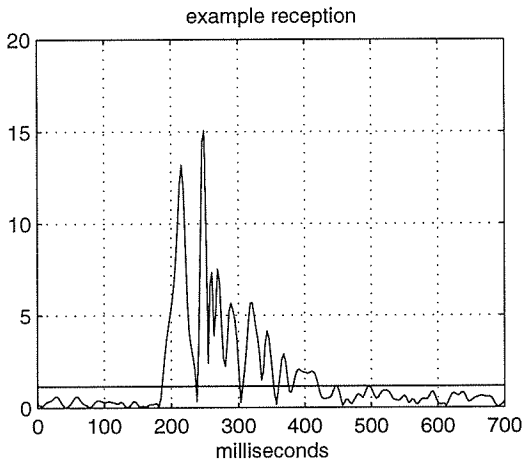

(a) An example mode reception (SE400 mode 4, 08030105).

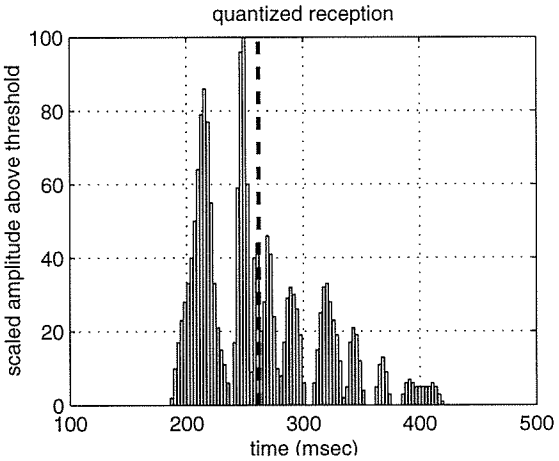

(b) Quantized version of reception above threshold. Dashed line indicates centroid.

Figure 5-2: Procedure for calculating mode statistics.

The leading edge and other statistics are computed for each of the 48 sequences and then averaged together, creating a time series of mode statistics with a 15-minute sample period. (Recall that the 400 Hz sources each transmitted a string of 48 m-sequences, lasting a total of 4.1 minutes, every 15 minutes.) Generally, these time series are given a 4-hour running average to remove the high frequency fluctuations (which are themselves of interest and are analyzed later on). Another measure of interest is the variance of the various statistical measures available. In particular, the variance across the 48 m-sequences that were used to create each 15-minute sample

point. These will also be discussed later. In sections that follow, we look at the wander and spread of the source receptions. Where appropriate, comparisons are made between the acoustic data and the oceanography, and also between measured acoustics and the theoretical propagation modeling results.

5.3 Analysis of SE 400 Hz Arrivals

Figure 5-3 shows the leading edge and centroid arrivals for the first ten modes (recall that the VLA can only resolve the first ten modes, and even then there is non-negligible energy leakage from higher adjacent modes). The leading edge of an arrival is sensitive only to changes that affect the quickest path to that mode number, at the receiver, through mode and range space (provided there is sufficient energy in that path to be detected). The arrival centroid, however, is a function not only of the fastest path, but also the slowest path, all paths in between, and also how the energy is distributed over the arrival. Large amounts of coupling along the propagation path will keep the leading edges relatively close together. This is apparent in Figure 5-3. Using the color-key to group the mode centroids, one notes that modes 1–5 tend to stay within 10 milliseconds of one another, while the centroids for modes 6–10 are spread out over approximately 50 milliseconds. One likely reason for this relates to the fact that the first five modes are not usually excited by the bottom-mounted source. The coupling histories of the first five modes are likely to be quite similar. That is, each of the first five modes is likely to receive energy at similar locations and times. Thus the spread in arrivals is due only to the small differences in group velocities, scaled by the propagation distance from coupling point to receiver. Pursuing the notion of propagation velocities a little further, one can plot the mode arrival times relative to mode 1, which tends to be the fastest-arriving mode as long as energy is being coupled into the mode in the latter half of the propagation path. Figure 5-4 shows the leading edges relative to the mode 1 arrival. Two periods are of immediate interest. The first, the times during yearday (YD) 208 (7/26/96) and YD 212–213 (7/30,31), when many of the other modes beat mode 1 to the receiver. In fact, toward

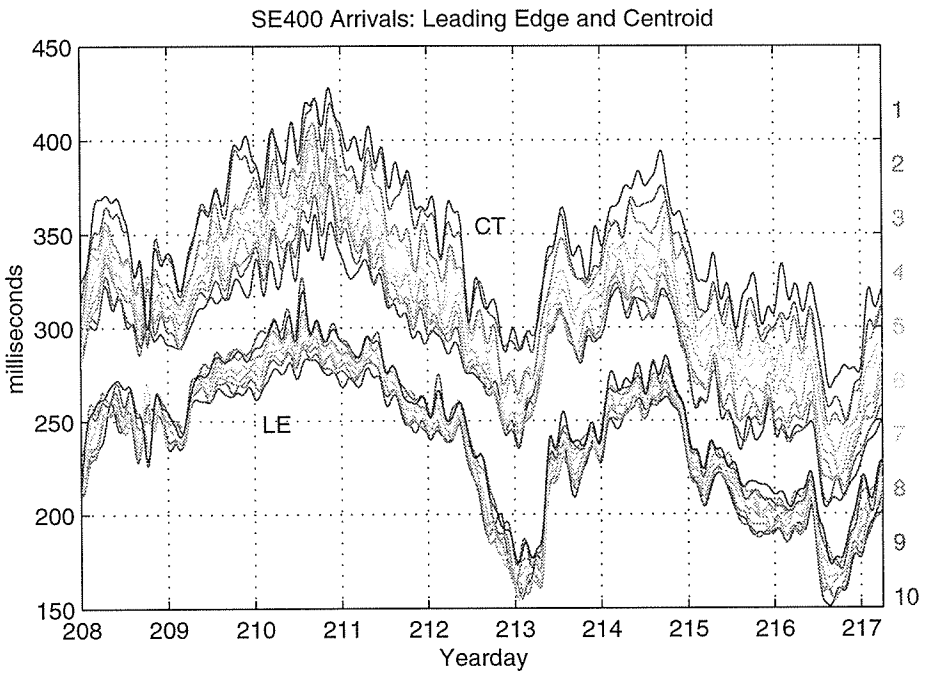

Figure 5-3: Leading edge and centroid arrivals for first ten modes from SE400 source. Larger numbers indicate later arrival times, or slower propagation speeds.

the end of YD 212, mode 1 is the last of the ten to arrive. In this particular instance, it is likely the lower 1–4 modes received little energy input from coupling. This is supported by the thermistor data, which show little soliton activity during this time period. Mode 1 is certainly not always the fastest mode. On some days either mode 2 or 3 may become the fastest over the latter half of the propagation path (recall from Chapter 4 that higher modes are faster in the deeper water). During YD 209–211, the leading edge of the mode 1 arrival tends to separate more from the other modes. This time period corresponds to the intrusion of a large body of cold shelf water into the eastern half of the PRIMER site. This change in oceanography may very likely alter the sound speed profiles in such a manner that mode 1 travels faster than usual relative to the other modes.

There are several features in the mode arrivals that warrant further exploration. In particular, the various factors contributing to the wander seen in the leading edge and centroid data need to be explored, as well as the signal spread, which hasn't been addressed yet.

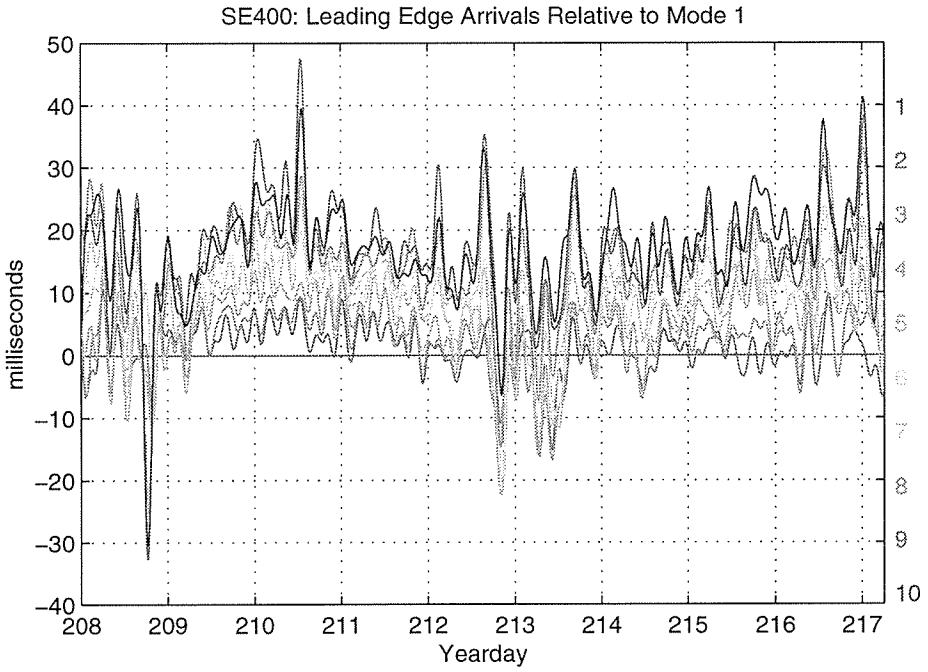

Figure 5-4: Leading edge arrivals for first ten modes from SE400 source relative to the more 1 arrival. Positive numbers indicate arrivals after mode 1.

5.3.1 Signal Wander

Mesoscale Influences

Several correlations may be drawn between the acoustic variability and the large-scale oceanography picture provided by the SeaSoar data. For example, the time between YD 209 and 212 corresponds to the cold shelf water intrusion along the eastern propagation path as the frontal meander passed through the study area. This is reflected by the generally longer travel times of all the acoustic modes. The sharp decrease in travel time centered around the beginning of YD 213 coincides with the advection of the shelfbreak front northward of the SE source. Indeed, the simulations of the last chapter show similar trends for this time period. Over this span of 72 hours, the mode 1 leading edge undergoes a travel time change of over 120 milliseconds. If this were to come entirely from a change in average water temperature along the acoustic travel path, it would require a ΔT of 1.3^{o}C, assuming an average mode 1 group velocity of 1480 m/s. This turns out to be in general agreement with the findings from a simplified inversion for range- and depth-averaged water temperature,

as discussed later in this chapter.

In the absence of SeaSoar data, the only oceanographic measurements available from which to form non-acoustic estimates of the thermohaline environment are thermistor records. Using only the thermistors from the east-side source and receiver moorings, it is straightforward to form an estimate of the expected acoustic travel time perturbations. The implicit assumption in such a back-of-the-envelope calculation is that the fluctuations in the propagation are primarily adiabatic[1]. The ad-hoc prediction proceeds as follows. Based on the general oceanography of the region, one may assume that temperatures measured at the southern mooring are valid roughly over the extent of the shelfbreak slope (from 0–8 km along the propagation path), and that the northern temperatures are representative of shelf waters (from 8–42 km). These relative distances can be used to assign weightings when combining the thermistor data from NE and SE moorings. A second parameter to vary is the choice of thermistors to use from each mooring. After calculating the cross-correlation between acoustic-based travel time perturbation and thermistor-based perturbation estimates, for all combinations of thermistors at the two moorings, it was found that the combination with the best fit to the acoustic data was an average of the SE mooring thermistors at 10 and 25 meters depth, and the near-surface thermistors from the NE mooring. This particular thermistor combination is not surprising, given that the depths of these thermistors are close to the turning points of many of the acoustic modeshapes. At those depths, the modes will be most sensitive to changes in water temperature. Figure 5-5 shows the resulting comparison between the range-weighted combination of thermistor data, converted into equivalent travel time fluctuation, and the actual travel time variation of the mode 1 leading edge. There is reasonable agreement between the two curves, in particular the cooling (travel time increase) centered around YD 211, and the rapid warming (decrease in travel time) early on YD 213. Most of the differences between the two curves likely come from mesoscale

[1]The term "adiabatic" is being used somewhat loosely here. An "adiabatic fluctuation" is one in which a fluctuation in travel time arises from changes in modal group speeds, as opposed to changes in mode coupling. Strictly speaking, adiabatic propagation occurs only in the absence of any mode coupling.

fluctuations in temperature that are not reflected in the thermistor measurements at the two endpoints. Some of the variability, however, may be due to significant changes in the mode coupling. This is particularly feasible during occasions such as Day 7/31 (YD 213) when the front shifted north of the source, accompanied by strong downwelling on the onshore edge of the front. Large deviations between acoustic and

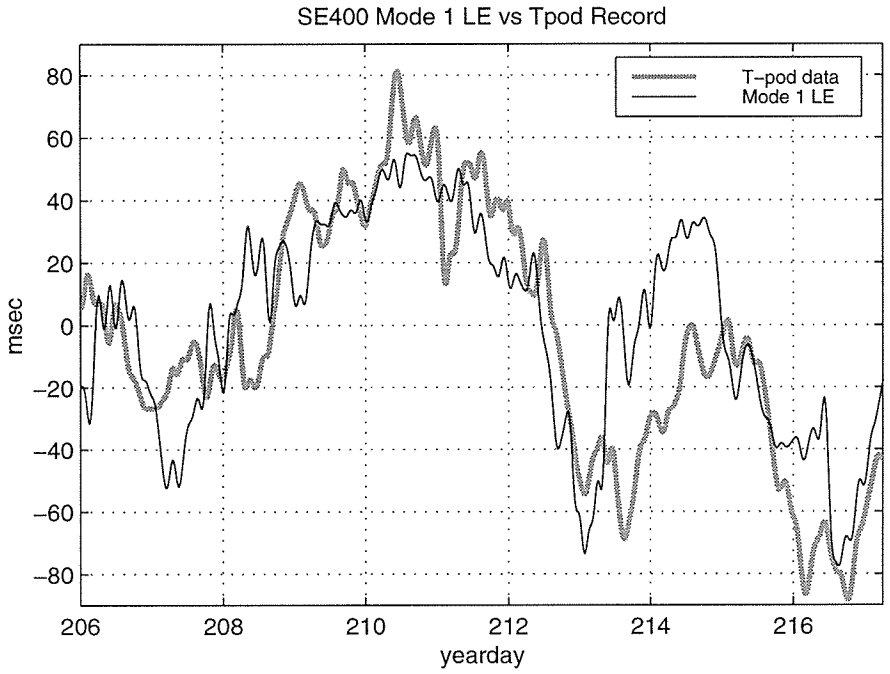

Figure 5-5: Leading edge arrival of mode 1 versus theoretical travel time perturbation based only on thermistor data. Both curves are centered about their mean values.

thermistor-derived curves are seen from YD 213 and 215, as well as around YD 208.5 and YD 207. It is possible that the latter two events correspond to instances where the front is again positioned northward of the source.

It is clear from this exercise that the large-scale variability is being tracked acoustically, and the rapid shifts seen acoustically, such as that around YD 213, are indeed consistent with recorded temperature variations. It is helpful to look at some of the other phenomena likely to have acoustic effects, such as the tides.

Tidal Contributions

A certain amount of travel time variability will result from tidal activity on the continental shelf. While the simulations in Chapter 4 showed how tidally-driven solibores can introduce periodic mode coupling, there are more direct means by which the tides can influence the acoustics. These include tidal currents (barotropic and baroclinic), horizontal advection of water masses, and barotropic change in water depth. Previous figures showing leading edge and centroid arrivals for the eastern propagation path show only slight variability at tidal frequencies. This is supported by the power spectral density of the mode 1 leading edge, shown in Figure 5-6. While there may indeed be contributions at the diurnal and semidiurnal frequencies, they do not stand out significantly from the rest of the spectrum. Nevertheless, we are still interested in estimating the contributions to travel time variability from the various tidal components.

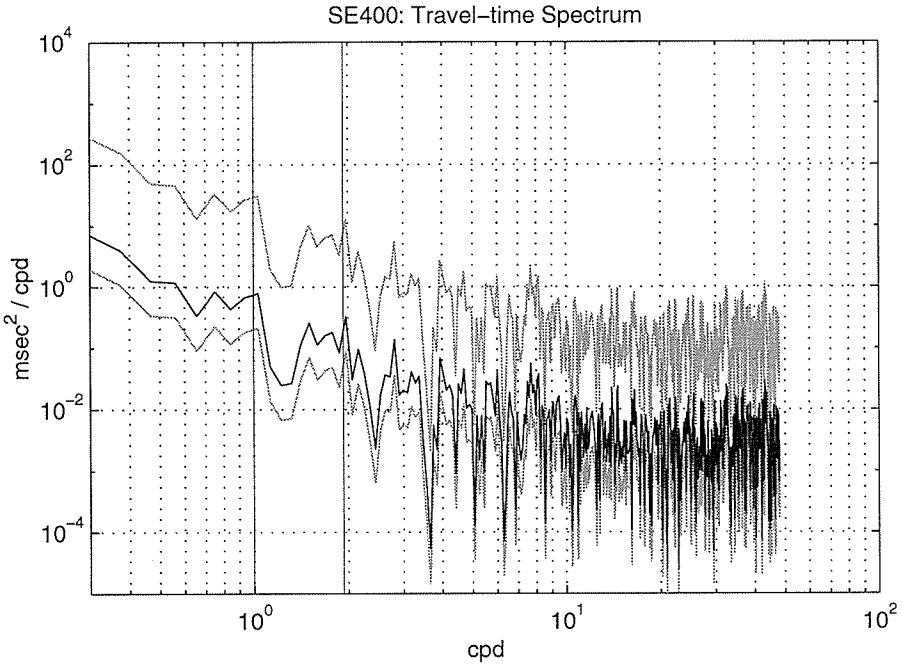

Figure 5-6: Power spectral density for mode 1 leading edge. The PSD is based on an 11-day record from yeardays 206–217. Gray lines indicate 95% confidence interval. Vertical lines indicate diurnal and semidiurnal tidal frequencies.

Ideally, current meter data would be used to estimate the local tidal current field.

As no such measurements were made on the eastern edge of the study area, the predicted current field from the tidal model discussed in Chapter 2 will be used. Figure 5-7 compares the travel time perturbation due to the barotropic tidal current, as predicted by the model, to the narrowband-filtered leading edge arrival, averaged over the first ten modes. Because only a very short time period (from a tide perspective) of acoustic data is available, one should not place too much stock in detailed comparisons between the two curves. Nevertheless, the perturbation amplitudes of ±2–5 msec are in relatively good agreement, particularly during the YD 209.5–212.5 period. As has been noted several times previously, this corresponds to the time when the shelf water meander occupies most of the acoustic path, and the soliton activity at the NE VLA noticeably differed from other periods. It is conceivable that enhanced mode coupling from solibores is responsible for the changes in amplitude and phase either side of the meander time window.

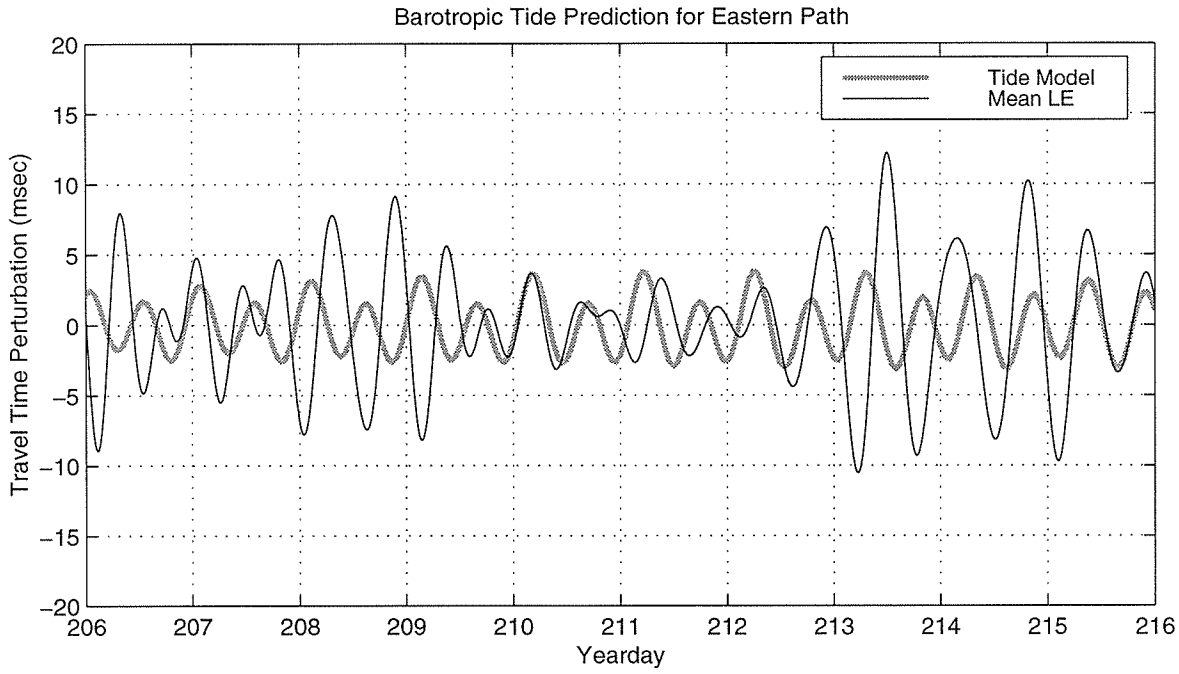

Figure 5-7: Equivalent travel time change from barotropic tidal model compared with the average modal leading edge for the eastern propagation path.

The effects of horizontal advection are more difficult to estimate. The North-South tidal excursion lengths (from integrating the modeled tidal currents) are ±1000 me-

ters. If, at its maximum southern displacement, the northern edge of the front was just seaward of the source, the changing tide could advect the front a full two kilometers northward of the source. Assuming an average change in water temperature of 1 degree, this influx of warmer water could result in a 4 millisecond decrease in travel time.

Water depth changes are available from the same tide model that provided the barotropic current field. The maximum variation appears to be ±80 centimeters. The acoustic impact of such elevation changes was estimated by assuming adiabatic propagation over the 42 km path length. Figure 5-8 shows the computed travel time change for each of the first fifteen modes due to tidal elevation effects. For the lower

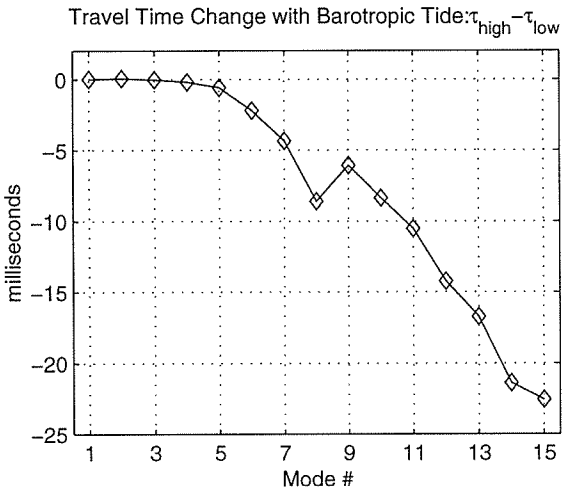

Figure 5-8: Difference in adiabatic modal travel times for a 1-meter increase in water depth over the entire propagation path along the eastern section. Negative indicates faster propagation.

5 modes, there is virtually no change in travel time, owing to their non-interaction with the surface waters. For surface-interacting modes there can be changes of 10 milliseconds or greater. The two simplifications made here, spatial uniformity of the tidal elevation change and adiabatic propagation, suggest that these numbers be treated as extrema; specifically they are an upper-bound on the higher order modes, and a lower-bound on the lower order modes. Since no pressure sensor data is available for the duration of the experiment, it is difficult to draw more specific conclusions.

5.3.2 Signal Spread

Figure 5-9 shows the signal spread as measured by the inter-quartile range (IQR) for mode 1. Higher modes had progressively more spread (not shown), some of which is certainly due to increasing amounts of modal crosstalk from the mode filtering. The magnitude of the mode 1 spread is a little larger than values seen in the Chapter 4 simulated propagation through a tidal series of solibore/soliton fields, where the mean for the mode 1 IQR was 34 msec. The primary reason for the discrepancy is likely the fact that the simulations were done using the reference mesoscale environment rather than any of the actual SeaSoar profiles. The values shown in Figure 5-9 are

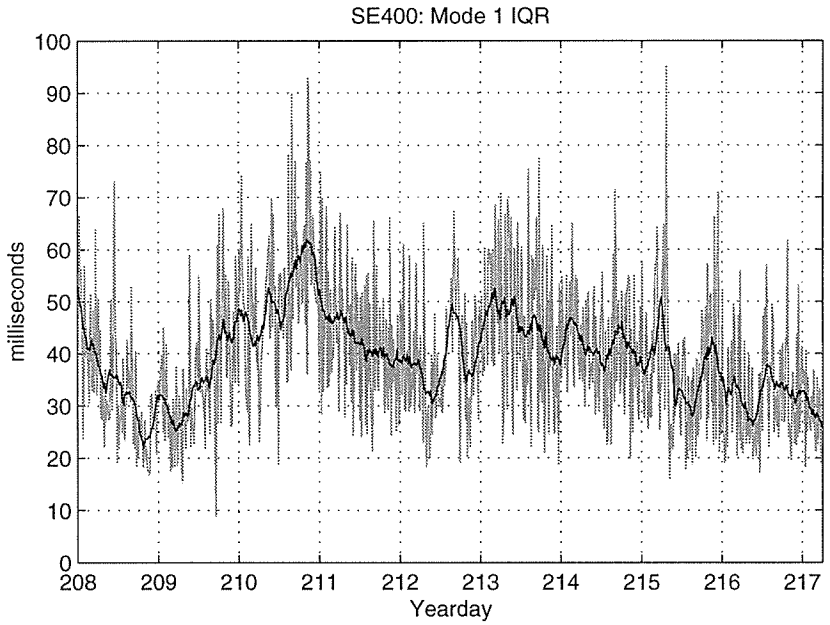

Figure 5-9: Mode 1 IQR for SE400. Gray line is unfiltered IQR, and black line is a 4-hour running average.

very comparable to the spread seen in the SWARM data (Headrick et al., 1997a), only with more daily variability seen in the PRIMER data. The daily variability is not unexpected, given the proximity to the shelfbreak front. The decreases in spread during yeardays 209 and 212 correspond to periods that appear to have less soliton activity, as inferred from back-propagated thermistor data at the NE VLA, which show more quiescence during those time intervals. This observation can be further quantified by highpass filtering the RMS isotherm displacement at the NE VLA, as

shown in Figure 5-10. The decrease in spread centered around YD 212–213 does indeed correspond to a minimum in soliton activity near the NE VLA, however the large decrease in spread of mode 1 around YD 209 (July 27, 1996) does not have a similar decrease in soliton energy at the NE VLA.

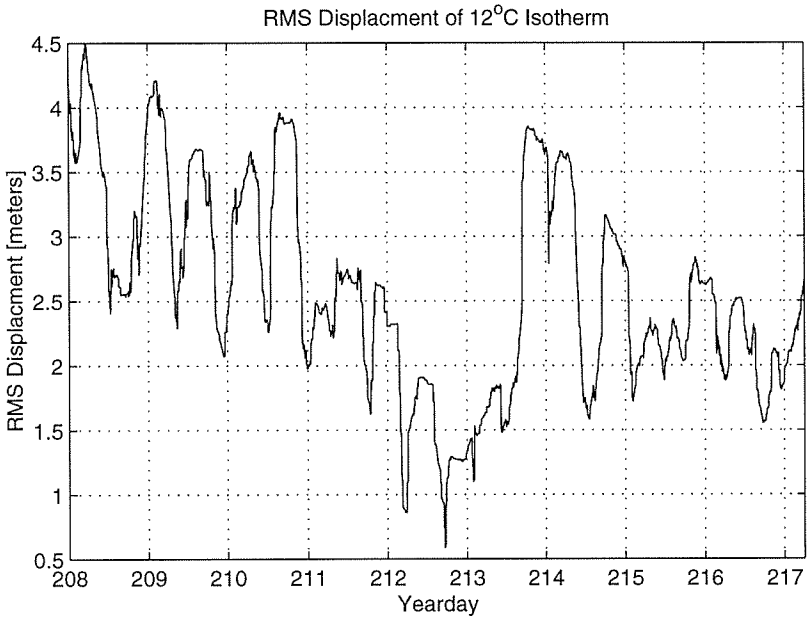

Figure 5-10: Estimate of soliton activity at NE VLA, inferred by computing RMS high-pass filtered 12°C isotherm displacement data, using a 4-hour sliding window average.

Figure 5-11 shows the power spectral density of the IQR shown in the previous figure. Note the large peak around 2 cycles per day. This is possibly due to coupling from solitons that have been generated at M_2 tidal cycles. It is also possible that other mechanisms may contribute to the IQR tidal dependence as well. For example, changes in water depth as the tide cycles perturb only the higher-order modes. In a coupled environment, energy exchange between modes that are and are not affected by elevation changes can lead to fluctuations in modes not affected under adiabatic conditions.

In Headrick et al. (1997a) it was noted that there were large increases in the IQR that were correlated with the passage of solitons by the array. In Figure 5-12, the mode 1 IQR is plotted on top of thermistor records from the NE VLA for a period of 6 days. Several spikes in the thermistor data can be traced downward to a nearby

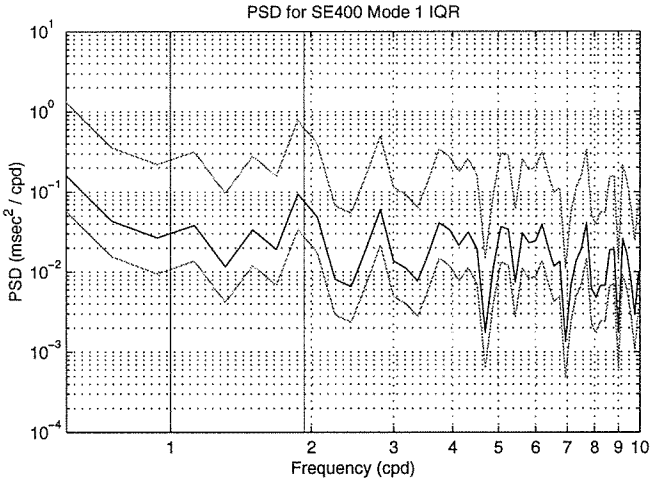

Figure 5-11: Power spectral density estimates for the SE400 Mode 1 IQR.

peak in the IQR, but many IQR peaks do not match up with solitons at the receiver. This suggests that a significant fraction of fluctuations in the IQR come from mode coupling that occurs further away from the receiver. This hypothesis is supported by the simulations carried out in Chapter 4.

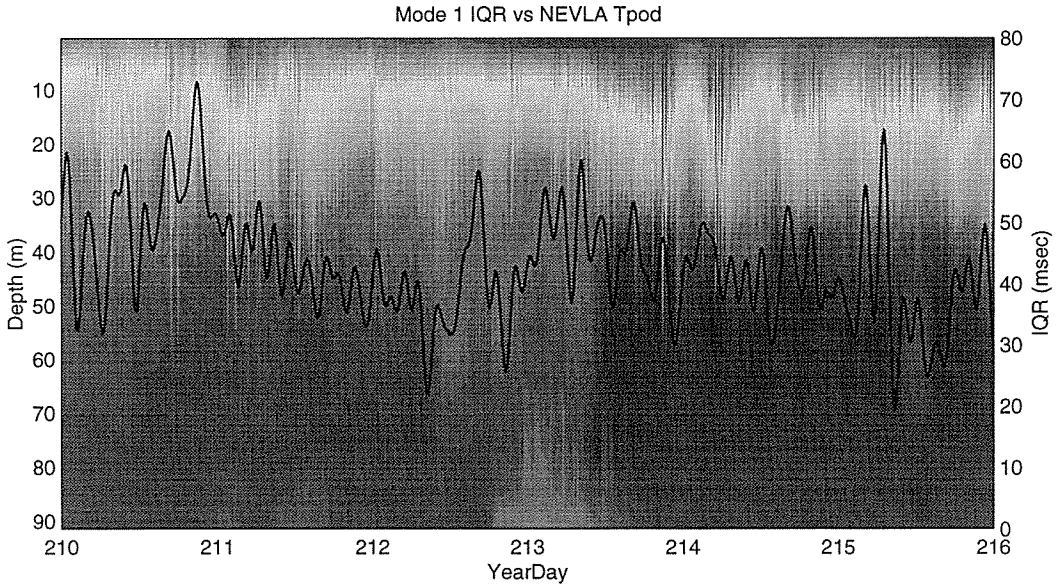

Figure 5-12: NE VLA temperature as a function of time and depth plotted against mode 1 IQR from SE400.

5.3.3 Signal Coherence

The waterfall plots at the beginning of the chapter suggested an upper bound on coherence times of around ten minutes. Given that each series of m-sequence transmissions lasted a little over 4 minutes, it is possible to look at the coherence of the mode arrivals within an individual transmission. Figure 5-13 shows the cross-correlation of the mode 1 arrival from the first sequence within a transmission series with each of the subsequent sequences within that same series. This is repeated for five consecutive transmission events. If a correlation coefficient of 0.5 is taken to be the division between coherence and incoherence, then the mode 1 arrivals are seen to decorrelate anywhere between 1 and 4 minutes. This is very similar to the findings from the SWARM Experiment (Headrick et al., 1997a), in spite of the fact that the PRIMER study region is directly over the shelfbreak.

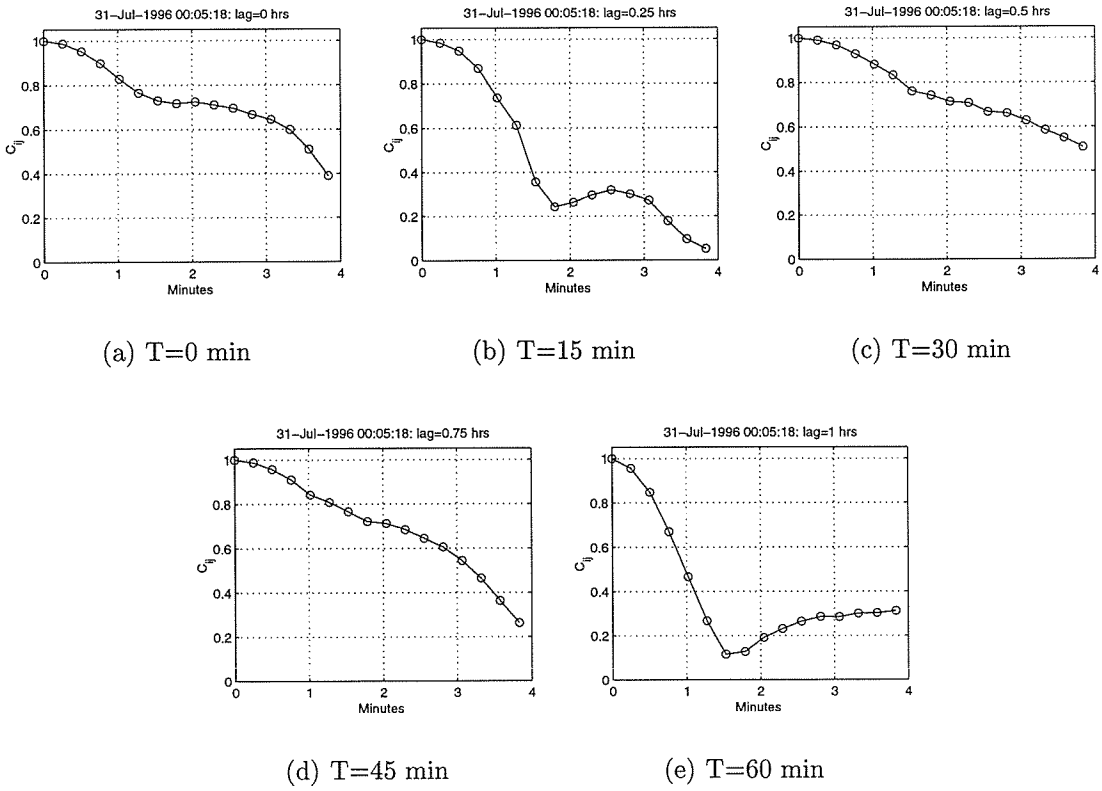

(a) T=0 min (b) T=15 min (c) T=30 min

(d) T=45 min (e) T=60 min

Figure 5-13: SE 400 Hz mode 1 coherence. Each circle represents the cross-correlation of a sequence with the first sequence within that transmission.

5.4 Comparison with the SW 400 Hz Arrivals

The presence of the SW 400 Hz source provides an additional perspective on the oceanography within the study region. Both paths have similar bathymetry, though the diagonal path (SW400) is 59.6 km long and makes a 45° angle with the shelfbreak, whereas the 42.2 km eastern path (SE400) is virtually perpendicular to the shelfbreak. The following two sections contrast the signal wander and spread between the two paths.

5.4.1 Signal Wander

Figure 5-14 shows the leading edges of mode 1 from the SE and SW 400 Hz sources. At first glance they appear quite different, and in some parts, they seem to have opposite trends. The SW400 path undergoes a total change of 170 msec, as compared with 130 msec for the SE400 path. Based on analysis of the SeaSoar data covering YD 208–214, the increase in travel time seen first in the eastern path around YD 208, and later in the diagonal path around YD 211, is consistent with the shelf water meander being pushed to the west, creating slower travel times along the occupied propagation paths. On YD 213 the SW400 path reaches its slowest travel time, and this matches very well with the SeaSoar data which shows the meander encompassing the entire SW400 propagation path at that point. The same travel time value is reached again just before YD 217, perhaps indicated that a similar environment has been reached. There are several possible explanations for the enhanced M_2 signal seen in the diagonal path. The first is that the M_2 tide is simply more energetic on the western side. Some of the thermistor data (not presented in this thesis) suggest a similar conclusion. A more-energetic tide could create either larger currents, or, as suggested by the modeling in Chapter 4, could affect travel times through changes in the mode coupling. An alternative explanation might be the positioning of horizontal temperature gradients in such a fashion that tidal advection is able to cause larger fluctuations in travel time.

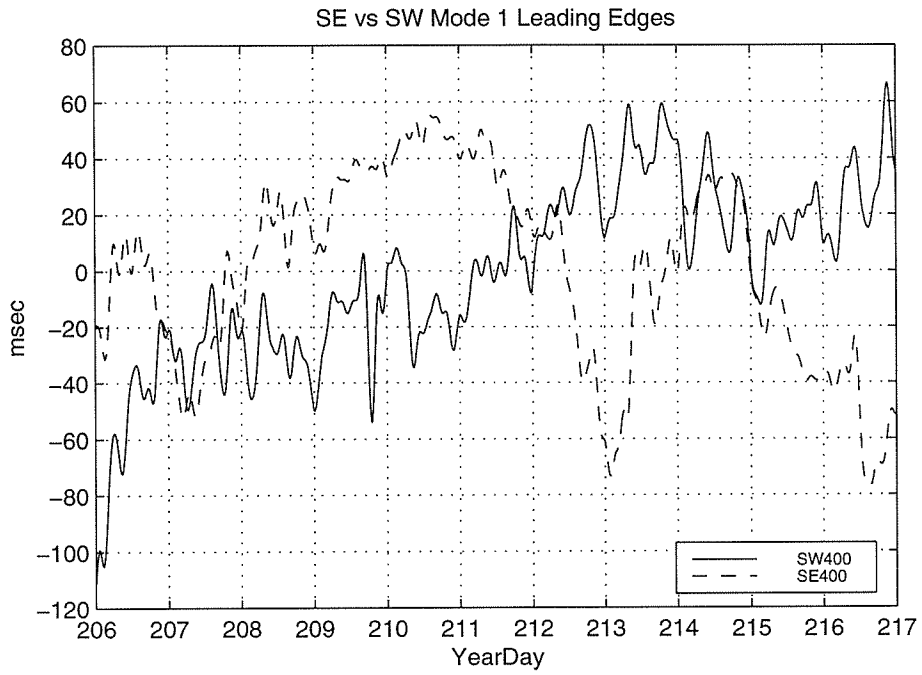

Figure 5-14: SE400 and SW400 mode 1 leading edges, with means removed. A 4-hour running average has been applied.

5.4.2 Signal Spread

Figure 5-15 shows both the SE400 and SW400 signal spreads for mode 1 arrivals over several days. Readily apparent is the fact that SW400 arrivals experience much greater spread than those along the eastern edge. A certain amount of the difference in spread may be attributed to increased effects of frequency dispersion due to the longer propagation path. A longer path also represents more opportunities for mode coupling to occur. In addition to having higher levels of spread overall, the SW400 arrival spread also shows greater variance, which again may be attributed to the longer path length.

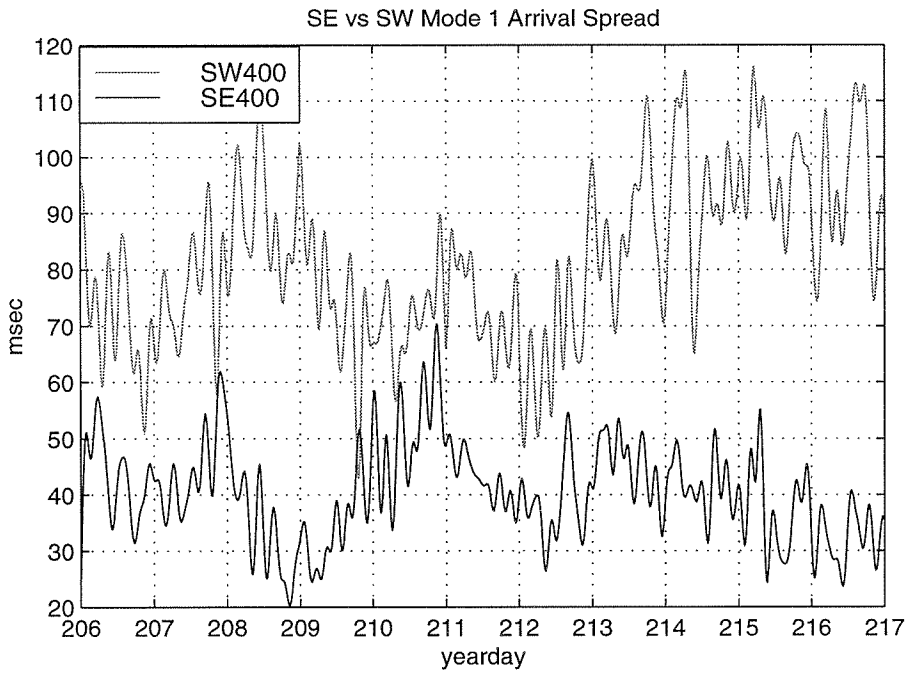

Figure 5-15: Mode 1 IQR for arrivals from SE400 and SW400 sources.

5.5 Inversions

One of the motivations in deploying the acoustic network in such a configuration as was used in the PRIMER experiments was the expectation that the gathered acoustic data could supply information about the regional oceanography (the temperature field, in particular). Such a procedure is often expressed as a mathematical inverse problem, a method commonly referred to within the community as acoustic tomography. The theoretical framework for acoustic tomography was first put forth by Munk and Wunsch (1978), specifically for the case of deep water, and has been successfully demonstrated in numerous instances (Munk et al., 1995). Deep water acoustic inversions have relied exclusively on the identification and tracking of stable ray path arrivals. One of the few exceptions has been the Greenland Sea Experiment, where a ray-based inverse was supplemented with mode travel time data (Sutton et al., 1994). Unlike in deep water, ray paths in shallow water are often very complex and difficult to track. Work from the Barent's Sea Polar Front Experiment (BSPF) looked closely at using both mode and ray data in inverse calculations (Chiu et al., 1994). While the BSPF inverse results were impressive, compared with PRIMER, the BSPF site had

only moderate range-dependence and little mode coupling. One of the main goals of this present work has been to detail exactly how strong the mode coupling can be in the region of a shelfbreak front. This forms the biggest obstacle to any sort of an acoustic inverse.

The ability to perform a standard tomographic inverse based on mode arrival time data requires an unambiguous mapping between the arrival time of an "energy packet", say in mode n, and the portion of the water column sampled by mode n during its propagation. The transfer of energy between modes, if left unaccounted for, can lead to substantial errors in the inversion. For instance, it was shown in the previous chapter that the SE 400 Hz PRIMER source excited primarily high-order modes, while at the receiver, significant energy was received in the lower modes. Without further information, it would be difficult to say whether or not a measured shift in arrival time was due to changes in the oceanography that were sampled early on by the high-order modes, or further along in the path by the lower modes, or some combination thereof. To complicate matters more, it is possible for the ocean stratification to change in such a manner that the average temperature remains the same, yet the mode coupling has been modified enough to alter the measured arrival times. An evolving soliton field might be an example of such a phenomenon.

If certain constraints may be applied to the mode coupling, for instance, assuming that the coupling occurs at only a single point in the propagation path, then an inverse is quite feasible. When the coupling is non-negligible and non-specific, varying with time and space, then accurate inversions are not possible using standard techniques. One potential approach to inverting the PRIMER acoustic data would be a non-linear, full-field approach, such as simulated annealing. Aside from the fact that such an approach would be extremely computationally-intensive, it would also rely on having good dynamical models for the oceanography, down to at least the internal-wave scale. For these reasons, a "full-blown" inversion of the acoustic data will not be attempted in this thesis. Rather, two less rigorous inverses (but insightful, nonetheless) will be considered in the following sections. The first is an attempt to estimate changes in the range- and depth-averaged temperature along the eastern propagation path, based on

perturbations in the mode arrival times. The second inverse attempts to assimilate data from the various thermistors around the PRIMER site, along with the acoustic data, into an estimate of the "strength" of the internal tide. Again, only the acoustic data collected at the northeast vertical array is being considered.

5.5.1 Inverting for Mean Temperature

The goal of this simplified inverse procedure was to see how well fluctuations in the acoustic data tracked changes in the range- and depth-averaged temperature field along the eastern propagation path, as measured by SeaSoar. The method relies on linear perturbation theory to relate changes in mode travel time to changes in water temperature. The biggest challenge in estimating the average temperature is in finding an appropriate way of treating the mode coupling and general range-dependence of the acoustic propagation. The approach taken is to simply (though not naively) assume a range-independent reference waveguide upon which the acoustic fluctuations are assumed to occur. This approach ignores the significant bathymetric changes, changes in the background sound velocity field, and all aspects of mode coupling. There is a certain amount of justification for this procedure, however. In a highly coupled environment, the influence of a perturbation to only a single mode (or group of modes) is soon felt by the entire mode field. Furthermore, as the modes reach shallower water, the differences in sampling depths of the modes become smaller, minimizing the effects of mode coupling. By estimating only an average ΔT, the sensitivity to mode coupling and range dependence is also minimized.

The perturbation in mode travel times, $\Delta\tau_n$, may be related to the local modal group slowness via the following integral over the propagation path:

$$\begin{aligned} \Delta\tau_n(r,t) &= \int_0^r \Delta s_{g_n}(r,\omega_0,t)dr \\ &= \int_0^R \int_0^D L_n(z,r,\omega_0,t)\Delta s(z,r,t)dzdr\,, \end{aligned} \tag{5.1}$$

where $\Delta s_{g_n}(r,\omega_0,t)$ is the perturbation to the mode n group velocity, evaluated at a

reference frequency ω_0, and the second equality utilizes the linear relationship between group velocity perturbations and perturbations in water column slowness. The kernel functions L_n are given by (Lynch et al., 1991):

$$L_n(r,z,t) = \frac{s^{(0)}(z)}{s_{p_n}^{(0)}(\omega)} \left(\frac{2s_{p_n}^{(0)}(\omega) - s_{g_n}^{(0)}(\omega)}{s_{p_n}^{(0)}(\omega)} \right) |\phi_n^{(0)}(r,z,\omega)|^2 + \frac{\omega s^{(0)}(z)}{s_{p_n}^{(0)}(\omega)} \frac{\partial |\phi_n^{(0)}(r,z,\omega)|^2}{\partial \omega} . \tag{5.2}$$

The independent variables of range and time have been retained to indicate that these quantities can vary with both time and space. All modal parameters (terms with subscripted n), are calculated using the reference, or unperturbed slowness profile, as indicated by the $^{(0)}$ superscript. The first term is positive semidefinite, while the second term alternates in sign with depth. For low modes and lower frequencies the first term will dominate the sum, while for higher modes and higher frequencies, the second will tend to dominate. Note that the frequency derivative in the second term can be quite small and care must be taken to retain numerical accuracy. Derivatives based on polynomial-fitting have worked well. The background waveguide used to calculate the reference mode quantities ($\phi_n^{(0)}$, $s_{g_n}^{(0)}$ and $s_{p_n}^{(0)}$) has a constant depth of 120 meters with a sound velocity profile given by the profile at the mean profile at the 120-m isobath. This implies that $L_n(r,z,t) = L_n(z)$. Figure 5-16 illustrates both the reference profile $c^{(0)}$, as well as the kernel functions for the first ten modes. The depth-structure of each L_n determines how the group slowness for a given mode will respond to water column perturbations with differing depth dependencies.

If Equation (5.1) were re-written using range-averaged quantities, $\Delta\overline{s}_{g_n}(\omega,t)$ and $\Delta\overline{s}(z,t)$, then the integrals over range may be dropped. Converting the continuous depth integral into a discrete summation allows the new equation to be written in matrix form, which is more suitable for inverting.

$$\Delta\overline{\mathbf{s}}_g = \mathbf{L}^T \cdot \Delta\overline{\mathbf{s}} . \tag{5.3}$$

The left hand side comes from the measured acoustic data. If $\tau_n(t)$ is the arrival time

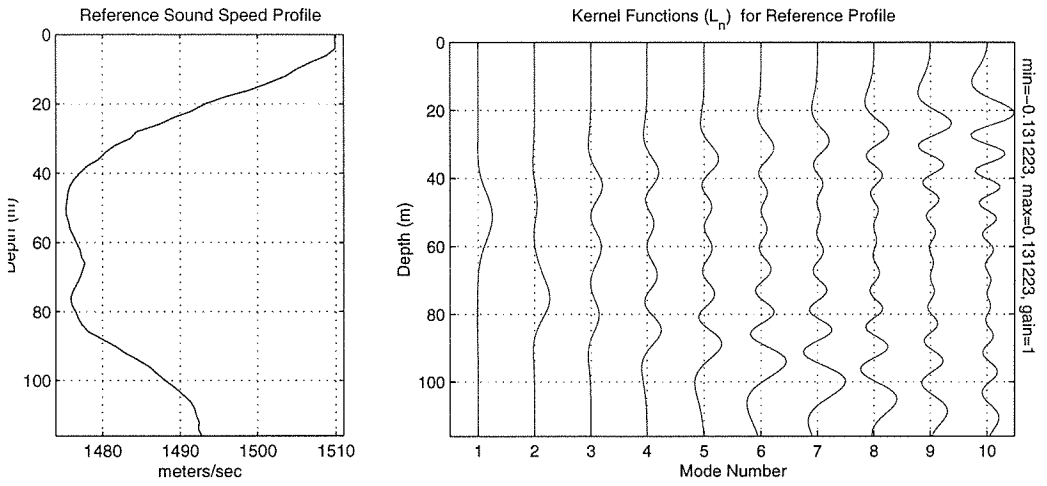

(a) (b)

Figure 5-16: Reference sound velocity profile and resulting kernel functions for the range- and depth-averaged temperature inverse.

of a given mode at time t, defined in this case by the centroid of the received signal, then an estimate of the range-averaged group velocity perturbation for a given mode is obtained by subtracting a mean arrival time and scaling by the range,

$$\Delta\overline{s}_{g_n}(t) = \frac{\tau_n(t) - \overline{\tau}_n}{R} \,. \tag{5.4}$$

It should be pointed out here that this is not strictly correct, since the group velocity of a given mode is by definition a narrowband quantity, $s_{g_n}(\omega) \equiv \frac{\partial k_n(\omega)}{\partial \omega}$, and τ is taken to be the arrival centroid of the broadband time series.

The next step is to invert (5.3) for $\Delta\overline{\mathbf{s}}$, which in turn is to be related to actual fluctuations in temperature using the following approximation

$$\Delta\overline{s}(z,t) \approx -3.6 s_o^2 \Delta\overline{T}(z,t) \,, \tag{5.5}$$

where the factor of 3.6 is an average number to account for the first-order change in sound speed per degree Celsius change in water temperature.

As it stands, the inverse is very under-determined, since $N \gg M$. A standard

method of reducing the number of unknowns is to expand the unknown $\Delta\overline{s}(z)$ into a sum of empirical orthogonal functions (EOFs), given by $w_j(z)$.

$$\begin{aligned} \Delta\overline{s}(z) &= \sum_j w_j(z) a_j \\ \Delta\overline{\mathbf{s}} &= \mathbf{W} \cdot \mathbf{a} \end{aligned}$$

The w_j are the eigenfunctions of the temperature-perturbation covariance matrix. The covariance matrix is determined by calculating the covariance of the SeaSoar profiles within a section ± 10 km in cross-shelf direction from the 120-m isobath, and 20 km in the along-shelf direction, west from the eastern edge of the domain. A snapshot of the covariance matrix formed in this manner is generated for each of the seven days of SeaSoar data, and then averaged together. The first 5 EOFs from the averaged covariance matrix, which account for over 95% of the variance, are retained for the inversion.

The coefficients a_j may be estimated via a standard least squares technique, the results of which are shown in Figure 5-17. The small dots represent range- and

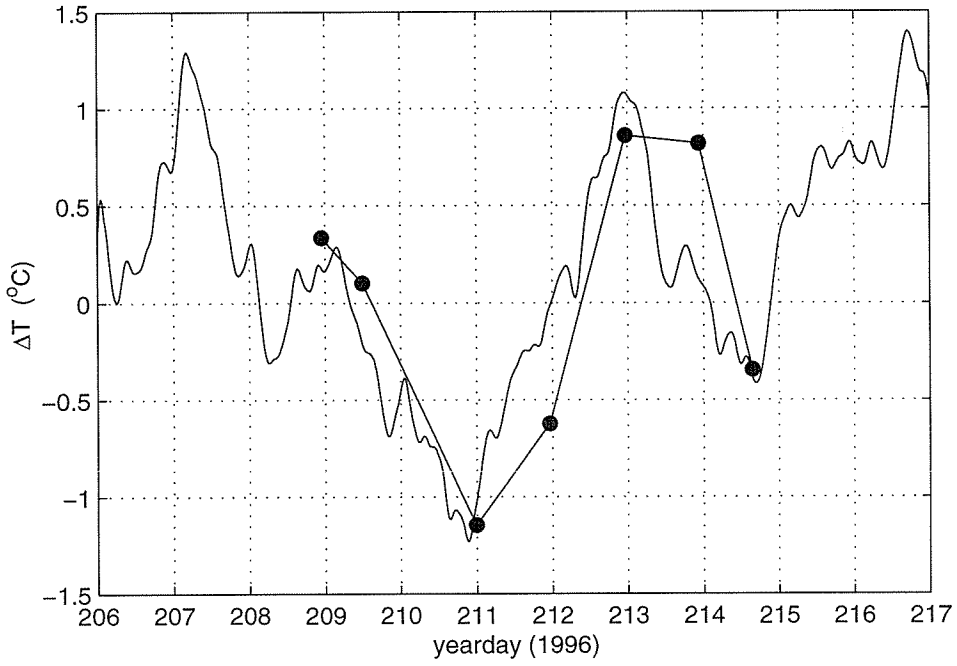

Figure 5-17: Inverse result for average temperature fluctuation along the eastern edge. Solid line is from the acoustic data, and dots are from SeaSoar.

depth-averaged temperatures computed directly from the SeaSoar records. There is reasonable agreement in the trends between the acoustic and SeaSoar results, but they do not follow exactly. Near days 212 and 214 the results are off by half-a-degree or more. There are numerous factors that likely contribute to the discrepancies, the most likely of which is mode coupling. By not taking into account the actual path through mode-space that resulted in each $\tau_n(t)$ data point, one is assured of not achieving the correct answer. Some speculation regarding the large discrepancy near Day 214 is in order. That is the day where there is the largest intrusion of the shelfbreak front northward of the SE 400 Hz acoustic source. The SeaSoar data indicate much more of a warming than the acoustic data show, relative to the seven-day mean. Recall that there was enhanced coupling into the lower modes near the front during YD 213. Also recall that over the first half of the propagation path, the lower modes are traveling the slowest. Therefore, in spite of there being more warm water near the source, much of the received acoustic energy is actually arriving later than usual because it has to travel in lower modes early on in the propagation path. If one assumes that the increase in average temperature around YD 213 is due to the front being advected north of the source, then one might surmise that similar events are happening shortly after YD 207 and a little before YD 217. This is quite consistent with observations from the thermistors on the southeastern source mooring.

5.5.2 Inversion for Internal Tides

It was observed that there were strong variations in the strength of the semidiurnal tide between thermistors at the various moorings, as well as between the two acoustic paths leading to the NE VLA. This section looks at a crude data-assimilation/inverse scheme that was developed to better visualize the spatial and temporal variability in the internal tide strength. The term "crude" is used because the acoustic data provide little, if any, depth or range resolution, a result of the unknown mode coupling along the propagation path. The goal, then, is to restrict the inversion estimate to the determination of an average "strength" of the internal tide as a function of time and acoustic path (i.e., use a very low spatial resolution). Including the thermistor data

provides not only improved spatial coverage (albeit as point measurements), but also provides a constraint on the less-accurate acoustic measurements. A more accurate acoustic inverse could be achieved by including the two propagation paths to the northwest vertical array, but those datasets were unavailable at the time of this work.

The foundation of the inverse is a model that relates the available measurements (acoustic travel times in milliseconds and temperature point measurements in degrees centigrade) to the quantity being estimated (internal tide strength). The operating assumption is that the semidiurnal internal tide in the region is described by a solibore that propagates toward the shore. This is consistent with observations from thermistor records, as well as observations made at similar shelfbreak sites. The first step is to convert both thermistor and acoustic travel time records into parameters more directly related to the internal tide. For the thermistor data, the internal tide component is estimated by extracting isotherm displacements, as discussed in Chapter 2, and applying a bandpass filtering about the semidiurnal frequency.

Processing the acoustic data is not quite as straightforward, given that the M_2 fluctuations seen in the acoustic data are probably a combination of mode coupling effects as well as changes in group velocities. The relationship between internal tide strength (as measured by either the maximum amplitude or area-under-the-curve of the isotherm displacement) and the amount of travel time variation is non-linear, primarily because of the mode coupling. Therefore, a parametric mapping between travel time perturbation and internal tide strength was utilized. To create such a mapping, broadband PE propagation runs were made through the semidiurnal solibore field for a variety of tide strengths. The general shape of the solibores was kept constant while a scale factor was applied to the amplitude. Note that this scaling of the output of the KdV internal wave model is *not* the same thing as re-scaling the initial thermocline depression that was used as input to the model, but it should be sufficient in an "average" sense. The changes in mode arrival times were tracked as a function of solibore amplitude. The result of this is a mapping that converts travel time fluctuations into "bore height," as shown in Figure 5-18. The actual mode travel time data were first corrected for barotropic current effects based on estimated

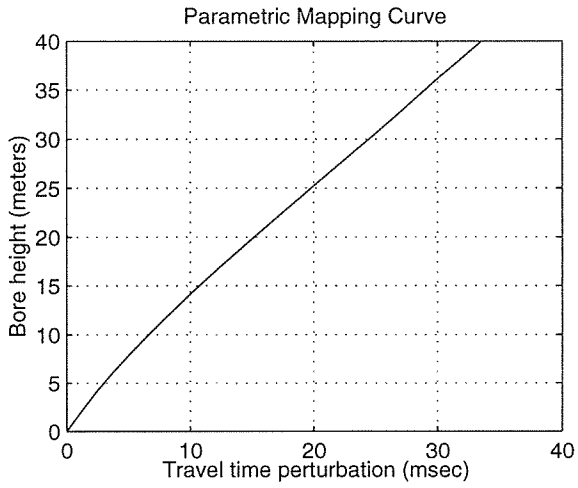

Figure 5-18: Parametric map used to convert acoustic travel times into equivalent internal tide strengths.

barotropic tidal currents, and then bandpass filtered about the semidiurnal frequency, just as the thermistor data were. The filtered travel times were then converted into bore heights using the parametric mapping.

The M_2-filtered and processed thermistor and acoustic data were integrated over each 12.42-hour period, yielding 16 sample points for each measurement source over the eight-day period used in the inversion. Figure 5-19 illustrates the integration process for the acoustic path from SE 400 source to NE VLA.

Before going any further with the inverse, it is important to establish estimates for the data variances for the acoustic data. Recall that each 15-minute estimate of the arrival centroid for a given mode was the result of averaging over 48 successive m-sequences. On average, the variance of the centroid estimate over those 48 sequences range from 31 msec^2 for mode 1 to 123 msec^2 for mode 10. After bandpass filtering, the variance was reduced to less than 1 msec^2. The real source of variance in the acoustic data comes from the parametric mapping processing. Taking this into account, a somewhat large variance of 20 msec^2 was assigned to the acoustic-based data (33 meters^2 after mapping).

With the measurements in the proper format, the next step is implementing the

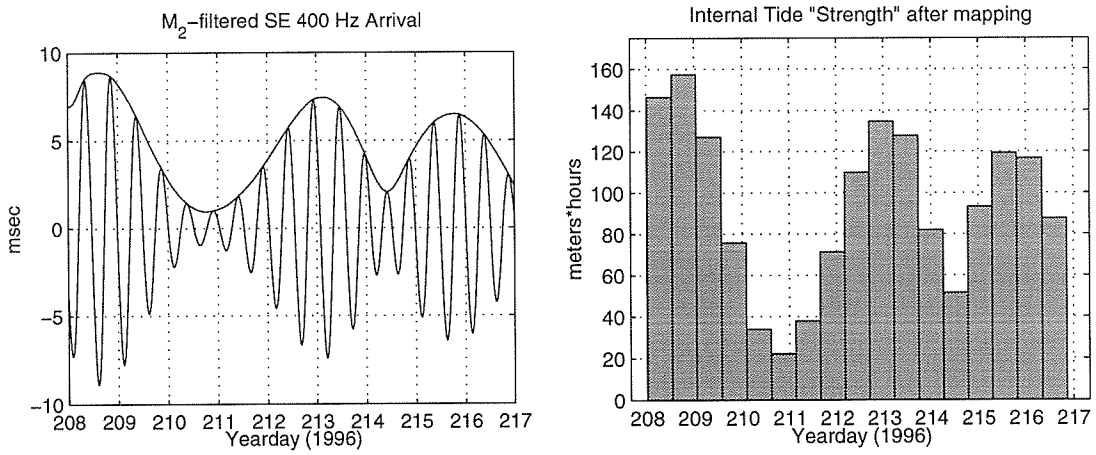

(a) SE 400 arrival times.

(b) Area-under-the-curve mapping.

Figure 5-19: Integrating the processed acoustic displacements over successive 12.42-hour periods.

inverse. The canonical inverse equation is typically expressed in the following manner,

$$\mathbf{y} = \mathbf{E}\mathbf{x} + \mathbf{n}\,, \tag{5.6}$$

where $\mathbf{y}$ is a column vector containing data measurements (i.e., thermistor- and acoustic-based) and $\mathbf{x}$ is a column vector representing the oceanographic field parameter of interest (i.e., solibore height at each spatial grid point). The vector $\mathbf{n}$ represents noise in the measurement process, and the matrix $\mathbf{E}$ linearly relates ocean parameters to data measurements. Given the above expression, an estimate of $\mathbf{x}$ is desired.

The linear inverse solution providing the minimum mean-square error is given by the Gauss-Markov inverse. Thorough discussions of the method may be found in Wunsch (1996), and good discussions of its application to acoustic tomography may be found in Chiu and Lynch (1987); Chiu et al. (1994); Munk et al. (1995). The standard equations for the Gauss-Markov estimate $\hat{\mathbf{x}}$, and the resulting estimate and

error covariances $\mathbf{P}_{\hat{x}\hat{x}}$ and $\mathbf{P}_{nn}$, may be written as:

$$\begin{aligned}
\hat{\mathbf{x}} &= \mathbf{R}_{xx}\mathbf{E}^T\left(\mathbf{E}\mathbf{R}_{xx}\mathbf{E}^T + \mathbf{R}_{nn}\right)^{-1}\mathbf{y}\,, \\
\mathbf{P}_{\hat{x}\hat{x}} &= \mathbf{R}_{xx} - \mathbf{R}_{xx}\mathbf{E}^T\left(\mathbf{E}\mathbf{R}_{xx}\mathbf{E}^T + \mathbf{R}_{nn}\right)^{-1}\mathbf{E}\mathbf{R}_{xx}\,, \\
\mathbf{P}_{nn} &= \left\{\mathbf{I} - \mathbf{E}\mathbf{R}_{xx}\mathbf{E}^T\left(\mathbf{E}\mathbf{R}_{xx}\mathbf{E}^T + \mathbf{R}_{nn}\right)^{-1}\right\}\mathbf{R}_{nn}\,.
\end{aligned}$$

R_{xx} represents the a priori cross-correlation of the oceanographic parameters being estimated, and R_{nn} the second-moment of the measurement noise, which may also include "noise" attributed to suspected errors in the model (Chiu and Lynch, 1987). For the purposes of this inverse, it will be assumed that $\mathbf{R}_{nn} = \mathrm{diag}(\sigma_n^2)$, where σ_n^2 is zero for the thermistor data, and 20 msec^2 for the acoustic data. The a priori covariance of the bore strength was assumed to be $\mathbf{R}_{xx} = 5^2\mathbf{I}$.

In addition to relying on the solution error estimate for providing interpretation of the inversion solution, estimating the resolution of the inverse is also useful. Numerous possibilities exist for measuring the resolution of an inverse technique. Conceptually, resolution may be thought of as the estimator response when the true field consists of an impulse function at a particular point in space (and/or time). The more the estimate differs from an impulse, the less the resolving power of the inversion. A numerical quantity may be attached to the resolution along any given coordinate-axis by computing the distance within which half of the total energy of the resolution kernel is confined (Chiu et al., 1994). The method used here differs slightly from the previous in that the second-moment of the resolution kernel in a given direction is computed at each point, according to

$$\begin{aligned}
r_x(x_o, y_o, z_o) &= \int (x - x_o)^2 F(x, y, z; x_o, y_o, z_o)dx \\
r_y(x_o, y_o, z_o) &= \int (y - y_o)^2 F(x, y, z; x_o, y_o, z_o)dy\,,
\end{aligned}$$

where F represents the impulse response to a unit perturbation at location (x_o, y_o, z_o). Figure 5-20(a) illustrates the resolution of the inverse with the thermistors and the two acoustic paths to the northeast.

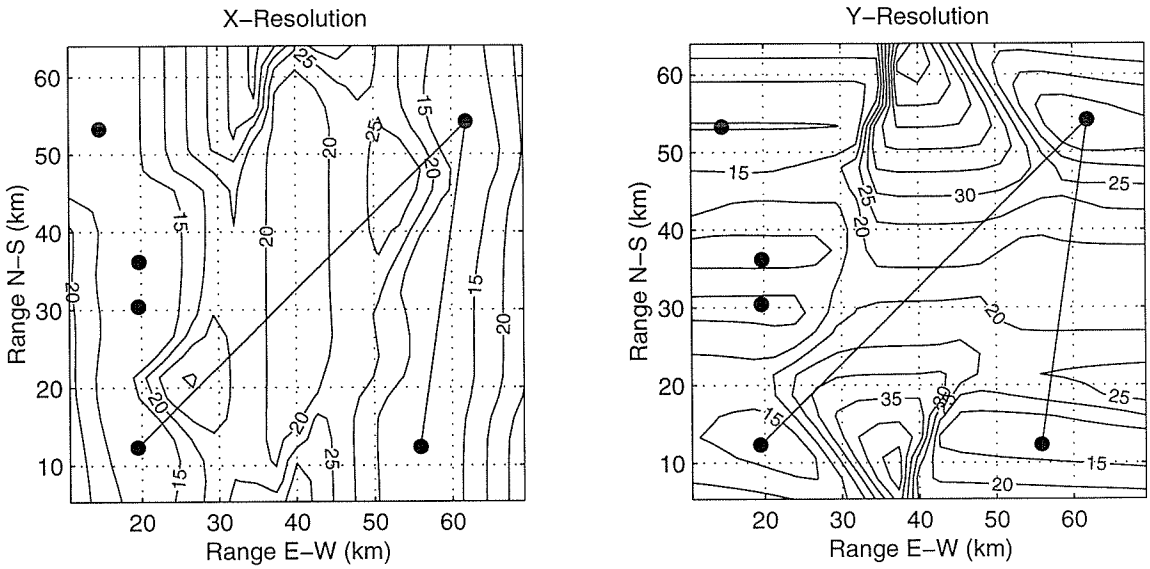

(a) Resolution (in km) in X and Y directions.

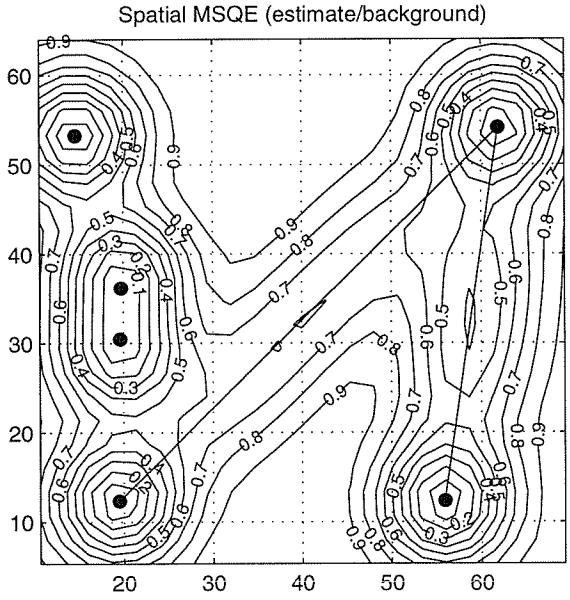

(b) Estimate MSQE.

Figure 5-20: Inverse resolution and spatial mean square error of the estimate.

Figure 5-20(b) illustrates the mean square error of the estimate for the given geometry. What is plotted is actually the ratio of the mean-square error (MSQE) of the estimate to the underlying mean-square perturbations of the environment. For an estimate in which one has very little confidence in the data (i.e., very large measurement variance), the MSQE ratio goes toward one. A very good measurement allows the inversion process to greatly reduce the variance over that of the underlying environment.

Figures 5-21 – 5-23 show the inversion results using thermistor only, acoustic only, and combined acoustic and thermistor data. Each panel corresponds to the estimated area-under-the-curve tide strength (in units of meters·hours) for sixteen consecutive semidiurnal tidal periods. All estimate values for which the MSQE ratio discussed above is greater than 0.9 are masked out to prevent erroneous interpretations of the inversions. There does appear to be some degree of correlation between tidal strength estimates from acoustic-based measurements and those based on thermistor data. For instance, during yeardays 208 and 209, the levels along the two acoustic paths tend to track the thermistor levels at the two southern source locations. Another observation to be made is that along the western side the tide strength is consistently stronger midway between the SW and NW moorings. This corresponds to the range where the leading edge of the internal solibore is at its steepest, usually with very large solitons present in the vicinity. Because there is no thermistor coverage at a similar point on the eastern edge, one should not say too much about the along-shelf variability. By using the acoustic data, however, one can place some bounds on what conceivably could be happening on the eastern side. Looking at the combined results in Figure 5-23, one sees that the internal tide does not appear to be as strong on the eastern side, suggesting perhaps that the tides are a little weaker along that side.

Other than to give a general sense of the possible distribution of internal tide levels across the region, there is not much more to be gained from such an inversion at this point. More work needs to be done in validating the parametric mapping procedure before one is able to place much trust in the actual numbers returned from the inversion.

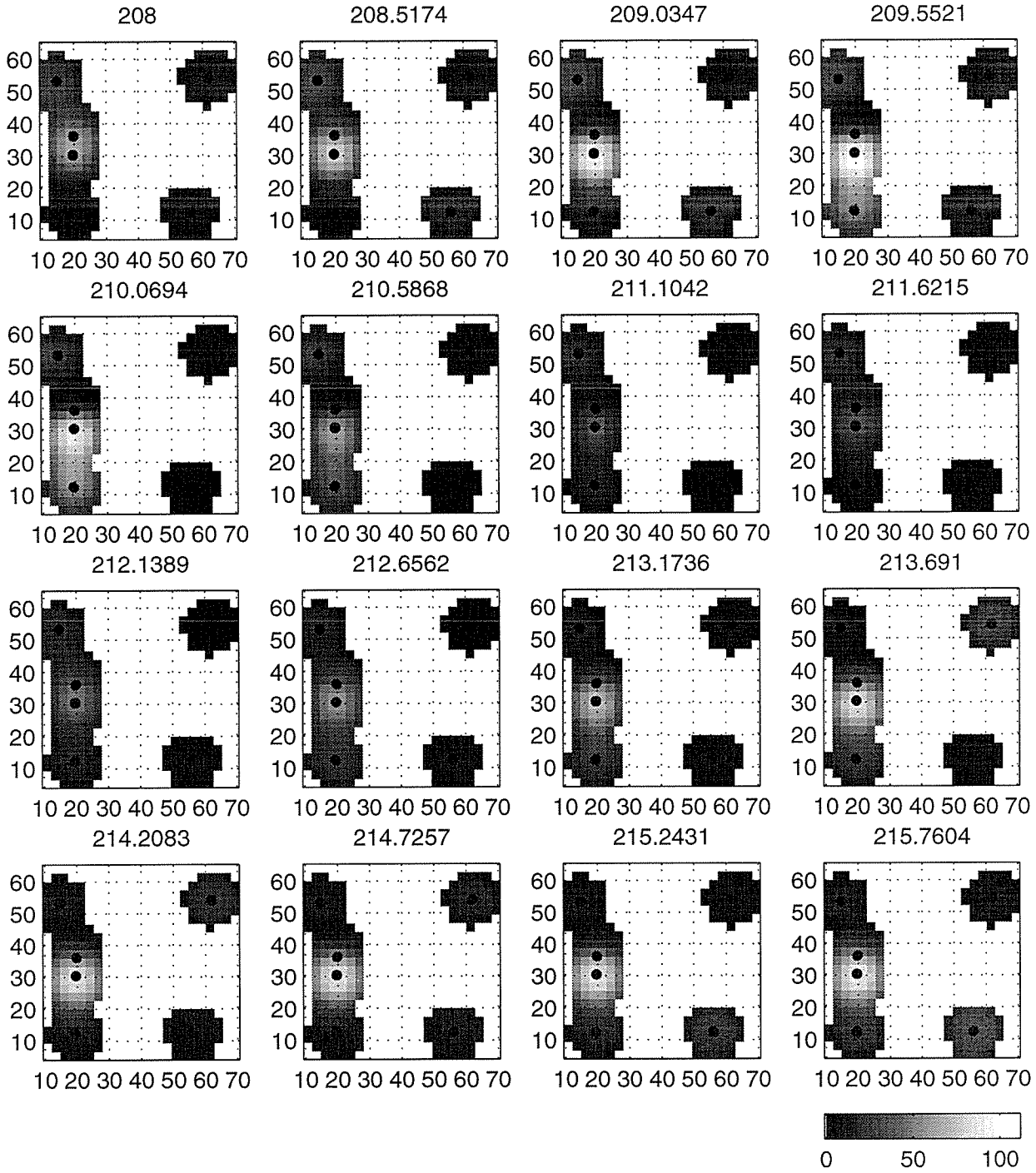

Figure 5-21: Inversion for internal tide "strength" using only thermistor data. Units are in meters·hours.

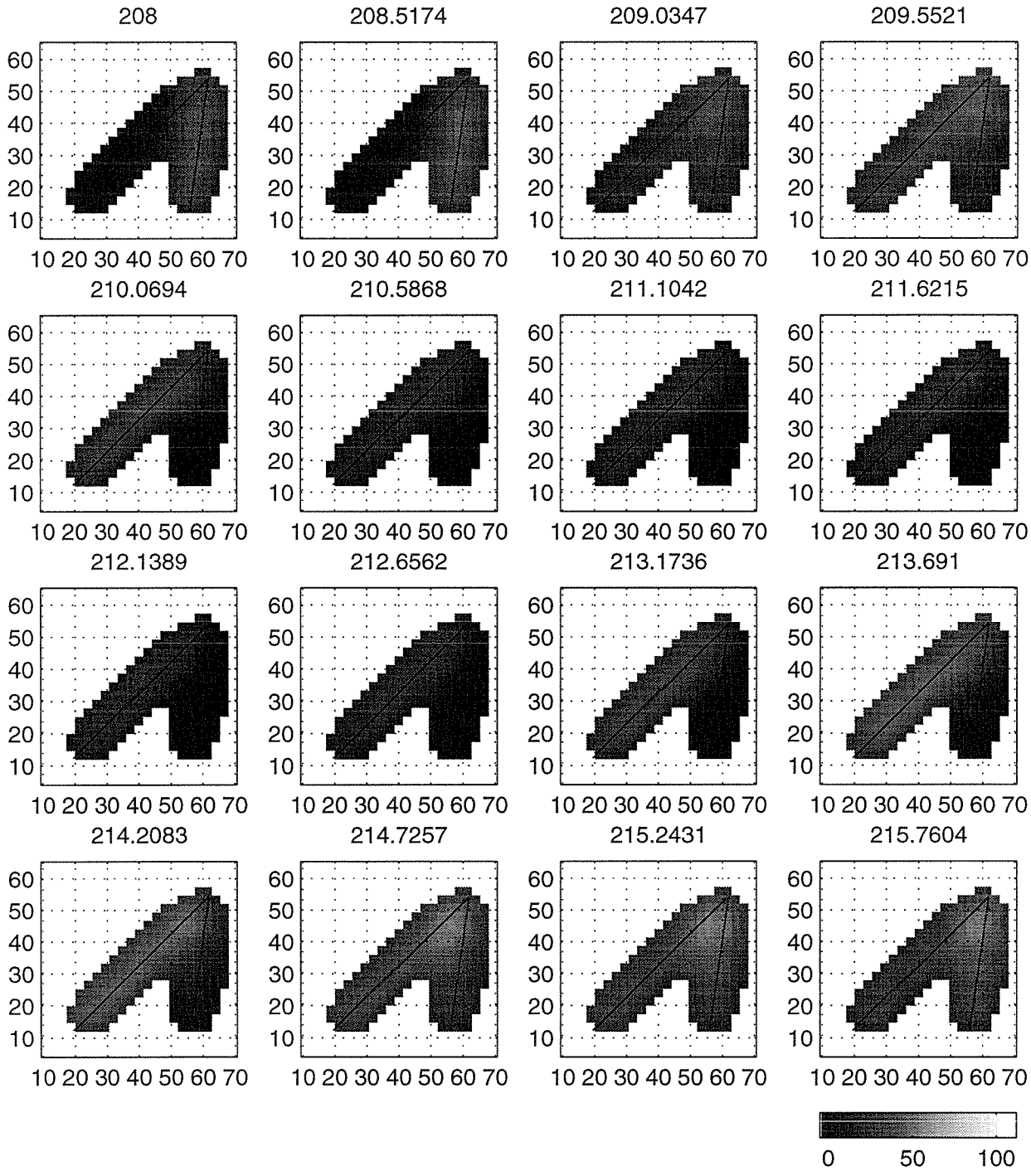

Figure 5-22: Inversion for internal tide "strength" using only acoustic data at the northeast VLA. Units are in meters·hours.

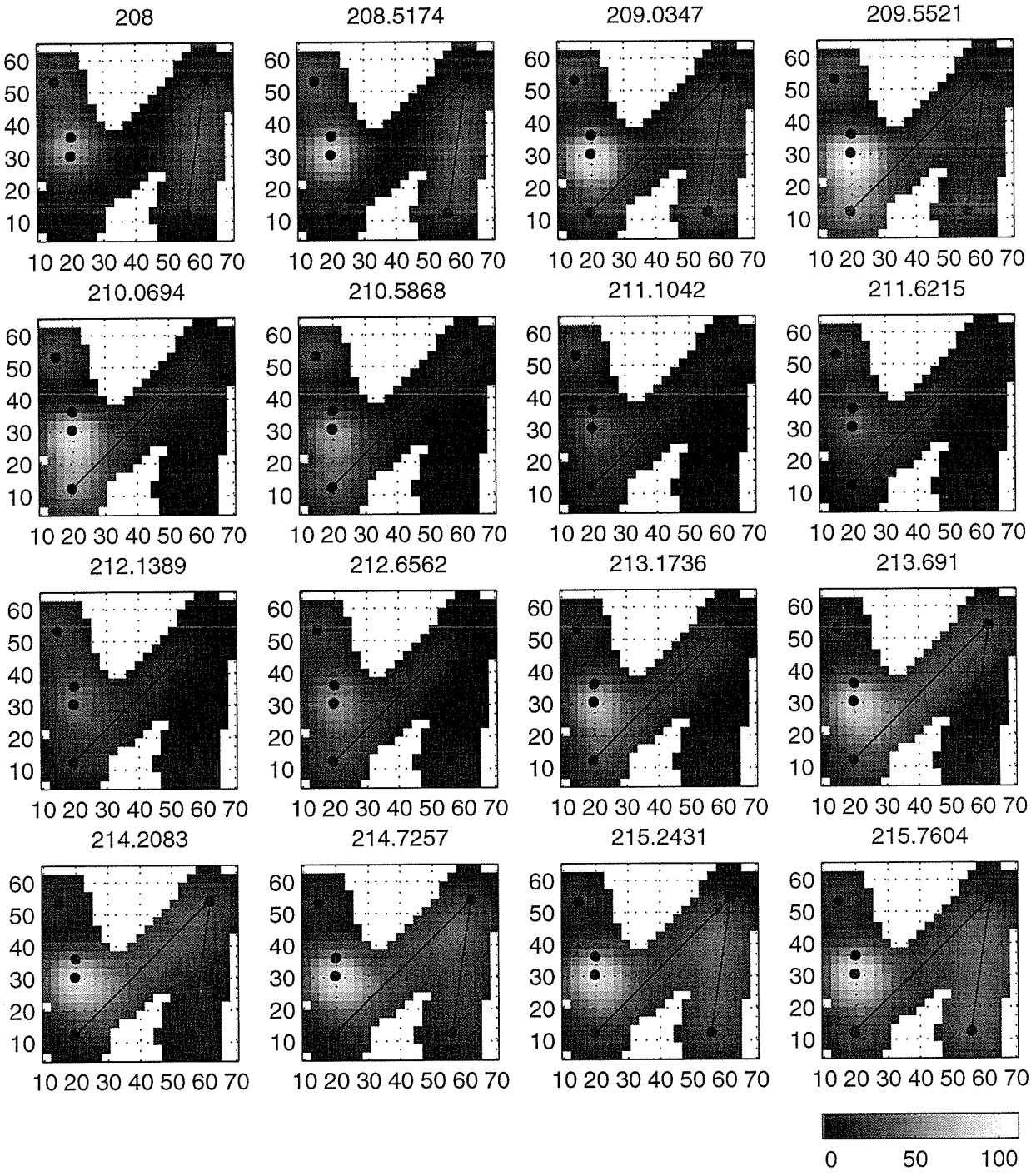

Figure 5-23: Inversion for internal tide "strength" using combined acoustic and thermistor data. Units are in meters·hours.

Chapter 6

Normal Mode Coherence Theory

6.1 Introduction

By this point it should be abundantly clear that acoustic propagation in shallow water can be extremely complicated. Factors affecting the propagation range from fronts and eddies, to internal solitary waves, to sea surface and bottom roughness as well as sub-bottom structure. One extremely useful measure of the impact of the environment on the propagation is the coherence of the acoustic field. This chapter represents a departure from the previous ones in that it focuses on a simplified environment model for the purposes of theory development, and only a few statistical parameters obtained from the summer PRIMER oceanography data are utilized. The development of a methodology aimed at understanding the effect of environmental variability on acoustic coherence is pursued in this chapter.

Generally speaking, coherence is a measure of the similarity between two signals that are measured at some separation from one another. The "separation" between the two measurements may be in their location, orientation, time, frequency or any combination thereof. In addition to these different flavors of coherence, one may also consider coherence between specific aspects of a propagating acoustic field. For instance, different multipaths (i.e., different rays/modes) may be more or less coherent with one another depending on the environment. The coherence at various separations along the wavefront associated with a particular ray or mode will also vary. It can be

shown that the coherence of the total acoustic field (signal, noise and reverberation) plays a key role in determining the performance of array processing systems (active or passive, adaptive or non-adaptive). For this reason, it has generated a great deal of interest over the years.

Many studies and experiments have looked at a variety of coherence issues. One set of experiments found that in shallow water, a 400 Hz acoustic field remained coherent over a horizontal extent of 30 wavelengths (112 meters at 400 Hz) out to a range of 45 kilometers (Carey, 1998). It is very difficult to make more than broad generalizations based on experimental coherence measurements since the exact conditions under which such measurements might have been taken are virtually impossible to duplicate. This fact largely motivates developing a more theoretical approach to understanding how environmental variability affects coherence. In addition, such coherence models may be useful in certain matched field processing applications.

In the next section, the standard expression for coherence is written in terms of normal mode theory. A key element in that expression is the modal phase difference. Borrowing from previous work involving wave propagation in random media, the phase structure function is defined for individual modes. It is this modal phase structure function that will be of interest in this chapter.

6.2 The Modal Phase Structure Function

6.2.1 Definition of Coherence

The coherence between two samples of the pressure field, p, is commonly written in the form of a cross-correlation coefficient, indicated by C_p:

$$C_p = \frac{\langle p_1 p_2^* \rangle}{\sqrt{\langle |p_1|^2 \rangle} \sqrt{\langle |p_2|^2 \rangle}}, \tag{6.1}$$

where the brackets $< \cdot >$ indicate ensemble averages. There are numerous issues that arise when trying to calculate such ensemble averages on actual data (e.g., the "snapshot" problem). Such issues will not be addressed at first; rather it will be

assumed for now that an infinite series of measurements are available for calculating the statistics. The issue of finite statistics will be taken up later. Since we are interested in acoustic propagation in shallow water, it is reasonable to express the pressure field p as a sum of normal modes. In shorthand notation, where the mode amplitudes and modeshapes (evaluated at specific depths) have been combined into a single variable, a_n, this becomes:

$$p = \sum_n a_n e^{ik_n r} = \sum_n p_n \,, \tag{6.2}$$

where $k_n r = \theta_n$ is the spatial phase at range r for mode n, along the path of propagation.

Consider for the moment the simple case of just two modes present in a waveguide. For the sake of an example, suppose the field is measured at two separate points in space, r_1 and $r_2 = r_1 + \Delta r$. The numerator of the coherence expression given in (6.1) may be written as the following (assuming mode amplitudes remain constant between the two points, which is usually a good assumption):

$$\begin{gathered}
\langle p(r_1)p^*(r_2)\rangle = \left\langle (a_1 e^{ik_1 r_1} + a_2 e^{ik_2 r_1})(a_1 e^{-ik_1 r_2} + a_2 e^{-ik_2 r_2})\right\rangle = \\
\left\langle a_1^2 + a_2^2 + a_1 a_2 e^{-i(k_1-k_2)\frac{\Delta r}{2}} \left[e^{i(k_1-k_2)r_1 + i(k_1-k_2)\frac{\Delta r}{2}} + e^{-i(k_1-k_2)r_1 - i(k_1-k_2)\frac{\Delta r}{2}}\right]\right\rangle = \\
\left\langle a_1^2 + a_2^2 + 2a_1 a_2 e^{-i(\theta_1'-\theta_2')} \left[\cos(\theta_1-\theta_2)\cos(\theta_1'-\theta_2') - \sin(\theta_1-\theta_2)\sin(\theta_1'-\theta_2')\right]\right\rangle
\end{gathered}$$

For the general case of multiple modes, this may be compactly written as

$$\langle pp'^* \rangle = \left\langle \sum_{m<n} \left[a_n^2 + 2a_m a_n e^{-i(\theta_m'-\theta_n')} \cos(\theta_m - \theta_n + \theta_m' - \theta_n')\right]\right\rangle \tag{6.3}$$

Notice how it is the phases that exert the most influence on the coherence. In particular, it is the modal phase *differences* that play the key role. Amplitudes are less of a concern, as beamformer outputs are generally less sensitive to fluctuations in amplitude than in phase.

Since the phase differences are critical, it is important to develop a good physical

model of how variability in the environment translates into variability of these phase differences. Although focusing on individual modal phases rather than the full field phase may seem rather indirect, it is not impractical to work with individual modes. One can theoretically filter a received signal for the individual modes, even on a horizontal array, via endfire steering (Clay and Medwin, 1977) or horizontal focusing, if in the nearfield (Lynch, 1983).

6.2.2 Deriving the Phase Structure Function

The phase structure function (PSF) (Esswein and Flatté, 1981; Flatté, 1979) was originally developed in the context of describing wave propagation in random media. For two raypaths of some separation, the PSF is defined as

$$D(2,1) = \left\langle \left[q_o \int_1 \mu(\mathbf{x}) d\mathbf{x} - q_o \int_2 \mu(\mathbf{x}) d\mathbf{x} \right]^2 \right\rangle . \tag{6.4}$$

Paths 1 and 2 may be any two paths separated in either time, space or both. The variable q_o represents a reference wavenumber and μ the medium index of refraction, a function of space and time. While this has proven quite useful in deep water situations where ray theory is applicable, in shallow water one is more interested in a modal interpretation. For modes, the PSF may be written, quite simply, as

$$D(2,1) = \left\langle (\theta_1 - \theta_2)^2 \right\rangle , \tag{6.5}$$

where θ_1 and θ_2 might represent the received modal phases for differing times, locations or mode numbers.

Consider the phase for mode n in more detail. It may be broken into two parts, a deterministic component and a random one. In practice, the amount of phase that can be determined correctly from the measured environment and modeled is considered the deterministic part, θ_n^0, and everything else falls into the random part, $\Delta\theta_n$. Thus,

one has $\theta_n = \theta_n^0 + \Delta\theta_n$, and the modal phase structure function becomes

$$D(1,2) = \theta_1^2 + \theta_2^2 + \left\langle (\Delta\theta_2 - \Delta\theta_1)^2 \right\rangle , \tag{6.6}$$

where it has been assumed that the $\Delta\theta_i$ are uniformly distributed from $-\pi$ to π, and may or may not be correlated. Since we are mainly interested in the random part of the signal, let assume that the modeled portion of the phase has been subtracted from both sides of (6.6), leaving:

$$D(1,2) = \left\langle (\Delta\theta_2 - \Delta\theta_1)^2 \right\rangle \approx 2\Delta \left\langle \theta_1^2 \right\rangle - 2 \left\langle \theta_1 \theta_2 \right\rangle . \tag{6.7}$$

Representing the random phase components in WKB integral fashion (Clay and Medwin, 1977), $\Delta\theta_n$ is written as:

$$\Delta\theta_n = \int_0^R \Delta k_n(r) dr . \tag{6.8}$$

The integral is along a propagation path through the horizontal coordinate space x and y. (Recall that WKB representation of modal phase is a 2-D function in the horizontal, where the modeshapes account for propagation in the vertical direction.)

Using the formulation suggested by both Shang and Wang (1991) and Lynch et al. (1991), $\Delta k_n(r)$ can be related to the environment variability using linear perturbation theory, as given by

$$\Delta\theta_m = \int_0^R \Delta k_m dr = \frac{-1}{k_m^0} \int_0^R \int_0^\infty \rho_0^{-1} |\phi_m^{(0)}(z;r)|^2 \frac{k_o^2}{c_o} \delta c(r,z) dz dr . \tag{6.9}$$

The depth integral is from the sea surface down to an infinite depth below the seabed. This allows contributions to $\Delta\theta_m$ from perturbations within both the water column and the bottom. The range integral is over the propagation path from source to receiver. Since this is for modal propagation, the path is within the horizontal plane, though it need not be a straight line. The wavenumber perturbation expression used in (6.9) has many other applications, including the calculation of group velocity

perturbations (Lynch et al., 1989).

The next step is to substitute (6.9) into the latter term in (6.6). Looking at the auto-correlation terms first, one has:

$$\begin{aligned}\langle \Delta\theta_1^2 \rangle &= \left\langle \left[\frac{1}{k_m^0} \int_0^R \int_0^\infty \rho_0^{-1} |\phi_m^{(0)}(z;r)|^2 \frac{k_o^2}{c_o} \delta c(r,z) dz dr \right] \right. \\ &\quad \left. \cdot \left[\frac{1}{k_m^0} \int_0^R \int_0^\infty \rho_0^{-1} |\phi_m^{(0)}(z';r')|^2 \frac{k_o^2}{c_o} \delta c(r',z') dz' dr' \right] \right\rangle ,\end{aligned}$$

where the two range integrals are over the same propagation path.

To simplify notation, define a kernel function, G_m, containing all of the mode information as follows:

$$G_m = \frac{-1}{k_m^0} \rho_0^{-1} |\phi_m^{(0)}(z;r)|^2 \frac{k_o^2}{c_o} . \tag{6.10}$$

Substituting this into the previous expression, and bringing the averaging brackets inside the integrals gives

$$\langle \Delta\theta_1^2 \rangle = \int\int_0^R \int\int_0^\infty G_m G'_m < \delta c \delta c' > dz dz' dr dr' . \tag{6.11}$$

Since the kernel function is based on a reference environment and is therefore deterministic, the only stochastic quantity is the sound speed perturbation, δc. At this point, it is useful to define the sound speed correlation function, C, to be

$$C(\mathbf{r}_1, \mathbf{r}_2) = \langle \delta c(\mathbf{r}_1) \delta c(\mathbf{r}_2) \rangle . \tag{6.12}$$

Now consider the cross terms from (6.5). As an example, assume a single mode, m, is measured at different locations in space, R_1 and R_2. The path integrals to the points R_1 and R_2 are 2-D functions of (x,y), and have along-path coordinates of s_1

and s_2, respectively. Let $\theta_1 = \theta_m(R_1)$ and $\theta_2 = \theta_m(R_2)$.

$$\begin{aligned}\langle \Delta\theta_1 \Delta\theta_2 \rangle &= \left\langle \frac{1}{k_m^0} \int_0^{R_1} \int_0^{\infty} \rho_0^{-1} |\phi_m^0(z; s_1)|^2 \frac{k_o^2}{c_o} \delta c(x, y, z) ds_1 dz \right. \\ &\quad \left. \cdot \frac{1}{k_m^0} \int_0^{R_2} \int_0^{\infty} \rho_0^{-1} |\phi_m^0(z; r_2)|^2 \frac{k_o^2}{c_o} \delta c(x, y, z) ds_2 dz \right\rangle \\ &= \int_0^{R_1} \int_0^{R_2} \iint_0^{\infty} G_m(z_1, s_1) G_m^*(z_2, s_2) \langle \delta c(s_1, z_1) \delta c(s_2, z_2) \rangle \, ds_1 dz_1 ds_2 dz_2 \\ &= \int_0^{R_1} \int_0^{R_2} \iint_0^{\infty} G_m(z_1, s_1) G_m^*(z_2, s_2) C(s_1, s_2, z_1, z_2) ds_1 dz_1 ds_2 dz_2 \end{aligned} \tag{6.13}$$

At this point it should be pointed out that Krolik (Krolik, 1992) has used the same expressions for mean square modal phase difference in the context of robust matched field processing. In order to reduce beamformer sensitivity to environmental mismatch, constraints were applied to the beamformer response over a realistic set of environmental perturbations. The Green's function was calculated in terms of normal modes, and so the environmental variability was then introduced into the formulation essentially via Eqns. (6.11) and (6.13).

Continuing on with the development, there are three assumptions that can be made to simplify the formulation. (All can be relaxed at a future point.) First, assume that the propagation is range independent. This implies $G_m(x, y, z) \rightarrow G_m(z)$. Until now, the theory has been fully adiabatic, allowing for modeshape variation with range. The second assumption is that of a homogeneous and isotropic medium. This implies that the correlation function $C =< \delta c \delta c' >$ is only a function of measurement separation. Note that this assumption is *not* being made for depth variations.

The final assumption is to consider a specific propagation geometry that will make the analytic formulation more straightforward. Assume that there is straight-line propagation to two points, R_1 and R_2, as shown in Figure 6-1. Note that the y-coordinate of the propagation path is solely a function of x, as given by $\overline{\Delta y}(x) = x\Delta y/R$. The sound speed correlation, C, is a function of six coordinates, $x_1, x_2, y_1, y_2, z_1, z_2$. Using the above assumptions, we can transform the problem into a more convenient set of variables by using a relative and center-of-mass coordinate (RCM) system. The new coordinates will be X, x, Y, y, z_1, z_2, where $X = (x_1 + x_2)/2$,

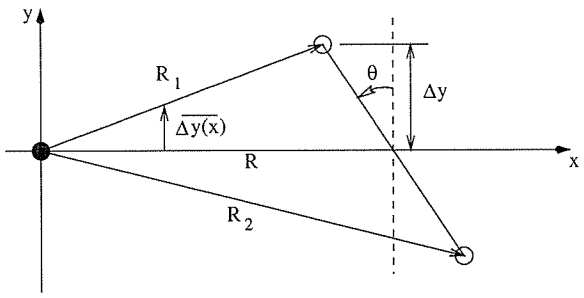

Figure 6-1: Simplified propagation geometry for coherence calculations. Open circles represent receivers, and the origin is centered at the source position.

$x = x_1 - x_2$, etc.. Note that the Jacobian of the transformation from x_i, y_i to x, X is 1. The integration is now over X and x, with the caveat that C is still an implicit function of the vertical separation $\overline{\Delta y}(X)$.

The cross-term from the phase difference equation is now as follows:

$$\langle \Delta\theta_1 \Delta\theta_2 \rangle = \int_0^{R_1'} \int_0^{R_2'} \iint_0^{\infty} dx\, dX\, dz_1\, dz_2\, \gamma\, G_m(z_1)\, G_m(z_2)\, C(X, x, y(X)) \;, \quad (6.14)$$

where

$$R_1' = R\left(1 - \frac{L}{2R}\sin\theta\right)$$

$$R_2' = R\left(1 + \frac{L}{2R}\sin\theta\right)$$

$$\gamma = \frac{\sqrt{1 + \left(\frac{L}{2R}\right)^4 + \frac{L^2}{4R^2}(1 - 2\sin^2\theta)}}{\left(1 - \frac{L}{2R}\sin\theta\right)}$$

The parameter γ represents the Jacobian of the transformation from along-path coordinates, ds, to the Cartesian $x-$,$y-$,$z-$ coordinate system. Under certain circumstances, R_1', R_2' and γ may be replace by R, R and 1, respectively. The appropriate condition is that the source be in the far-field of the receivers, where the transition range from near- to far- field for mode n is given by (Lynch, 1983):

$$R_n^{N-F} \simeq \frac{\Delta y^2 k_n}{\pi} \,. \quad (6.15)$$

All of the propagation considered here is assumed to be in the far-field of the *source*, where the large-argument asymptotic expansion of the Hankel function is valid. For purposes of analytic simplicity, we will also only consider, from here on, cases in which the source-receiver separation is greater than the receiver near-field.

The depth integrals have been explicitly left in regular z_1, z_2 coordinates, since the RCM system affords little benefit when there is an expected depth dependence to the correlations (i.e., inhomogeneity). The primary benefit of RCM is to make calculating the correlation function easier, which in turn allows the two range integrals to be evaluated, leaving behind only the two depth integrals for the computer to calculate. This of course limits the complexity of the cases we can consider for now, but hopefully allows greater physical insights into the issue of modal coherence.

Until now, we have not discussed the form of the sound speed correlation, C. Recall that the two depth integrals go from sea surface well into the seafloor. Since these two regions behave statistically independently of one another (assuming the deterministic background has been properly subtracted), the correlation function may be separated as a function of depth as follows:

$$C(X, x, z_1, z_2) = \begin{cases} C_{bottom} & z_1, z_2 > H \\ C_{water} & z_1, z_2 < H \\ 0 & \text{otherwise.} \end{cases} \tag{6.16}$$

This gives (for isotropic, homogeneous and range-independent environment),

$$\begin{aligned} \langle \Delta\theta_1 \Delta\theta_2 \rangle \;=\; & \iint_0^R \iint_0^H dx dX dz_1 dz_2 G_m(z_1) G_m(z_2) C_w(X, x, z_1, z_2) + \\ & \iint_0^R \iint_H^\infty dx dX dz_1 dz_2 G_m(z_1) G_m(z_2) C_b(X, x, z_1, z_2) \end{aligned}$$

Even if the bottom and water column are for some reason correlated, a separation similar to that above can still be done, with the addition of a term representing the

cross-correlation between the bottom and water column.

$$\langle \Delta\theta_1 \Delta\theta_2 \rangle = \iint_0^R \left\{ \iint_0^H G_m(z_1) G_m(z_2) C_w + \iint_H^\infty G_m(z_1) G_m(z_2) C_b \right. \\ \left. 2 \int_H^\infty \int_0^H G_m(z_1) G_m(z_2) C_{bw} \right\} \tag{6.17}$$

There is a subtle issue regarding exactly when the averaging, as indicated by the $\langle \cdot \rangle$ is valid. For instance, in (6.17), a term similar to the third term occurs if the propagation range has been insufficient (i.e., on the order of a correlation length) for the mean values to converge to zero (assuming that the process is zero-mean), even if the water column and bottom are uncorrelated. Note, however, that variabilities in the bottom and at the interface are likely to have much shorter correlation scales than the ocean processes (on the order of 1 km versus orders of 10 km), and so for most situations, the elimination of the third term is likely justified.

6.3 PSF Calculations and Examples

In this section we look at a few of the ways in which the modal phase structure function (MPSF) may be applied. Two example calculations are shown.

6.3.1 Mesoscale Variability

Using the data provided by SeaSoar, it is possible to estimate the correlation scales of the thermohaline variability. The example presented here looks at how the mesoscale variability in the region affects the modal phase structure function. Analysis of the horizontal variability of the region from the summer data[1] suggests a horizontal correlation scale of about 10 kilometers in *both* the along-shelf and cross-shelf directions. This unexpected isotropy could possibly be a result of the large amount of mesoscale turbulence associated with the front and front/eddy interactions (G. Gawarkiewicz, personal communication). A simple model, then, of the sound speed correlation is to

[1] There is no reason to expect the winter and spring variability to have the same correlation scale as in the summer.

assume a Gaussian correlation function in the x and y directions, with decorrelation scale of 10 km, and some function for the depth variability that will be determined later.

The simulation environment is a range-independent waveguide of 100 meter water depth. The reference sound speed profile is taken from the summer PRIMER SeaSoar records, averaged over the entire 7-day dataset. Figure 6-2 shows the resulting profile. A 30 m sediment layer is used, with $C_p = 1700$ m/s and $\rho = 1.9$ gm/cm^3, overlying

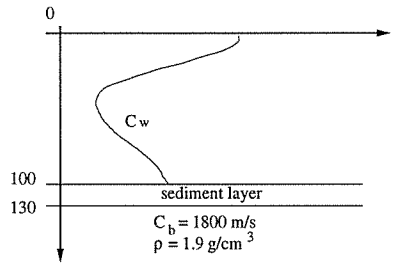

Figure 6-2: Background environment for Example 1.

an acoustic halfspace of nearly the same properties. The kernel, $G_m(z)$, is shown in Figure 6-3 for the first 30 modes at 400 Hz. Note that the functions are positive semi-definite.

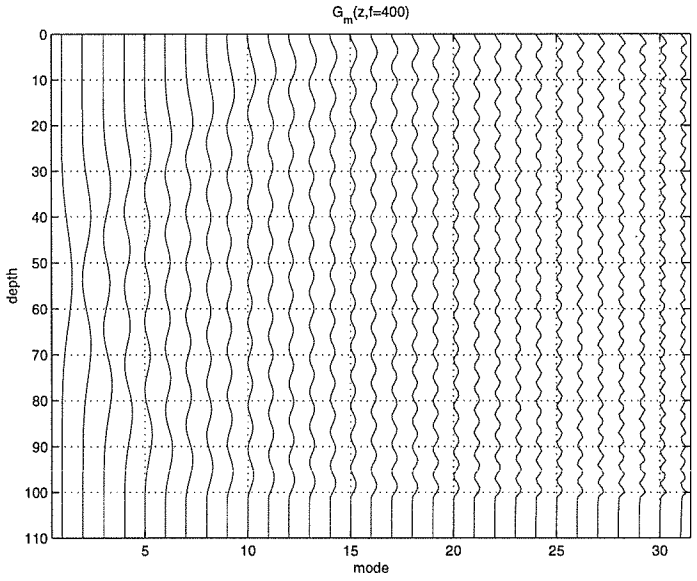

Figure 6-3: Kernel functions.

As mentioned earlier, the medium is assumed to be isotropic, with a Gaussian cor-

relation function of the sound speed based on the SeaSoar temperature and salinity records. While this does not necessarily completely reflect what the actual oceanography is doing (i.e., vertical water motion versus horizontal advection), it is a good enough proxy for current purposes. Recalling the simplified propagation geometry discussed in the prior section, the adopted correlation function within the water column becomes:

$$\begin{aligned} C_w(x, X, z_1, z_2) &= e^{\frac{-x^2}{2L_x^2}} e^{\frac{-y(X)^2}{2L_y^2}} W(z_1)W(z_2) \\ &= e^{\frac{-(x^2+(2\Delta y/R)^2 X^2)}{2L^2}} W(z_1)W(z_2)\,. \end{aligned} \tag{6.18}$$

The depth function $W(z)$ in this example is based on an EOF decomposition of the sound speed cross-correlation matrix. Figure 6-4 shows the first ten sound speed perturbation EOFs and their cumulative contributions to the total variance. Only the first three are retained for the example.

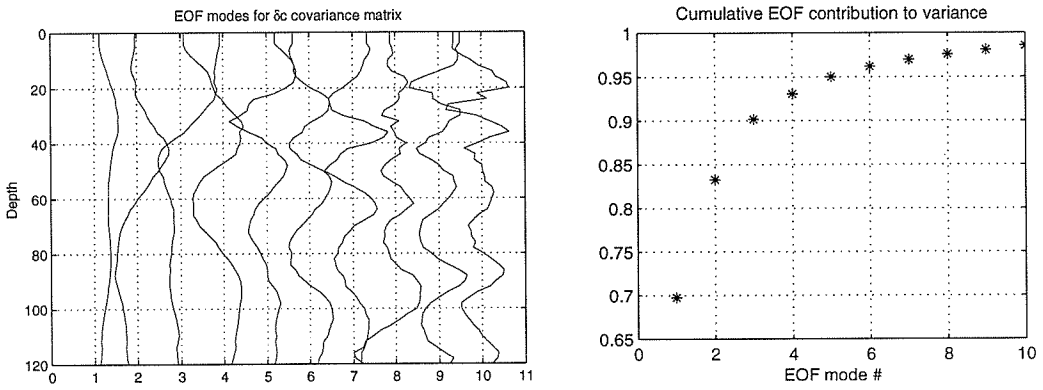

(a) First ten sound speed perturbation EOFs.

(b) Cumulative EOF variances.

Figure 6-4: Empirical Orthogonal Function (EOF) expansion of the sound speed perturbation cross-correlation matrix.

The next step is to substitute the correlation function of (6.18) into the expressions for auto- and cross-correlations. Looking first at just the range integrals for the cross

terms, one has:

$$\iint_0^R dx\, dX\, C_w(x, X, z_1, z_2) = A \iint_0^R dx\, dX\, e^{\frac{-(x^2+(2\Delta y/R)^2 X^2)}{2L^2}} W(z_1)W(z_2)\,. \quad (6.19)$$

Letting

$$\gamma = \tfrac{x}{\sqrt{2}L} \quad \text{and} \quad \Gamma = \tfrac{2\Delta y}{\sqrt{2}RL} X\,, \quad (6.20)$$

(6.19) becomes

$$\begin{aligned} & A\left(\sqrt{2}L \int_0^{R/\sqrt{2}L} e^{\gamma^2} d\gamma\right)\left(\frac{RL}{\sqrt{2}\Delta y} \int_0^{\sqrt{2}\Delta y/L} e^{\Gamma^2} d\Gamma\right) \\ = \; & A\left(\sqrt{2}L \frac{\sqrt{\pi}}{2} \text{erf}\left(\tfrac{R}{\sqrt{2}L}\right)\right)\left(\frac{RL\sqrt{pi}}{2\sqrt{2}\Delta y} \text{erf}\left(\tfrac{R}{\sqrt{2}L}\right)\right) \\ = \; & A\frac{\pi RL^2}{4\Delta y} \text{erf}\left(\tfrac{R}{\sqrt{2}L}\right) \text{erf}\left(\tfrac{\sqrt{2}\Delta y}{L}\right) \\ \approx \; & A\frac{\pi RL^2}{4\Delta y} \text{erf}\left(\tfrac{\sqrt{2}\Delta y}{L}\right)\,, \end{aligned}$$

where A is a normalization factor that scales the modeled variance at a reference depth to be a particular value as measured from the SeaSoar data. In this case, the sound speed perturbation variance at 40 meters was set to 120 $(\text{m/s})^2$. The final equality comes from the fact that the error function, for arguments much greater than one, tends to one itself. A similar procedure is followed for the $\langle \theta_i \theta_i \rangle$ terms, which yields:

$$\begin{aligned} \iint_0^R dx\, dX\, C_w(x, X, z_1, z_2) &= A \iint_0^R dx\, dX\, e^{\frac{-(x^2+(\Delta y/R)^2 x^2)}{2L^2}} W(z_1)W(z_2) \\ &= A\sqrt{\frac{\pi}{2}} RL \end{aligned}$$

The final expression, then, for the phase structure function is:

$$\langle\theta_1\theta_1\rangle + \langle\theta_2\theta_2\rangle - 2\langle\theta_1\theta_2\rangle =$$
$$2A\left(\sqrt{\frac{\pi}{2}}RL - \frac{\pi RL^2}{4\Delta y}\mathrm{erf}\left(\frac{\sqrt{2}\Delta y}{L}\right)\right)\iint_0^H dz_1\,dz_2\,G_m(z_1)G_m(z_2)W(z_1)W(z_w)\,.$$

Figure 6-5 shows the resulting modal phase difference function for modes 1–20 at 400 Hz as a function of receiver separation, plotted in units of acoustic wavelength. Several items are worth noting. The shape of each curve is that of the error function, and the relative amplitudes are controlled by the projection of $W(z)$ onto the kernel function, G_m. These can be seen by noting that for a fixed mode number and frequency, the depth integral is a constant, leaving only the range integral contribution (which has the form of an error function) to vary with receiver separation. A rule of thumb for acceptable phase coherence between two points is that the phase differs by less than $\pi/4$. Taking the square ($(\pi/4)^2 \approx 0.6$), one sees that at 20 wavelengths (75 meters), only modes 1 and 2 are close to being "coherent." Recall that experimental measurements suggest 30λ as being the maximum coherence length in shallow water. A very important point that this figure does not convey is the high sensitivity of the phase structure function to the depth-structure of $C_{\delta c}$. Before carrying out comparisons between coherence limits (theoretical or experimental), one should really establish a common environment. Also, one must be careful comparing this mode-by-mode coherence with the total (full field) coherence.

The same calculations may be done for a variety of frequencies and a fixed receiver separation. This is illustrated in Figure 6-6. As frequency increases, the higher modes, which are initially all surface-interacting, begin turning below the surface. This is evidenced by the sharp bend in the curves, most noticeable in the high modes.

6.3.2 Incorporation of Sub-bottom Variations

As indicated earlier, it is possible to include the effects of geoacoustic variability in the bottom. For the example used here, the previous range-independent waveguide is used again, with the addition of subbottom perturbations that have Gaussian correlation

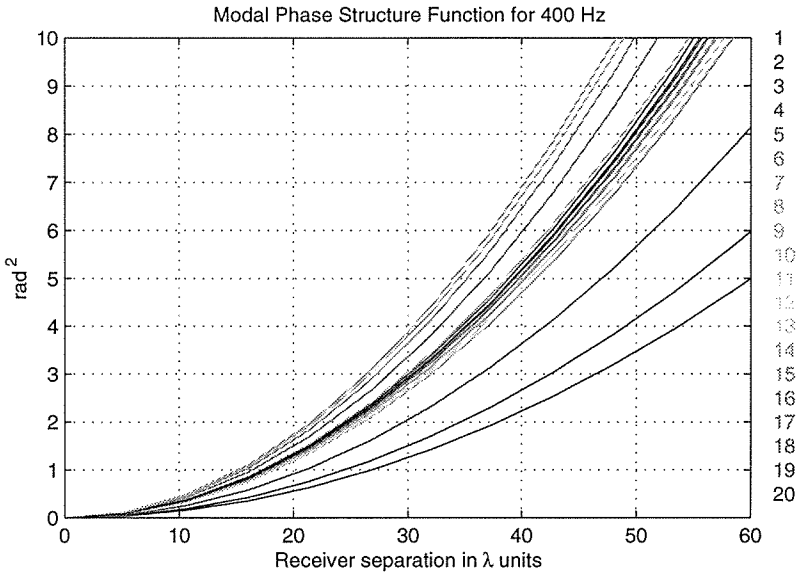

Figure 6-5: Phase difference function for first example case. Modes 1-20 are shown as a function of receiver separation distance, in wavelength, λ.

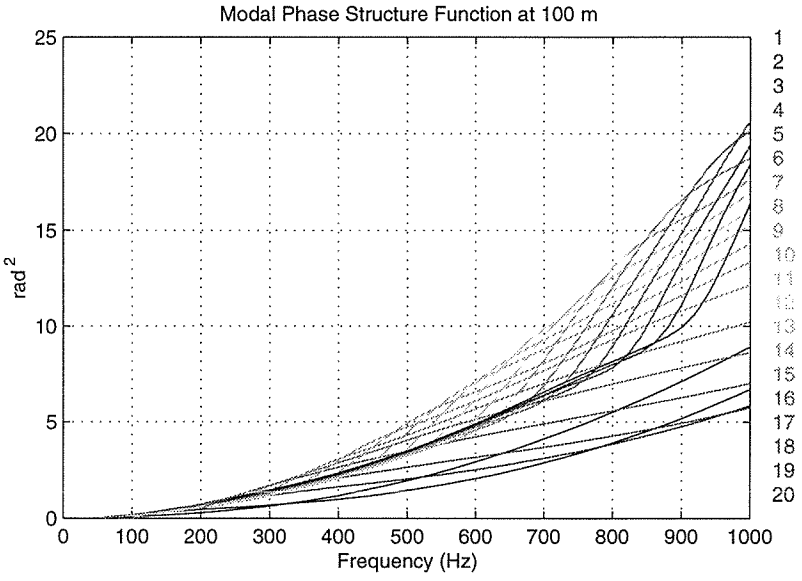

Figure 6-6: Phase difference function versus frequency for modes 1–20. Receiver separation is 100 meters.

functions in the horizontal with 1 kilometer scale lengths and Gaussian correlations in depth with 10 meter scales. Figure 6-7 shows the difference in phase structure functions with and without bottom perturbations. As would be expected, the PSF with bottom variability shows greater RMS phase variation than with water column only. Also, it is the lower frequencies and lower mode numbers that penetrate the bottom the most and therefore show more variability.

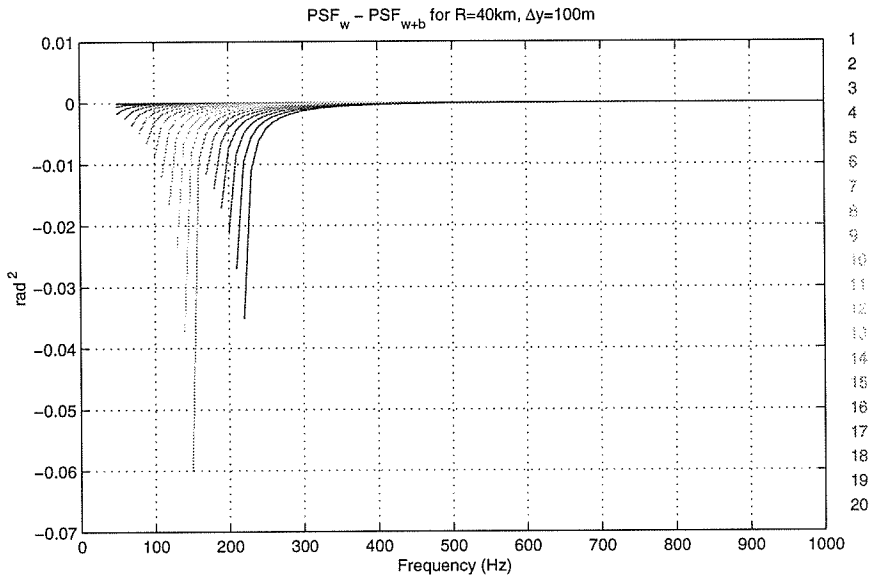

Figure 6-7: Relative effect of adding in bottom structure to the waveguide.

6.3.3 Interface Roughness

A simple and perhaps useful way of incorporating layer roughness in our formulation is as follows. Let us break the depth integrals in a similar fashion to the method outlined earlier, as shown below:

$$\iint_0^\infty dz_1\, dz_2\, C = \iint_0^{H-\epsilon} dz_1\, dz_2\, C_w + \iint_{H-\epsilon}^{H} dz_1\, dz_2\, C_r + \iint_H^\infty dz_1\, dz_2\, C_b\,, \quad (6.21)$$

where ϵ is the RMS roughness value for the interface, and C_r is the roughness correlation function. There is actually a more rigorous approach to interface roughness that still uses perturbation theory. In this case, the modeshape perturbations due to a fluctuating bottom boundary height are allowed (Zhu and Guan, 1992).

6.3.4 Extension to Range-dependent Environments

Assuming that the range-dependence lies only in the x-direction, and that path separation is small,

$$\langle \theta_1 \theta_2 \rangle = \int\int_0^R \int\int_0^H G_m(X, x, z_1) G_m(X, x, z_2) C_w(X, x, z_1, z_2) dz_1 \, dz_2 \, dX \, dx \ . \quad (6.22)$$

If one breaks the environment into piecewise range-independent segments, one can again pull G_m out of the range integrals, and if the bottom varies, H become $H(X)$.

For single mode coherences (e.g., different points in space), this extension is straightforward. The RMS phase terms are summed together for each spatial segment traversed while the energy is in a particular mode. This may be written as the following, where the mode number, $m(j)$, has become a function of the segment number,

$$\Delta\theta_m = \sum_j \Delta\theta_{m(j)} \ . \quad (6.23)$$

The actual mode coupling between segments only affects the magnitude. More complicated scenarios can also be considered, for instance, the coherence between modes arriving within a certain time window, but having traversed any number of different paths through mode space to get to the receivers.

6.4 Summary

In this chapter, a new technique for analyzing modal coherences has been presented, the so-called modal "phase structure function" (PSF). Using first-order perturbation theory, it was shown that the modal phase structure function could easily be expressed in terms of environmental correlation functions. The modal PSF may be related to the full-field coherence by noting that the latter may be written as a summation over mode numbers involving a series of phase differences. The modal PSF is nothing more than the mean square of a given phase difference. Studying the RMS behavior of the

individual phase differences by means of the modal phase structure function should shed light on the behavior of the full-field coherence. A few examples were given to illustrate how the phase structure function might be applied to various situations.

Chapter 7

Summary

The primary focus of this thesis has been on characterizing acoustic propagation in the region of the continental shelfbreak. Results from both an acoustic modeling study and analysis of acoustic and oceanographic data collected during the Summer 1996 Shelfbreak PRIMER Experiment have been combined to provide a better understanding of the complexities of the propagation. Because of the high levels of acoustic mode coupling encountered, one of the experimental objectives, the inversion of the acoustic data in a tomographic sense, was not achievable. Instead, after considering two simplified inverses, attention was re-directed toward a promising method of analyzing horizontal coherences on a mode-by-mode basis in shallow water. The first section that follows summarizes the important conclusions that may be drawn from the work presented in this thesis. Partially overlapping with the first, the second section details those results and findings that represent new and important contributions. Lastly, the third section looks ahead and discusses the work remaining to be done in this particular area of acoustical oceanography and ocean acoustics.

7.1 Conclusions

The conclusions reached in this thesis may be grouped into three categories: propagation modeling, data analysis/simple inversions and theoretical coherence calculations.

7.1.1 Propagation Modeling

The following conclusions may be drawn from the modeling study of Chapter 4:

1. Given the PRIMER source locations, there could be no direct excitation of the lowest 4 or 5 modes. Energy received in those modes, therefore, had to arrive there via mode coupling.

2. Three primary mechanisms for causing mode coupling were identified: the bathymetry, the shelfbreak front and the soliton field, listed in order of increasing importance. Only the latter two mechanisms are able to couple energy into the lowest mode number.

3. Under adiabatic conditions, the fastest mode arrival is mode 6. The fastest path for energy to travel SE source to NE array is through mode 6 for the first 30 km, and then to couple into mode 1 for the rest of the path. A similar scenario exists for the propagation path from SW source to NE VLA, although it involves more coupling.

4. Downwelling on the on-shore side of the front, possibly due to secondary circulation effects near the front, couples energy directly into the low modes.

5. Mode arrival times and spreads are sensitive functions of how the mode field is excited and where in the propagation path coupling may occur. For each mode not normally excited by the source, the arrival time (or bias) and spread have maximum variability when the coupling occurs at an optimal point along the propagation path, determined by the range-dependence of the modal group velocities.

7.1.2 Data Observations/Simple Inversions

Based on the data observations made in Chapters 3 and 5, the following conclusions can be made:

1. The fastest-arriving mode frequently varies, although more often than not it is one of the first three modes. Based on the modeling results, this suggests that there must be relatively constant supply of mode couplers present within the region.

2. Mode decorrelation times at 400 Hz range from less than 1 minute to more than 4 minutes.

3. The leading edge of SE400 arrivals wanders 130 milliseconds, and can change by as much as 80 milliseconds in half a day. The SW400 arrival times wandered 170 msec. Much of this wander may be traced to thermal variability, as indicated by the agreement with thermistor-based data, as well as by the inversion for range- and depth-averaged temperatures in comparison with SeaSoar.

4. Those parts of the leading edge wander that do not match well with thermistor or SeaSoar data correspond to periods when the mode coupling has likely changed in a substantial fashion.

5. Fluctuations in the signal spread are not as correlated with the local soliton arrivals at the VLA as they were in SWARM, indicating likely coupling events happening further away from the VLA.

6. There is some evidence, though it is not yet complete, that the internal tide strength measurably differs across the 40 km width of the study region.

7.1.3 Mode Coherence Calculations

The primary conclusion to be drawn from Chapter 6 is that the use of the modal phase structure function provides a relatively straightforward method of understanding a key component of the full-field coherence, namely the RMS behavior of phase differentials. With some care, much of the phase structure function may be calculated analytically, providing better insight into the underlying physics. The formulation also allows statistically-independent environmental fluctuations to be treated separately, and the method is readily extendable to a wide variety of situations.

7.2 Original Thesis Contributions

The findings of the Shelfbreak PRIMER Experiment are closely related to those of the SWARM experiment, and as such, many of the contributions of this thesis build upon, or are related to, the findings from the SWARM group, in particular the work done by Headrick (Headrick et al., 1997a,b). It also needs to be clearly stated that the idea of using a modal phase structure function, coupled with the possible splitting of the environmental correlation function, were contributions by my advisor. The subsequent theoretical development, calculations and final presentation of the material were my own, however. The significant and original contributions of this thesis are as follows:

1. This thesis represents the first time that a detailed analysis has been made of acoustic propagation in the region of the shelfbreak front.

2. Through modeling and data analysis, it has been demonstrated that acoustic propagation through the shelfbreak region is dominated by mode coupling, and that the primary mechanism responsible for moving energy from high-order modes at the source location, to low-order modes at the receiver location, is most likely soliton-induced coupling.

3. Two very important propagation characteristics of the region result from strong variations in mode velocity with range: (1) the fastest path from source to receiver is through a higher mode over the slope, transitioning to the lowest mode over the shelf; (2) as a result of the above, mode coupling away from receiver can cause large fluctuations in signal spread and wander.

4. Combining thermistor and acoustic data in a non-linear parametric inversion as a means of estimating the spatial and temporal structure of the internal tide strength.

5. Demonstration of the usefulness of the modal phase structure function.

7.3 Directions for Future Work

7.3.1 Analysis and Modeling

In terms of data analysis, the Winter PRIMER acoustic data remain to be analyzed in detail. With the existence of three seasons of SeaSoar data, a seasonal catologuing of acoustic propagation characteristics (based on propagation modeling) would be quite interesting and useful in planning any sort of future field work in the area. Also, the characteristics of multi-frequency propagation have not yet been explored, and the entire set of acoustic arrivals from all propagation paths remains to be analyzed as a whole.

7.3.2 Coherence

As mentioned in Chapter 6, the work presented here in the thesis represents the initial step in exploring what should be a very useful analysis tool for understanding mode coherences in shallow water. Areas of particular interest to cover in the future include: cross-frequency and cross-modal calculations, an extension to range-dependent environments with both adiabatic and coupled-mode propagation, the inclusion of interface roughness and the incorporation of actual measurement-based subbottom correlation data.

7.3.3 Experimentation

Based on what has been learned throughout the course of this thesis work, there are several ways one might modify future experiments in similar regions.

- A towed source offers many advantages in a region as complex and dynamic as the continental shelfbreak. One can transmit from shallower depths, thus directly exciting the low acoustic modes. Simulations show that, at least in the absence of soliton coupling, the lowest modes can travel upslope and through the front nearly adiabatically. A towed source may be moved as needed to account for unexpected variations in front location, such as those forced by eddies or

shelf water meanders. These advantages need to be weighed against the extra ship time and increased logistics involved in source towing, as well as space-time aliasing.

- A towed array, as well as a fixed horizontal array, for measuring horizontal coherence would provide valuable data to compare with theoretical calculations for the region.

- Shortening the distance between source and receiver could eliminate the presence of multiple soliton packets along propagation path. This could potentially open avenues for acoustic-based estimation of soliton and solibore parameters.

- Along the lines of wishful thinking and unlimited budgets, having vertical arrays with greater apertures would improve mode resolution, and more ADCPs and thermistors would enable better sampling of the oceanography for propagation modeling.

Appendix A

Array Navigation

Motion of the two hydrophone arrays deployed during the PRIMER experiments was tracked by means of acoustic navigation. With this method, the length of time required for an acoustic pulse to travel between two points in space is proportional to the distance between them, and with judicious placement of transmitters and receivers, the motion of a sensor array may be accurately tracked.

A.1 Deployment Configuration

The northeast vertical array (NE VLA) was equipped with two independent navigation systems, both utilizing the same baseline array of three Benthos Expendable XT6000 transponders deployed in a triangular fashion about the vertical array. The first system (referred to here as VLA NAV) used four of the tomographic hydrophones (No.'s 1,7,12 and 16), and a pinger located on the electronics sled at the base of the VLA (refer to Figure 3-2, on page 49). The circuits for the four hydrophones were modified to capture the high-frequency navigation signals. The second navigation system, a WHOI Navigator unit, was placed near the top of the array and functioned independently of the VLA NAV system. The three transponder units listened at 10 kHz and responded at 11.0, 11.5 and 12.0 kHz, respectively. Figure A-1 illustrates the navigation geometry. The transponders were intentionally placed non-equidistant from the VLA to avoid simultaneous arrivals.

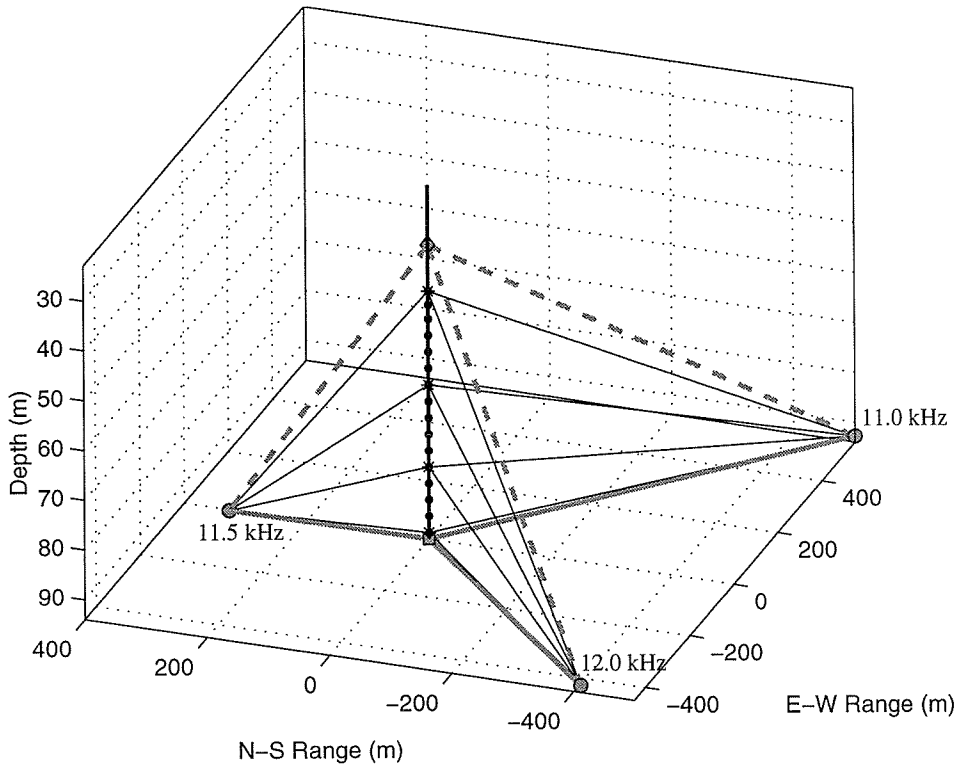

Figure A-1: Navigation configuration for the NE VLA. Thick dashed lines are paths from WHOI Navigator to transponders. Thin solid lines connect navigation hydrophones with transponders, and the thick solid lines along the bottom connect pinger to transponders.

Every four minutes the VLA NAV electronics would generate a clock pulse that simultaneously initiated on-board timers for the four NAV channels and also elicited a 10kHz pulse from the pinger. The transponders would then reply upon receiving the 10kHz signal. Timers on board the VLA logged the arrival times of each transponder signal, measured relative to the initiating clock pulse. The WHOI NAV system was less circuitous. It was clocked every 5 minutes, and the round trip time to and from the navigator unit to the transponders was recorded. Table A.1 details the frequencies and deployment locations of the various components of the NE VLA navigation.

	Dropped		Surveyed		
Transponder	Lat	Lon	Lat	Lon	Depth
anchor	40° 22.589′	−70° 40.197′	—	—	95
11.0kHz	40° 22.324′	−70° 39.889′	40° 22.3422′	−70° 40.1970′	95
11.5kHz	40° 22.764′	−70° 40.199′	40° 22.7952′	−70° 40.1787′	95
12.0kHz	40° 22.372′	−70° 40.427′	40° 22.3656′	−70° 40.4415′	95

Table A.1: NE VLA navigation coordinates. A bottom depth of 95 meters is assumed.

For the most part, the navigation data was of good quality, with two notable exceptions involving the 11.0 kHz data (the eastern-most transponder). In the VLA NAV records, the variance of the 11.0 kHz data is much higher than that of the other two transponders. Also, for some as-yet unexplained reason, the WHOI navigator failed to capture any of the 11.0 kHz arrivals. Figure A-2 shows the raw[1] data from the VLA NAV system. Variations between hydrophones, for a given transponder, are slight. There are significant differences, though, between the three transponder arrivals. As will be shown later, most of this variability is due to fluctuating oceanography as opposed to actual array motion.

A.2 Hydrodynamic Predictions

It is useful to have an estimate of the mooring motion magnitude expected for a given deployment. To obtain a prediction for the mooring displacement, the Shark

[1]Not entirely raw, as numerous spikes and other glitches have been removed.

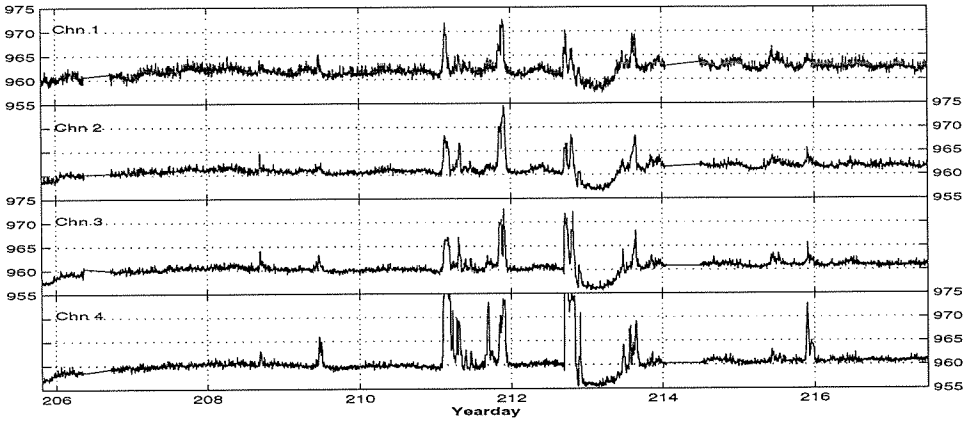

(a) 11.0kHz

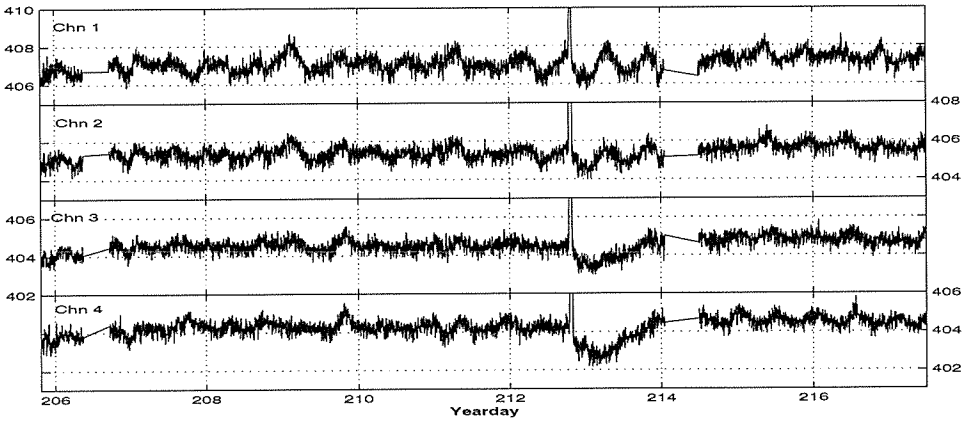

(b) 11.5kHz

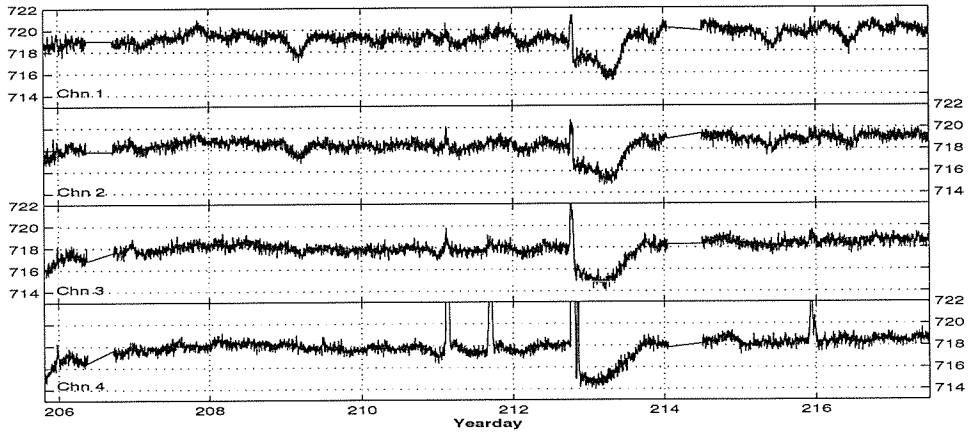

(c) 12.0kHz

Figure A-2: Raw data for the VLA NAV system. Note that the dynamic range of the plots differs between the transponders.

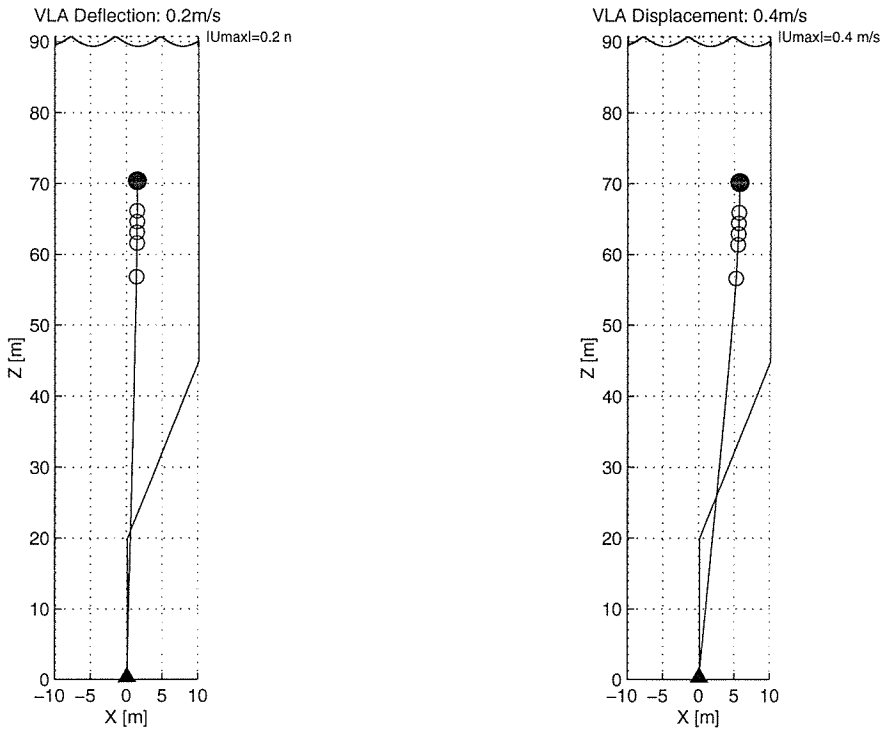

(a) 20 cm/s current field.

(b) 40 cm/s current field.

Figure A-3: Modeled VLA displacements for various current magnitudes.

VLA mooring was entered into the Mooring Design and Dynamics program, written by R. Dewey of Univ. Victoria (Dewey, 1998). While the program was created to aid in the design and deployment of moorings, one of the fundamental tasks of the code is to estimate array motion under a variety of current conditions. Each element of the mooring was specified, including the exact weight, buoyancy and geometry of each component. A simple current model was used, with uniform flow over the upper 45 meters, tapering to zero over the next 10 meters in depth. Since the northern moorings were positioned well away from the frontal jet, typical maximum currents were expected to range from 10 to 20 cm/s. Two cases are considered here, a 20 cm/s current and a very unlikely, 40 cm/s. Figure A-3 shows the model results. The maximum deflection for the 20 cm/s current, at the upper hydrophone depth of 45 meters, is around 1 meter. At 40 cm/s, the deflection increases to about 4.5 meters.

A.3 Inverting the VLA NAV data

There are numerous methods of obtaining array motion from the acoustic travel time data provided by the navigation systems. Most often, some form of a least squares inverse is utilized to minimize what is most often an over-constrained problem. We follow the Gauss-Markov formulation, which is equivalent to a weighted, or tapered, least squares where the weighting matrices are chosen according to a priori statistics. This provides the best linear, unbiased estimator (Wunsch, 1996). With all four navigation hydrophones providing usable data from three well-positioned transponders, there is the somewhat unique opportunity to use all of the data to reduce the variances of the position estimates.

Given the large amount of tension in the array, it is reasonable to assume that the array behaves as a rigid staff and does not undergo any deformation. This assumption has the advantage of constraining the possible relative motions of each hydrophone element. In fact, the rigid array assumption forces the individual hydrophone displacements to be fully-dependent, reducing the problem to 12 data measurement points (14 including the 2 usable WHOI NAV channels) with only three unknowns (i.e., the x, y and z displacements of the array tip). Lest the degree to which the problem is over constrained seems too good to be true, it should be noted that one could conceivably add in 6 more unknowns to represent the transponder locations, and 3×4 more unknowns to account for sound speed variations along each acoustic path!

The first step is to develop a model relationship between the travel time and various physical parameters. First of all, we can express the range between points i and j as

$$R_i^j = ||(\mathbf{x}_i - \mathbf{x}^j)|| = \sqrt{(x_i - x^j)^2 + (y_i - y^j)^2 + (z_i - z^j)^2}\,. \tag{A.1}$$

The round trip travel time recorded at hydrophone i, from transponder m, may then

be written as:

$$\tau_m^i = S_0^m R_0^m + S_m^i R_m^i + \tau_{ta} + \tau_r + \delta s_m^0 + \delta s_m^i + \epsilon_r + \epsilon_{ta} + n\,, \tag{A.2}$$

where,

$$\begin{aligned} S_i^j &= \text{mean sound speed slowness between points } i \text{ and } j \\ \tau_{ta},\, \epsilon_{ta} &= \text{turn-around time (and error) at a transponder} \\ \tau_r,\, \epsilon_r &= \text{pulse recognition time (and error) at receiver} \\ \delta s_m^i &= \text{error slowness estimate along path} \\ n &= \text{noise} \end{aligned}$$

For the time being, we will keep only the first two terms on the right hand side of (A.2). The left hand side is the measured navigation data, and it is assumed that S is known for each path, and the only unknown is the location of the receiving element relative to the transponder. The relationship between the positions x, y, z and the travel time is a non-linear one. Given an initial guess for the element positions, a logical first step is to linearize the problem about the initial guess, $R_m^{i(0)}$, using a Taylor Series expansion:

$$R_o^m = R_m^{i(0)} - \Delta\mathbf{x} \cdot \left.\frac{\partial R_m^i}{\partial \mathbf{x}^i}\right|_{R_m^{i(0)}} + \frac{\Delta\mathbf{x}^2}{2} \cdot \left.\frac{\partial^2 R_m^i}{\partial (\mathbf{x}^i)^2}\right|_{R_m^{i(0)}} + \ldots\,, \tag{A.3}$$

where the derivative is given by,

$$\frac{\partial R_m^i}{\partial \mathbf{x}^i} = \frac{\partial R_m^i}{\partial (x^i, y^i, z^i)} = \frac{-(x^i, y^i, z^i)}{(R_m^i)^2}\,. \tag{A.4}$$

We now have a linear relationship between Δx and the measured travel times,

$$\tau_i^j - SR_i^{j(0)} = \Delta\tau_i^j = \frac{\partial R_m^i}{\partial \mathbf{x}^i} \cdot \Delta\mathbf{x}\,. \tag{A.5}$$

The coordinates $\mathbf{x}^j = (x^j, y^j, z^j)$ and $\mathbf{x}_i = (x_i, y_i, z_i)$ are relative to the anchor position on the seabed, and S represents an appropriate sound slowness between the two points. Later on this issue will be dealt with in some detail.

Now assume that $\mathbf{x}^j$ represents the location of transponder j and $\mathbf{x}^i$ represents

the location of hydrophone i. Also, let $\mathbf{x}^{i(0)}$ represent the initial guess as to the hydrophone location. A good guess is the location of the phone were the array not tilted in any manner, $(0, 0, z_i)$. Next, let $\Delta\mathbf{x}^i$ represent the perturbation from the nominal position. This is what will be inverted for, and one may relate the travel time, τ, in a linear fashion, to the unknown perturbation.

A.3.1 Positioning Using One-Way Travel Times

The data recorded by the VLA NAV system represent the travel times from pinger to transponder to hydrophone. The pinger-to-transponder path length remains constant, and thus does not contribute to array motion. In fact, it introduces a source of error in the measurements, as fluctuations in sound speed along the pinger-to-transponder path may be confused with array motion. Fortunately, the lower-most hydrophone is less than a meter away from the pinger. Therefore the round-trip times recorded from the lower phone (NAV phone #4) may be used to remove the pinger-to-transponder paths from the other NAV data. If $\tilde{T}_m^i$ represents the round trip time from pinger to transponder m to phone i, the adjusted time may be written as:

$$T_m^i = (T_m^p + T_m^i) - \frac{1}{2}(T_m^p + T_m^4) \approx (T_m^p + T_m^i) - \frac{1}{2}(2T_m^p) = T_m^i \,. \tag{A.6}$$

Equation (A.6) may be modeled via

$$\tau_m^i = S_i^m R_i^m + \frac{\tau_{ta}}{2} + \frac{\tau_r}{2} + \delta s_m + \frac{\epsilon_r}{2} + \frac{\epsilon_{ta}}{2} + n \,, \tag{A.7}$$

This approach may be followed for each phone/transponder combination, and either the absolute position or just the locations relative to the anchor, may be solved for at each time step. Given, though, that we are mainly interested in the positions relative to the pinger, a slightly different difference may be used that can significantly decrease the errors. That is what is sometimes referred to as the single-difference formulation.

A.3.2 Positioning Using Single-Differences

The single-difference method is often used in differential GPS navigation, where paths from two receivers to a single satellite are differenced (Hofmann-Wellenhof et al., 1994). The benefit of a single-difference formulation is that it reduces the sensitivity to errors in the estimates of the anchor and transponder positions. By subtracting the total round trip time of the pinger-transponder-phone #4 path from the other data paths, one is left with a measurement that depends solely on the relative positions of the hydrophones with respect to one another, and not on absolute positions nor on any delays due to on-board electronics. There is also the advantage that the error due to fluctuating sound speed along to the paths associated with a particular transponder is minimized. If the fluctuations are of equal strength along all four paths from a given transponder, then the fluctuation-induced error is completely removed. Otherwise, the magnitude of the error is proportional only to the sound speed differences between paths.

Mathematically, the single-difference is expressed as

$$T_i^j = \tilde{T}_i^j - \tilde{T}_4^j \,, \tag{A.8}$$

or in matrix form as

$$T = C_{sd} \cdot \tilde{T} \,, \tag{A.9}$$

where the difference matrix C_{sd} is a 9×12 matrix given by

$$C_{sd} = \begin{bmatrix} 1 & 0 & 0 & -1 & 0 & 0 & 0 & 0 & \cdots & 0 \\ 0 & 1 & 0 & -1 & 0 & 0 & 0 & 0 & \cdots & 0 \\ 0 & 0 & 1 & -1 & 0 & 0 & 0 & 0 & \cdots & 0 \\ & & & & \vdots & & & & & \\ 0 & 0 & 0 & 0 & \cdots & 0 & 0 & 1 & 0 & -1 \\ 0 & 0 & 0 & 0 & \cdots & 0 & 0 & 0 & 1 & -1 \end{bmatrix} \tag{A.10}$$

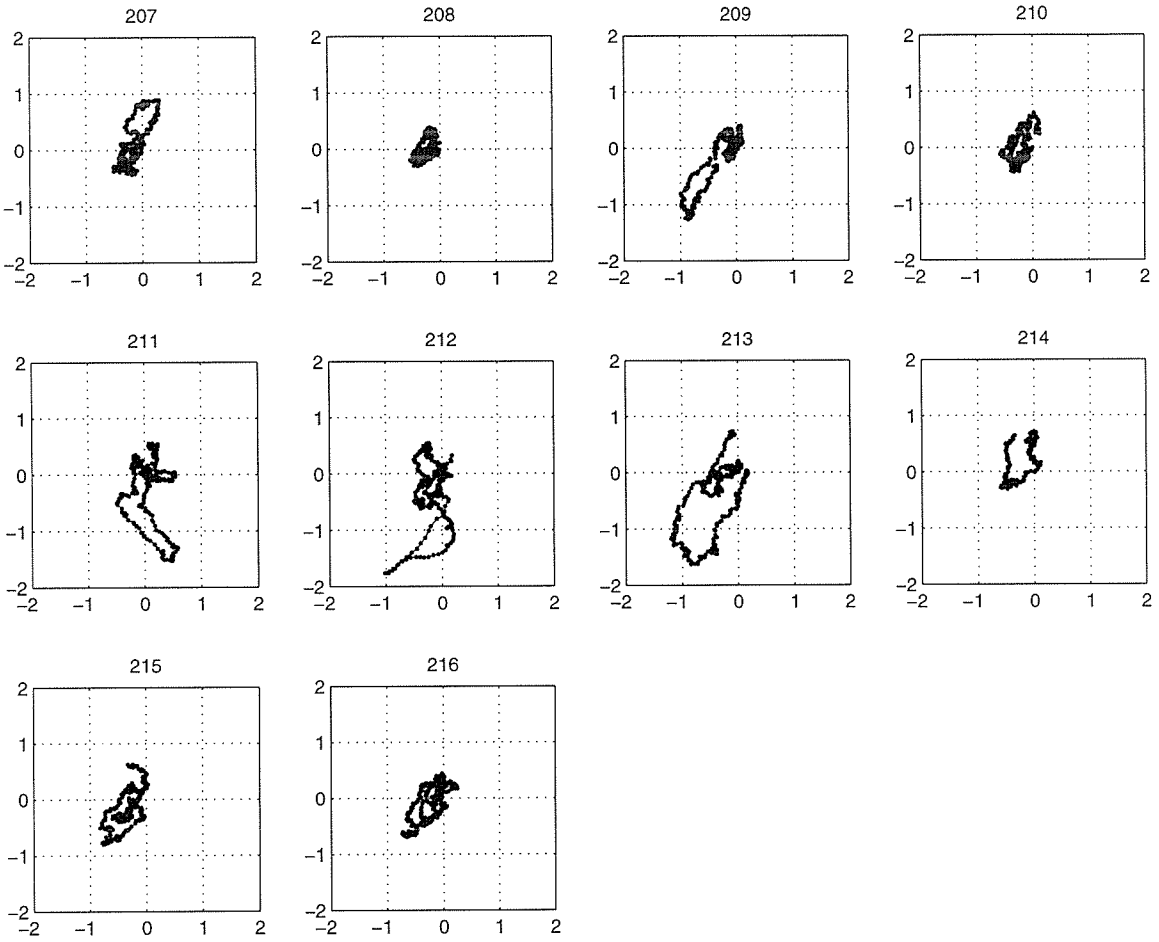

Figure A-4: Estimates motion of the array at uppermost hydrophone element (nominally 50 meters of water).

$$\begin{aligned} \tau_m^{i4} &= \tau_m^i - \tau_m^4 \\ &= S_i^m R_i^m - S_4^m R_4^m + \epsilon_s + \frac{\epsilon_r}{2} + n\,, \end{aligned}$$

Figure A-4 shows the results of inverting for the motion of the upper-most hydrophone on the VLA, plotted for each day. The ellipses traced out are all in agreement with the local tidal ellipses. The majority of the motion is all less than one meter, in keeping with the original design specifications of the mooring.

Appendix B

Summary of Acoustic Receptions

The northeast vertical array ("shark" array) recorded over eleven days of continuous data without gaps or missing channels. A careful review of all the recorded acoustic receptions was conducted with the purpose of identifying transmissions that were either missing or rendered unusable because of noise contamination. The following table summarizes the findings. Each entry in the table corresponds to one of the datafiles in which a noise source was noted. Each datafile nominally covers a two-hour time period. In some of entries in the table, the times associated with a particular noise event are given in parentheses.

Datafile	Description
07231633	ker-splash...VLA goes overboard; *R/V Endeavor* noise
07231830	*Endeavor* survey legs...really noisy
07231954	*Endeavor* goes away; good data begins 2030; ship (2142-2151)
07232349	big ship (0000-0100)
07240553	ship (0724-0736)
07240751	ship (0936-0948); jams 07250945 transmission
07240948	ship (0936-1012); jams 07250950 transmission
07241716	ship (1716-1736)
07242111	ship (2124-2132); strong tones @ 350 and 480 Hz
07242309	trawl noise(?) (2312-2330); more tones @ 350 and 480 Hz
07250106	ship (0212-0306)
07250635	ship (0724-0800); several tonals up to 240 Hz
07251623	ship (1724-1812)
07251955	loud ship (1955-2018); jams 07252000-07250015; other funny noises
07260147	ship (0147-0212); jams 07260145-07260215
07260739	strong ship noise < 100 Hz
07270623	tone @ ≈ 20 Hz that wobbles around
07280113	missing SE400 transmission @ 0220
07280311	ship
07280508	ship
07281100	ship
07281258	ship
07281630	ship
07282025	ship (2206-2230); jams 07282215 & 07282220

Datafile	Description
07290548	slow ship (0624-0745)
07291008	ship (1012-1042); jams transmissions 07291015-07291035
07291206	ship
07291910	ship
07301027	ship (1048-1112); jams 07301100 & 07301105
07301224	ship (1406-1418); very fast; funny jumps & skips
07301421	ship (1524-1600); SUS; jams 07301535 & 07301545
07302148	ship (2218-2236); SUS; weird stuff, esp. @ 2220
07302346	lots of SUS
07310143	a few SUS
07310341	distant ship (0512-0536)
07310910	ship (0912-0936); may jam 07310915—07310935
07311108	increased noise levels 100-600 Hz till 1200; SUS?
07311700	low-frequency ship noise (1836-1854)
08010027	ship (0030-0054); strong ship tones < 100 Hz
08010620	ship (slow) (0724-0817)
08010817	2 ships (0817-0830) & (0954-1015); more noise 0-600 Hz
08011351	ship (close!) (1418-1506); jams 08011430 and nearby 224 Hz
08011746	ship - very broad
08012141	mess of distant ships; higher noise levels up to 600 Hz
08012338	mess of distant ships; higher noise levels up to 600 Hz
08020507	ship (0530-0606); may affect some 224 Hz
08020902	strong ship (1000-1100); may affect 08021015; bkgrnd noise
08021100	ships?; very strong 200 Hz tone (10 Hz BW) begins 1130
08021257	strong ship (1257-1330); 200 Hz tone ends @ 1400
08030217	ship (0330-0351)
08030351	ship noise (0351-0430)
08031141	ship (1300-1400)
08031710	missing SE400 transmission @ 1820
08040607	lots of tones

Appendix C

Horizontal Refraction

All of the propagation modeling in this thesis has assumed straight-line propagation. This assumption is in reality an approximation which neglects index of refraction gradients in the cross-track direction. In situations where such gradients are significant, there can be horizontal refraction of the acoustic wavefronts, or in other words, bending of the acoustic energy out of the vertical plane of propagation. In shallow water, both the bathymetry and the strong oceanographic variability can contribute to horizontal refraction. A coastal shelf, or any shoaling bottom, can act as a repulsive barrier, refracting sound back toward the open ocean (Brekhovskikh and Lysanov, 1990). A wavefront obliquely incident upon an ocean front can be refracted in a direction dependent upon the angle of incidence and the sound speed gradient at the front. Considering for a moment the Shelfbreak PRIMER study region, it is not immediately evident whether or not horizontal refraction is significant. The existence of additional multipaths is unlikely, given the relatively short distances, but the total signal coherence can be effected by slight variations in the mode travel paths. The goal of this appendix is to determine the degree of horizontal refraction encountered during the experiment and what impact there is, if any, on the received data.

C.1 Horizontal Rays, Vertical Modes

Weinberg and Burridge (1974) were the first to apply horizontal ray theory to the method of normal modes. The issue has more recently been taken up by Munk and others in regards to the acoustic thermometry problem (Munk et al., 1995). Briefly, solutions to the wave equation are formed such that the depth dependence is expressed in terms of normal modes and the mode coefficients solve the 2-D (in the horizontal plane) eikonal and transport equations. Only the eikonal equation is of interest here, since that is the equation that determines the path over which a mode will travel. If the solution to the Helmholtz equation is written in the form:

$$p(\mathbf{x}) = \sum_n a_n(x,y)\phi_n(z;x,y)\,, \tag{C.1}$$

then, in the WKB approximation, one has for a_n,

$$a_n(x,y) \simeq e^{i\int \mathbf{k_n}\cdot\mathbf{ds}}\,, \tag{C.2}$$

where $\mathbf{k_n}$ and $\mathbf{ds}$ are vector quantities in the 2D horizontal plane. The modeshapes, ϕ_n, are the local modeshapes evaluated along the path determined by the eikonal equation

$$\begin{aligned} \frac{d\mathbf{x_n}}{ds} &= \frac{1}{k_n}\mathbf{k_n} \\ \frac{d\mathbf{k_n}}{ds} &= \nabla_\perp k_n\,, \end{aligned} \tag{C.3}$$

where $\mathbf{x}_n$ is the trajectory for mode n, s the arclength along the path and $k_n = |\mathbf{k_n}|$. This is entirely analogous to the standard 2D raytrace problem (Jensen et al., 1994). It is the gradient of the local wavenumber for a given mode, or, factoring out an ω, the local phase speed, that determines the refraction. For modes that are trapped within the water column, the modal wavenumber, k_n, is equal to the water wavenumber at the turning depths for that mode. Each mode, then, should travel a slightly different path, determined by its local wavenumbers.

C.2 Analysis

Horizontal mode refraction calculations were made for both of the 400 Hz paths leading to the northeast vertical array. Two different environments were considered, the reference sound speed profile discussed earlier (see Figure 4-2 on page 70), and the environment measured on Day 7/31 (see Figure 2-6, on page 32). In both cases, the actual USGS bathymetry is used over the entire PRIMER study region. For the reference environment, the sound velocity profile varies in the cross-shelf direction, but not in the along-shelf direction, where it is held constant.

Figure C-1 shows a detailed look at the bathymetry relative to the mooring locations. The path from SE source to receiver follows a heading of 8.23° (degrees E of N). The isobaths near the SE source are rotated 7–8° clockwise, making the relative angle between the local bathymetry gradient and the acoustic path bearing only 1–2°. Near the SE source, refraction should be toward the deeper water to the east. North of the 140 meter isobath, the local bathymetry gradients are slight, and therefore difficult to discern visually. The path from the SW 400 Hz source has a bearing of 45.5°, and the along-path bathymetry gradients are not as large as on the eastern line.

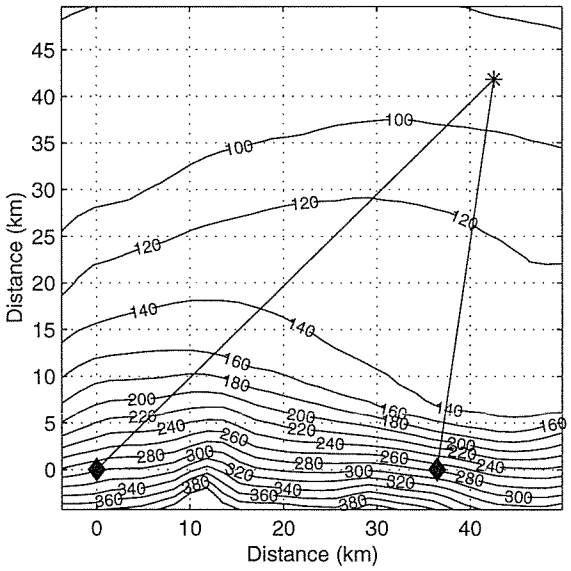

Figure C-1: USGS bathymetry of the eastern Shelfbreak PRIMER region. Contours are in 20 meter increments.

Normal mode phase speeds were calculated over the entire experiment domain, with 1 km spacing in the cross-shelf and 2 km spacing in the along-shelf directions. The phase speeds were then used as the input sound speed field for the raytrace routine, RAY (Bowlin et al., 1992). A range of horizontal launch angles ($\pm 20°$ about the line-of-sight (LOS) path) was searched for potential eigenrays. Only a single eigenray was found for each of the modes considered. Figure C-2 shows the resulting mode paths for the two environments and two source/receiver paths. For the reference propagation case (Figures C-2(a) and C-2(c)), the lowest 2–3 modes make the trip with no refraction at all. There is no bottom interaction for these modes, and the cross-slope variability in phase speeds is slight. The more bottom-interacting higher modes are all refracted to varying degrees toward the right, in accordance with local bathymetric gradients. Although the deflections are as great as 70 meters from the direct path, the total change in path length is no more than one meter in the worst case.

To illustrate the effect that local sound speed gradients can have, Figures C-2(b) and C-2(d) show the refraction on Day 7/31. Most noteworthy are the lower modes, which now experience the greatest refractive effects. With turning points within the water column, these modes are the most susceptible to refraction. The higher modes maintain trajectories that more closely resemble the reference case. It should be mentioned that the 3D environmental information provided by SeaSoar was acquired over a period of 12–15 hours and therefore contains a certain amount of aliasing.

To assess the actual impact of the horizontal refraction, it is necessary to compute the resulting changes in mode travel times. Assuming simple adiabatic propagation, each mode trajectory shown earlier was integrated through the modal group velocity field and the travel times tabulated. This was done for a single frequency, 400 Hz. Figure C-3 shows both the total travel times and the difference in travel times that would result from assuming straight-line propagation from source to receiver for each mode. Even in the worst-case scenario, perturbations are still less than 2 milliseconds. For a 100 Hz bandwidth source, a 2 millisecond change in travel time would theoretically be detectable under adiabatic conditions, and with good signal-to-noise

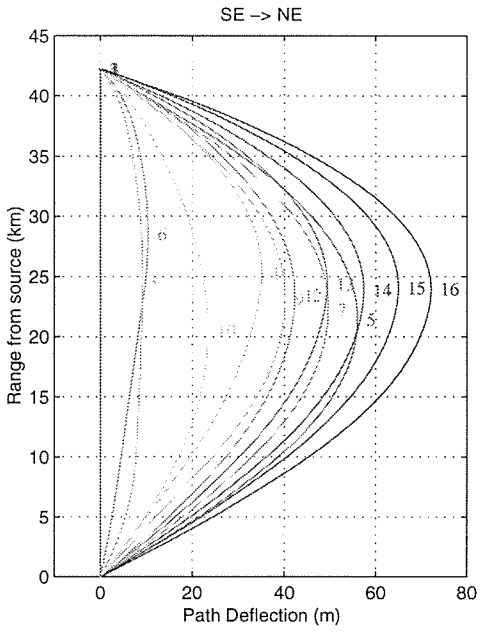

(a) Eastern path; reference

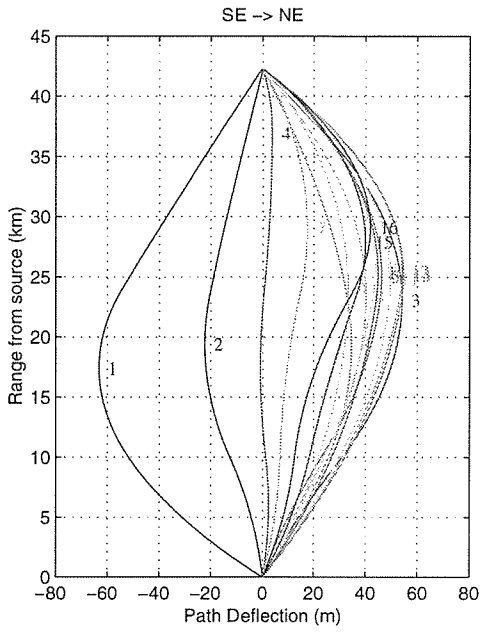

(b) Eastern path; Day 6

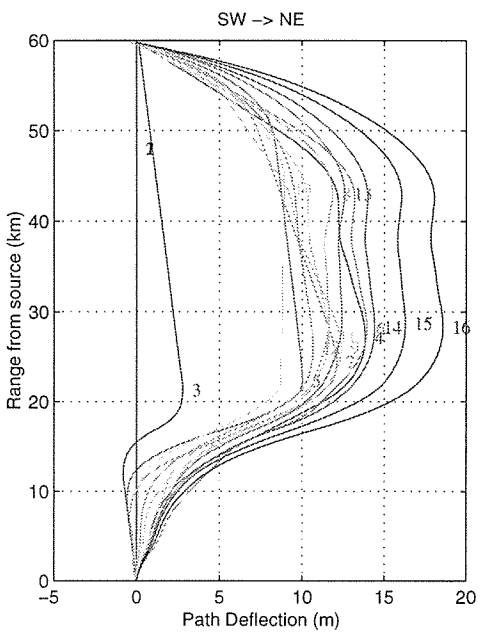

(c) Diagonal path; reference

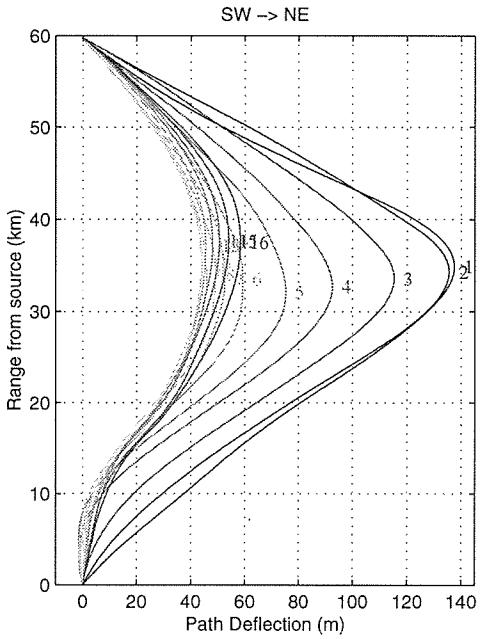

(d) Diagonal path; Day 6

Figure C-2: Horizontal deflection of each mode relative to the direct, source-to-receiver path. Note that the y-axis scales differ between the plots. Calculations are for 400 Hz only.

ratios. However, given the degree of mode coupling present, there is no possibility of resolving such travel-time changes due to variations in the horizontally-refracted paths.

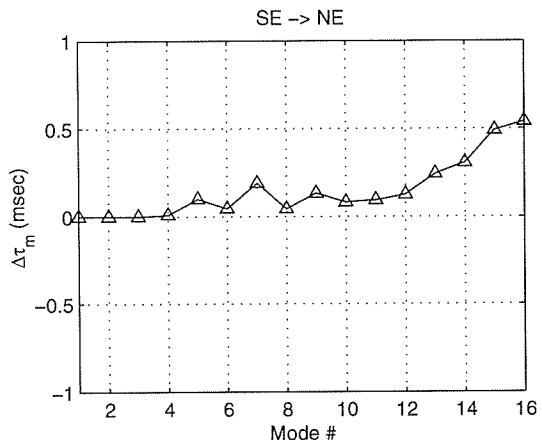

(a) SE source - reference environment.

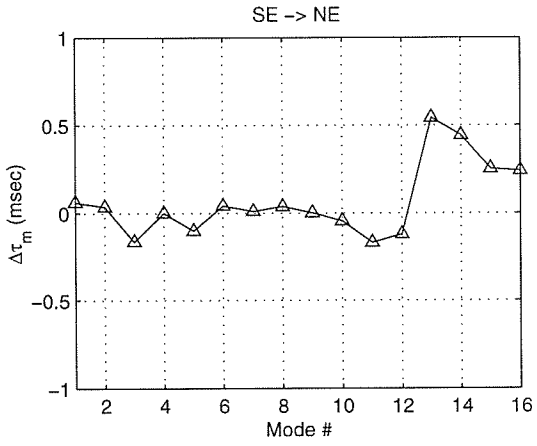

(b) SE source - Day 6 environment.

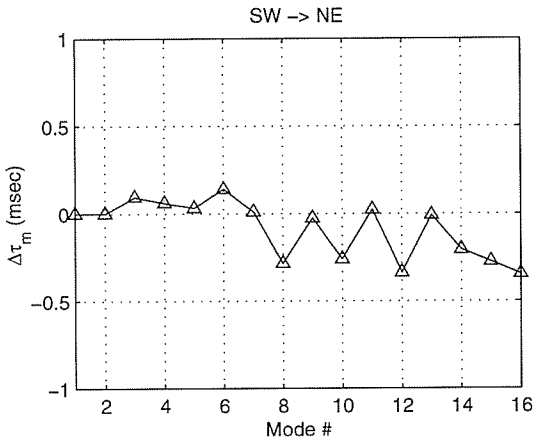

(c) SW source - reference environment.

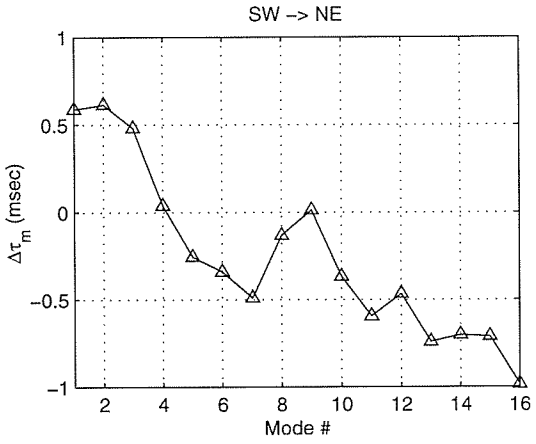

(d) SW source - Day 6 environment.

Figure C-3: Refraction-induced changes in modal travel times.

C.3 Summary

Based on the short survey done in this section, there appear to be no significant travel time effects due to horizontal refraction, consequently straight-line propagation is a reasonable simplification to make. Perhaps the most important item to note

from these calculations is that the modal paths may be separated by over 100 meters horizontally. This could have potential ramifications on cross-modal coherences. Note, too, that the above calculations have ignored the possible effects of mode coupling, though the net result of such coupling, given the relatively short ranges, is not expected to be significant.

Bibliography

Apel, J., Badiey, M., Chiu, C., Finette, S., Headrick, R., Kemp, J., Lynch, J., Newhall, A., Orr, M., Pasewark, B., Tielburger, D., Turgut, A., von der Heydt, K., and Wolf, S. (1997). An overview of the 1995 SWARM Shallow-Water Internal Wave Acoustic Scattering Experiment. *IEEE J. of Oceanic Engineering*, 22(3):465–500.

Apel, J., Ostrovsky, L., and Stepanyants, Y. A. (1995). Internal solitons in the ocean. Technical Report MERCJRA0695, Applied Physics Laboratory: The Johns Hopkins University.

Beardsley, R. C. and Boicourt, W. C. (1981). On estuarine and continental-shelf circulation in the Middle Atlantic Bight. In Warren, B. and Wunsch, C., editors, *Evolution of Physical Oceanography - Scientific Surveys in Honor of Henry Stommel*, chapter 7, pages 198–233. MIT Press, Cambridge, MA.

Beardsley, R. C., Chapman, D. C., Brink, K. H., Ramp, S. H., and Schlitz, R. (1985). The Nantucket Shoals Flux Experiment (NSFE79), I, A basic description of the current and temperature variability. *J. Phys. Oceanogr.*, 15:713–748.

Bowlin, J. B., Spiesberger, J. L., Duda, T. F., and Freitag, L. F. (1992). *Ocean Acoustical Ray-Tracing Software RAY*. Woods Hole Oceanographic Institution.

Brekhovskikh, L. and Lysanov, Y. (1990). *Fundamentals of Ocean Acoustics*. Springer-Verlag, Berlin, second edition.

Buck, J. R., Preisig, J. C., and Wage, K. E. (1998). A unified framework for mode filtering and the maximum a posteriori mode filter. *J. Acoust. Soc. Am.*, 103(4):1813–1824.

Carey, W. M. (1998). The determination of signal coherence length based on signal coherence and gain measurement in deep and shallow water. *J. Acoust. Soc. Am.*, 104(2):831–837.

Chamley, H. (1990). *Sedimentology*. Springer-Verlag.

Chapman, D. C. and Beardsley, R. C. (1989). On the origin of shelf water in the Middle Atlantic Bight. *J. Phys. Oceanogr.*, 19:384–391.

Chiu, C.-S. and Lynch, J. (1987). Tomographic resolution of mesoscale eddies in the marginal ice zone: A preliminary study. *J. Geophys. Res.*, 92(C7):6886–6902.

Chiu, C.-S., Miller, C. W., and Lynch, J. F. (1997). Optimal modal beamforming of bandpass signals using an undersized sparse vertical hydrophone array: Theory and a shallow-water experimentation. *IEEE J. of Oceanic Engineering*, 22(3):522–533.

Chiu, C.-S., Miller, J. H., and Lynch, J. F. (1994). Inverse techniques for coastal acoustic tomography. In Lee, D. and Schultz, M., editors, *Environmental Acoustics*, volume 2, pages 917–931. International Conference on Theoretical and Computational Acoustics.

Clay, C. S. and Medwin, H. (1977). *Acoustical Oceanography: Principles and Applications.* Wiley-Interscience, New York.

Collins, M. D. (1993). A split-step Padé solution for the parabolic equation method. *J. Acoust. Soc. Am.*, 93(4):1736–1742.

Collins, M. D. (1994). User's guide for RAM versions 1.0 and 1.0p. Technical report, Naval Research Laboratory, Washington, D.C. 20375.

Collins, M. D., Fialkowski, L. T., Kuperman, W. A., and Perkins, J. S. (1994). Environmental source tracking. *J. Acoust. Soc. Am.*, 94(6):3335–3341.

Colosi, J. (1998). personal communications.

Colosi, J. A. and Flatté, S. M. (1996). Mode coupling by internal waves for multimegameter acoustic propagation in the ocean. *J. Acoust. Soc. Am.*, 100:3607–3620.

Desaubies, Y., Chiu, C.-S., and Miller, J. H. (1986). Acoustic mode propagation in a range-dependent ocean. *J. Acoust. Soc. Am.*, 80(4):1148–1160.

Dewey, R. K. (1998). *Mooring Design and Dynamics.* Centre for Earth and Ocean Research, Univ. Victoria, Victoria, BC, Canada, version 1.04 edition. URL: http://canuck.seos.uvic.ca/rkd/mooring/moordyn.html.

Esswein, R. and Flatté, S. (1981). Calculation of the phase-structure function density from oceanic internal waves. *J. Acoust. Soc. Am.*, 70(5):1387–1396.

Evans, R. B. (1983). A coupled mode solution for acoustic propagation in a waveguide with stepwise depth variations of a penetrable bottom. *J. Acoust. Soc. Am.*, 74:188–195.

Flatté, S. M., editor (1979). *Sound Transmission Through a Fluctuating Ocean.* Cambridge University Press.

Garfield, N. and Evans, D. L. (1987). Shelf water entrainment by Gulf Stream warm-core rings. *J. Geophys. Res.*, 92(C12):13003–13012.

Garrett, C. and Munk, W. (1972). Space-time scales of internal waves. *Geophys. Fl. Dynam.*, 2:225–264.

Garvine, R., Wong, K.-C., and Gawarkiewicz, G. (1989). Quantitative properties of shelfbreak eddies. *J. Geophys. Res.*, 94:14475–14483.

Gawarkiewicz, G. and Chapman, D. C. (1992). The role of stratification in the formation and maintenance of shelfbreak fronts. *J. Phys. Oceanogr.*, 22:753–772.

Hamilton, E. L. (1980). Geoacoustic modeling of the sea floor. *J. Acoust. Soc. Am.*, 68:1313–1340.

Headrick, R. H. (1997). *Analysis of Internal Wave Induced Mode Coupling Effects on the 1995 SWARM Acoustic Transmissions.* PhD thesis, Massachussetts Institute of Technology/Woods Hole Oceanographic Institution.

Headrick, R. H., Lynch, J. F., and The SWARM Group (1997a). Acoustic normal mode fluctuation statistics in the 1995 SWARM Internal Wave Scattering Experiment. *J. Acoust. Soc. Am.* submitted July 17, 1997.

Headrick, R. H., Lynch, J. F., and The SWARM Group (1997b). Modeling mode arrivals in the 1995 SWARM Experiment acoustic transmissions. *J. Acoust. Soc. Am.* submitted July 17, 1997.

Henyey, F. S. and Antje, H. (1997). Energetics of borelike internal waves. *J. Geophys. Res.*, 102(C2):3323–3330.

Hofmann-Wellenhof, B., Lichteneggter, H., and Collins, J. (1994). *GPS Theory and Practice.* Springer-Verlag, New York, third edition.

Jensen, F. B., Kuperman, W. A., Porter, M. B., and Schmidt, H. (1994). *Computational Ocean Acoustics.* American Institute of Physics, New York.

Krolik, J. L. (1992). Matched-field minimum variance beamforming in a random ocean channel. *J. Acoust. Soc. Am.*, 92(3):1408–1418.

Linder, C. (1996). Climatology of the shelfbreak front. Master's thesis, Massachussetts Institute of Technology/Woods Hole Oceanographic Institution.

Linder, C. A. and Gawarkiewicz, G. (1998). A climatology of the shelfbreak front in the Middle Atlantic Bight. *J. Geophys. Res.*, 103(C9):18405–18423.

Lynch, J., Gawarkiewicz, G., Chiu, C., Pickart, R., Miller, J., Smith, K., Brink, K., Beardsley, R., Sperry, B., and Potty, G. (1997). Shelfbreak PRIMER - An integrated acoustic and oceanographic field study in the Middle Atlantic Bight. In *Proceedings of the Shallow Water Acoustics Conference (SWAC)*, Beijing, China.

Lynch, J. F. (1983). On the use of focused horizontal arrays as mode separation and source location devices in ocean acoustics. Part I: Theory. *J. Acoust. Soc. Am.*, 74(5):1406–1416.

Lynch, J. F., Jin, G., Pawlowicz, R., Ray, D., Plueddemann, A., Chiu, C.-S., Miller, J. H., Bourke, R. H., Parsons, A. R., and Muench, R. (1996). Acoustic travel-time perturbations due to shallow-water internal waves and internal tides in the Barents Sea Polar Front: Theory and experiment. *J. Acoust. Soc. Am.*, 99(2):803–821.

Lynch, J. F., Miller, J. H., and Chiu, C.-S. (1989). Phase and travel-time variability of adiabatic acoustic normal modes due to scattering from a rough sea surface, with applications to propagation in shallow-water and high-latitude regions. *J. Acoust. Soc. Am.*, 85(1):83–89.

Lynch, J. F., Rajan, S. D., and Frisk, G. V. (1991). A comparison of broadband and narrow-band modal inversions for bottom geoacoustic properties at a site near Corpus Christi, Texas. *J. Acoust. Soc. Am.*, 89:648–654.

Milder, D. M. (1969). Ray and wave invariants for SOFAR channel propagation. *J. Acoust. Soc. Am.*, 46(5).

Miller, C. (1998). Estimating the acoustic modal arrivals using signals transmitted from two sound sources to a vertical line hydrophone array in the 1996 Shelfbreak PRIMER Experiment. Master's thesis, Naval Postgraduate School, Monterey, CA.

Munk, W., Worcester, P., and Wunsch, C. (1995). *Ocean Acoustic Tomography.* Cambridge Monographs on Mechanics. Cambridge University Press, Cambridge.

Munk, W. and Wunsch, C. (1978). Ocean acoustic tomography: a scheme for large-scale monitoring. *Deep-Sea Research*, 26A:123–161.

Pickart, R., Torres, D., McKee, T., Caruso, M., and Przystup, J. (1999). Diagnosing a meander of the shelf break current in the Middle Atlantic Bight. *J. Geophys. Res.*, 104(C2):3121–3132.

Pierce, A. D. (1965). Extension of the method of normal modes to sound propagation in an almost-stratified medium. *J. Acoust. Soc. Am.*, 37:19–27.

Porter, M. (1991). The KRAKEN normal mode program. Technical Report Rep. SM-245, SACLANTCEN, La Spezia, Italy.

Potty, G. (1999). Personal communications.

Potty, G. and Miller, J. (1998). Geoacoustic inversions for PRIMER. *J. Acoust. Soc. Am.*, 103(3(a)).

Potty, G. and Miller, J. (1999). Geoacoustic inversions for PRIMER. *J. Acoust. Soc. Am.* paper in preparation.

Preisig, J. C. and Duda, T. F. (1997). Coupled acoustic mode propagation through continental-shelf internal solitary waves. *IEEE J. of Oceanic Engineering*, 22(2):256–269.

Racine, B. S. (1996). A characterization of internal solitons in the SWARM region of the New York Bight. Master's thesis, Massachussetts Institute of Technology/Woods Hole Oceanographic Institution.

Ramp, S., Beardsley, R., and Legeckis, R. (1983). An observation of frontal wave development on a shelf-slope/warm core ring front near the shelf break south of New England. *J. Phys. Oceanogr.*, 13(5):907–912.

Richards, A. (1977). Atlantic Margin Coring Project 1976 - Preliminary report on shipboard and some laboratory geotechnical data. Open File Rep. No. 78-123, U.S. Geol. Surv.

Rubenstein, D. (1998). Observations of cnoidal internal waves and their effects on acoustic propagation in shallow water. *IEEE J. of Oceanic Engineering.* accepted for publication.

Shang, E. and Wang, Y. (1991). On the calculation of modal travel time perturbation. *Sov. Phys. Acoust.*, 37:411–413.

Sperry, B. J. (1994). Modal analysis of vertical array receptions for the Heard Island Feasibility Test. Master's thesis, Massachusetts Institute of Technology/Woods Hole Oceanographic Institution.

Sutton, P., Morawitz, W., Cornuelle, B. D., Masters, G., and Worcester, P. F. (1994). Incorporation of acoustic normal mode data into tomographic inversions in the Greenland Sea. *J. Geophys. Res.*, 99(C6):12,487–12,502.

Urick, R. (1983). *Principles of Underwater Sound.* McGraw-Hill Inc., New York, 3rd edition.

van Trees, H. L. (1968). *Detection, Estimation, and Modulation Theory: Part III.* John Wiley & Sons, New York.

von der Heydt, K. (1996). PRIMER-96 VLA data information. Technical report, Woods Hole Oceanographic Institution.

Weinberg, H. and Burridge, R. (1974). Horizontal ray theory for ocean acoustics. *J. Acoust. Soc. Am.*, 55:63–78.

Wunsch, C. (1996). *The Ocean Circulation Inverse Problem.* Cambridge University Press, New York.

Zhou, J. X., Zhang, X. Z., and Rogers, P. (1991). Resonant interaction of sound waves with internal solitons in the coastal zone. *J. Acoust. Soc. Am.*, 90:2042–2054.

Zhu, R. and Guan, D. (1992). Spatial horizontal coherence of sound in shallow water. *J. Acoust. Soc. Am.*, 92(2):956–961.